Technische Universität München
Fakultät für Physik

Abschlussarbeit im Masterstudiengang Physik

Search for Light-Meson Resonances in Diffractively Produced $\boldsymbol{K^-K^+\pi^-}$, $\boldsymbol{K^0_S\pi^-}$, and $\boldsymbol{K^0_SK^-}$ Final States Measured at COMPASS

Suche nach Leichte-Meson-Resonanzen in den diffraktiv-produzierten $\boldsymbol{K^-K^+\pi^-}$, $\boldsymbol{K^0_S\pi^-}$, und $\boldsymbol{K^0_SK^-}$ Endzuständen in COMPASS Daten

Julien Beckers

June 2021

Themensteller: Prof. Dr. Stephan Paul
Zweitgutachter: Prof. Dr. Hubert Kroha

Abstract

At high energies, quantum chromodynamics, i.e. the theory of strong interaction, can be calculated using perturbative methods and is in excellent agreement with data. However, at lower energies, in the regime of hadrons, these calculations break down, and one has to employ models, effective theories, or lattice QCD. Precision measurements of the excitation spectrum of hadrons help to test these approaches. Mesons are bound states of quarks and antiquarks and hence the simplest hadrons. However, the meson spectrum is still only partly known. So-called exotic mesons, that are not compatible with the quark-antiquark model, are especially interesting. At the COMPASS experiment, excited light mesons are produced via diffractive dissociation reactions.

In the first part of this thesis, we analyze data on the reaction $\pi^- + p \to K^- K^+ \pi^- + p$ recorded at COMPASS. This is the partner reaction to $\pi^- + p \to \pi^- \pi^+ \pi^- + p$ for which COMPASS has acquired a large data sample and has performed a detailed PWA. A partial-wave analysis of the $K^- K^+ \pi^- + p$ final state would help us to further study some interesting resonance states seen in $\pi^- \pi^+ \pi^-$. In order to select $K^- K^+ \pi^-$ events, particle identification must be performed, which causes a significant loss of events in certain phase-space regions. Performing a partial-wave analysis of the $K^- K^+ \pi^-$ data, we find that the results seem to be severely distorted by the low acceptance. We investigate these acceptance effects through various Monte Carlo pseudodata studies.

In the second part of this work, we develop an event selection for the reactions $K^- + p \to K_s^0 \pi^- + p$ and $\pi^- + p \to K_s^0 K^- + p$, not yet analyzed at COMPASS. The kinematic distributions of the data are discussed. Studies with Monte Carlo pseudodata are performed to study acceptances, resolutions, and backgrounds for the two channels.

Contents

Chapter 1

Introduction

In hadron physics, we study the bound systems of the strong interaction, the so-called *hadrons*. These are composite systems, built from two or more quarks held together by the exchange of gluons. We distinguish *mesons*, that have integer spin, and *baryons*, that have half-integer spin. Compared to other composite systems in physics, such as the hydrogen atom, hadrons exhibit some significant differences. One unique property is that the constituents of hadrons, i.e. quarks and gluons, have never been observed as free particles. This phenomenon, called *color confinement*, is due to the fact that gluons, unlike the photons that mediate the electromagnetic force in the hydrogen atom, carry strong (or color) charge themselves, and thus interact with each other.

This self-interaction leads to another significant difference between hadrons and the hydrogen atom. The total mass of the hadron is much larger than the sum of the constituent masses. This is because most of the hadron mass comes from the cloud of gluons and quark-antiquark pairs in the hadron. Unfortunately, it is up to now not possible to calculate the masses of the hadrons directly from first principles, which is especially concerning since the proton and neutron masses nearly completely determine the mass of visible matter in the universe. Indeed, the Lagrangian of quantum chromodynamics (QCD), which is the quantum field theory of the strong interaction between quarks and gluons, cannot be analytically solved at low energy scales of the order of the hadron masses. Because of the unique properties of the gluons, the strong coupling constant varies strongly with the energy. At high energies, the coupling constant is small (asymptotic freedom) and we can apply perturbation theory to solve the QCD Lagrangian. Towards lower energies however, i.e. in the hadron regime, the coupling constant approaches unity (confinement) and perturbative methods hence cannot be used. This means we have to rely on other methods, such as effective theories or lattice QCD. The latter simulates the Lagrangian on a grid of points in space and time, and can already predict hadronic ground states and calculate their masses reliably. However, current lattice QCD calculations of excited states are still limited in their predictive power.

From the experimental side, *hadron spectroscopy* aims to measure the excitation spectrum of hadrons and determine the fundamental properties of the states, such as their masses, widths, and quantum numbers. This provides important information in order to better understand the strong interaction at low energies. A precise knowledge of the spectrum is also important in order to compare to lattice QCD calculations. In hadron spectroscopy, the search for *exotic hadrons* is especially interesting. In principle, QCD allows hadrons to be any color-singlet combination of quarks, antiquarks and gluons, but the widely used constituent quark model assumes hadrons to only consist of a quark and an antiquark (i.e. mesons) or three quarks (i.e. baryons). States that do not fit into this simple model are labelled exotic. In the case of mesons, several possibilities for these exotic states exist, such as tetraquarks that contain four (anti)quarks, hybrid mesons that contain one quark-antiquark pair and an excitation of the gluon field, or glueballs, which consist only of gluons.

The COMPASS[1] experiment, located at the M2 SPS[2] beamline at CERN[3], has been a key experiment in the search for new hadronic states. It studies in particular the spectroscopy of light mesons, which consist of the three lightest quark species, i.e. up, down, and strange. Using the primary 400 GeV/c proton beam from the SPS, secondary charged hadrons, mostly pions and kaons, are created, momentum-selected, and guided onto a liquid-hydrogen target, with which they interact strongly. At the chosen high momentum of 190 GeV/c, the reaction is dominated by diffractive reactions beam $+ p \to X + p$, where the target proton scatters elastically, and only the beam particle is excited into light-meson states X. These intermediate states X quickly decay via the strong interaction into a multi-body hadronic final state, which is measured by the spectrometer. By performing a partial-wave analysis (PWA) of the measured kinematic distributions of the final-state particles, we decompose the data into partial- wave amplitudes with well-defined quantum numbers. This enables us to to distinguish the various resonances contributing to the intermediate states X and extract their parameters.

In this thesis, we have analyzed three different reactions (equivalently called channels). In the first reaction $\pi^- + p \to K^-K^+\pi^- + p$, a negative pion

---

[1] COmmon Muon Proton Apparatus for Structure and Spectroscopy

[2] Super Proton Synchrotron

[3] Conseil Européen pour la Recherche Nucléaire

interacts with a proton to produce the $K^-K^+\pi^-$ final state. The resonances created in this reaction are isovector states, i.e. they have isospin $I = 1$, and thus also appear in the already extensively analyzed partner reaction $\pi^- + p \to \pi^-\pi^-\pi^+ + p$ [1–3]. Therefore, a particular focus of this analysis is to gain more information on interesting states discovered in the previous analyses of the $\pi^-\pi^-\pi^+$ final state, such as the new axial-vector meson $a_1(1420)$ or the exotic $\pi_1(1600)$ resonance.

In addition, we have studied the reactions $K^- + p \to K^0_s\pi^- + p$ and $\pi^- + p \to K^0_sK^- + p$, which have a very similar experimental signature: In both reactions, a two-body final state containing a charged particle and a K^0_s is produced. The two reactions have already been studied by Cleland et al. in a similar experiment 40 years ago [4, 5]. This not only enables us to compare our findings to these earlier analyses, but also gives us the opportunity to search for the $a_6(2450)$ state that Cleland et al. claim to have observed in $\pi^- + p \to K^0_sK^- + p$. As of yet, this resonance has only been observed by them, and a partial-wave analysis of our more precise dataset could confirm its existence. Additionally, the $K^0_sK^-$ and the $K^-K^+\pi^-$ final states share an interesting property. As both have isospin $I = 1$ and no overall strangeness, a $K\bar{K}$ pair needs to be produced in both decays, which could give insights into the intrinsic $s\bar{s}$ content of the isovector states.

The reaction $K^- + p \to K^0_s\pi^- + p$ enables us to study the spectrum of kaon resonances, which is less well-known than the isovector spectrum. Additionally, there is a disagreement of the parameter values of one of the most well-known kaonic states, the $K^*(892)$, measured in different processes. In an analysis of the $\tau \to K_s\pi^-\nu_\tau$ decay, the Belle collaboration finds a $K^*(892)$ mass value that is significantly higher than the value measured for hadroproduced $K^*(892)$ [6]. As the $K^*(892)$ resonance contributes significantly to the intermediate states in $K^- + p \to K^0_s\pi^- + p$, we may be able to confirm or resolve this discrepancy.

For each of the three analyzed channels, the ultimate goal is to search for excited resonances contained in the intermediate states X. However, the analysis steps that were performed in the course of this thesis differ depending on the analyzed channel. Therefore, this thesis is divided into two independent parts. The first part deals with the $K^-K^+\pi^-$ channel. For this final state, the even selection has already been performed in Ref. [7]. The goal of this thesis was to attempt a partial-wave analysis of the selected data. Being a three-body final state, the PWA of the $K^-K^+\pi^-$ channel is complicated and has a potentially large model dependence. In combination with the limited acceptance of the COMPASS spectrometer for this final state, this leads to difficulties, which will be discussed. In the second part of this thesis, we perform a first analysis of COMPASS data for the $K^- + p \to K_s^0\pi^- + p$ and $\pi^- + p \to K_s^0 K^- + p$ channels. We will develop an event selection for the two rather similar final states, and use it to select clean event samples of both reactions. As in both reactions, two-body final states are produced, the data are easier to analyze and interpret. We thus gain direct information about the dominant resonances appearing in these reactions by inspecting the angular distributions of the final-state particles by eye, even without performing a partial-wave analysis of the reactions.

This thesis is structured as follows: First, we present in Chapter 2 the COMPASS spectrometer, with which the analyzed data were recorded. Chapter 3 introduces the concepts that will be of use in this thesis. We give an introduction to light mesons and their quantum numbers in Section 3.1, before discussing the construction of the scattering amplitudes from basic components and the involved theoretical assumptions in Section 3.2. Starting from these amplitudes, we introduce the partial-wave analysis method and explain how the data are analyzed in Section 3.3. Finally, Section 3.4 introduces the Monte Carlo techniques that are employed in this work. Then, we come to the first analysis part of this thesis, which is the partial-wave analysis of the $\pi^- + p \to K^-K^+\pi^- + p$ channel. In Chapter 4, we introduce the channel, present the event selection used to select the analyzed dataset, and take a first look at the kinematic distributions of the data, before coming to the partial-wave analysis of the channel in Chapter 5. In Section 5.1, we attempt a first PWA of the data, which reveals substantial technical difficulties. We investigate the encountered issues and gauge the reliability of our results by conducting a wide range of studies using Monte Carlo pseudodata in Sections 5.2 and 5.3. We conclude this analysis of the $\pi^- + p \to K^-K^+\pi^- + p$ channel in Chapter 6. In the second analysis part, we report on the analysis of the $K^- + p \to K_s^0\pi^- + p$ and $\pi^- + p \to K_s^0 K^- + p$ reactions. The event selections developed for the two channels are presented in Chapter 7. The kinematic distributions of the processed data are then discussed in Chapter 8 separately for each final state. Chapter 9 presents the results of Monte Carlo studies that have been performed to investigate the acceptance of the experimental setup and possible background contributions for both channels. In Chapter 10, we conclude the second part of this thesis by summarizing our findings and discussing the future steps of the analysis. The appendices contain further material on the $K^-K^+\pi^-$, $K_s^0\pi^-$, and $K_s^0 K^-$ analyses.

Chapter 2

Experimental Setup

The data used in this analysis were recorded at the COMPASS experiment at CERN. The following section gives a brief overview of the experimental setup used to produce hadrons and observe their interaction and subsequent decay. An in-depth description of the experiment can be found in Ref. [8].

2.1 The COMPASS Experiment

COMPASS is a large-acceptance magnetic spectrometer located at the CERN Super Proton Synchrotron (SPS). One of the goals of COMPASS is to study the spectroscopy of hadrons through the production of light mesons in inelastic scattering reactions of pions or kaons on protons or heavier nuclear targets at a beam momentum of 190 GeV/c. In these production reactions, the total center-of-mass energy of about 20 GeV is shared between the mesonic final state and the target recoil, which enables the coverage of a wide range of intermediate-state masses with only a fixed beam energy. Also, many possible sets of quantum numbers are available to the intermediate states, so that both non-exotic and exotic intermediate states can be produced.

The experimental setup can be split into four main parts: the beam line, the target area, and two spectrometer sections. Fig. 2.1 shows a three-dimensional schematic view of the spectrometer, omitting the beam line.

2.1.1 COMPASS Beam Line

COMPASS uses high-intensity secondary hadron beams consisting either of mainly negative pions and small admixtures of kaons and antiprotons or of positive protons, pions, and kaons. The beams are produced by a 400 GeV/c primary proton beam from the SPS impinging on a Beryllium target. For the data analyzed in this thesis, the secondary beam was tuned to negative hadrons at a momentum of 190 GeV/c. At this momentum, the beam consists

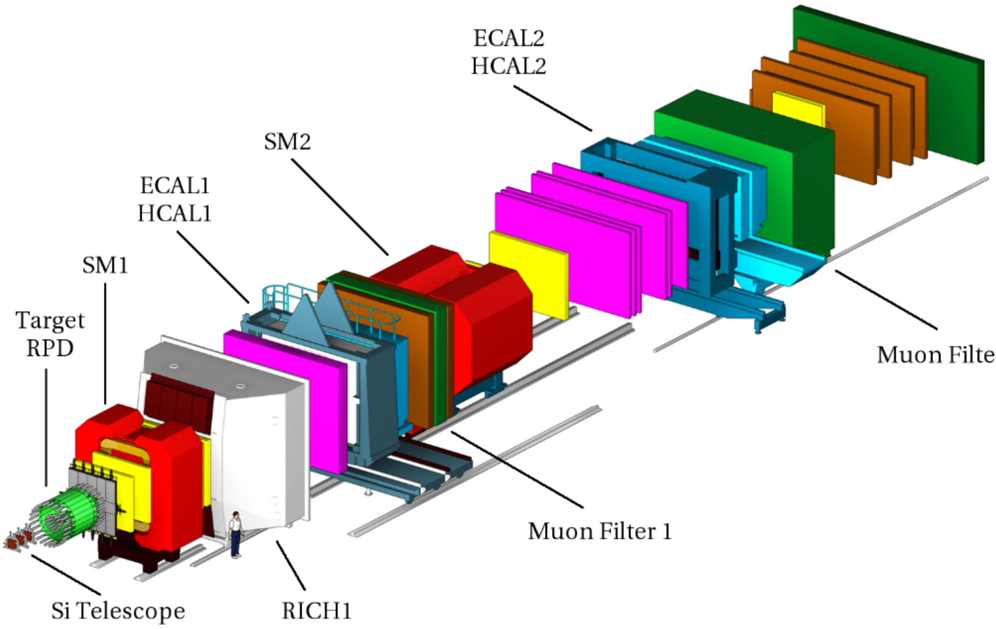

Figure 2.1: Three-dimensional view of the COMPASS spectrometer, with the beam coming from the lower left. The CEDAR detectors and the beam line upstream of the target are not shown. From Ref. [8].

of 96.8% π^-, 2.4% K^-, and 0.8% $\bar{p}$. Two beam Cherenkov detectors (CEDARs) located 30 m upstream of the target identify the incoming particles.

2.1.2 Target Region

The target is surrounded by a time-of-flight detector called Recoil Proton Detector (RPD). This detector measures velocity and energy loss of the recoil particles, essential for identifying the recoil protons. High-resolution silicon detectors in the target region measure the trajectories of the beam particles and those of the charged final-state particles with high precision.

2.1.3 Large-Angle Spectrometer

The Large-Angle Spectrometer (LAS), immediately downstream of the target, measures scattered particles with polar angles of up to 180 mrad. The array of detectors located around the first dipole magnet (SM1) comprises several tracking detectors, a Ring-Imaging Cherenkov detector (RICH-1), which identifies charged particles, and electromagnetic and hadronic calorimeters, measuring their energy. The RICH-1 detector will be discussed in more detail in Section 2.2.

2.1.4 Small-Angle Spectrometer

The Small-Angle Spectrometer (SAS), which constitutes the last part of the COMPASS spectrometer, detects particles that are emitted at small polar angles of less than 30 mrad and at momenta larger than 15 GeV/c. These particles pass through central holes in the calorimeters of the LAS. Similar to the LAS, tracking detectors and calorimeters are positioned around a dipole magnet (SM2).

2.2 Particle Identification using the RICH-1 Detector

An important step in the reconstruction of some final states that are produced in the scattering process is the identification of the outgoing particles. This is performed by the Ring-Imaging Cherenkov detector (RICH-1), which distinguishes charged hadrons in a certain momentum range using the Cherenkov effect. In the following sections, we will give an overview of the working principle and the performance of the detector. More details can be found in Ref. [8].

2.2.1 Cherenkov Effect

The Cherenkov effect occurs when a charged particle passes through a medium with a speed higher than the phase velocity of light in the medium. Electromagnetic radiation is then emitted at a specific angle θ with respect to the direction of the particle. The angle is given by the particle's velocity $v = \beta c$ and the refractive index $n > 1$ of the medium:

$$\cos\theta = \frac{1}{n\beta} \tag{2.1}$$

By measuring θ and hence v, one can distinguish between particles of different mass by additionally determining the momentum of the particles.

2.2.2 The RICH-1 Detector

The RICH-1 detector is a 3 meter-long vessel filled with C_4F_{10} ($n = 1.0014$ at $\lambda = 400$ nm), which covers the whole angular acceptance of the LAS. It identifies charged particles of known momentum by measuring the angle of the Cherenkov radiation that is emitted during traversal of the gas. These Cherenkov photons are reflected by two spherical mirror surfaces onto photodetectors in such a way that photons emitted at the same angle θ are focused onto the same point. Therefore, the photons form rings in the detector plane with specific, constant radius given by θ.

2.2.3 RICH-1 Detector Performance

The performance of the RICH-1 detector depends strongly on the momentum of the particle. The detector saturates at a Cherenkov angle of approximately 55 mrad, which enables separation of pions and kaons at a 2.5 σ level up to momenta of 45 GeV/c. Figure 2.2 shows the dependence of the Cherenkov

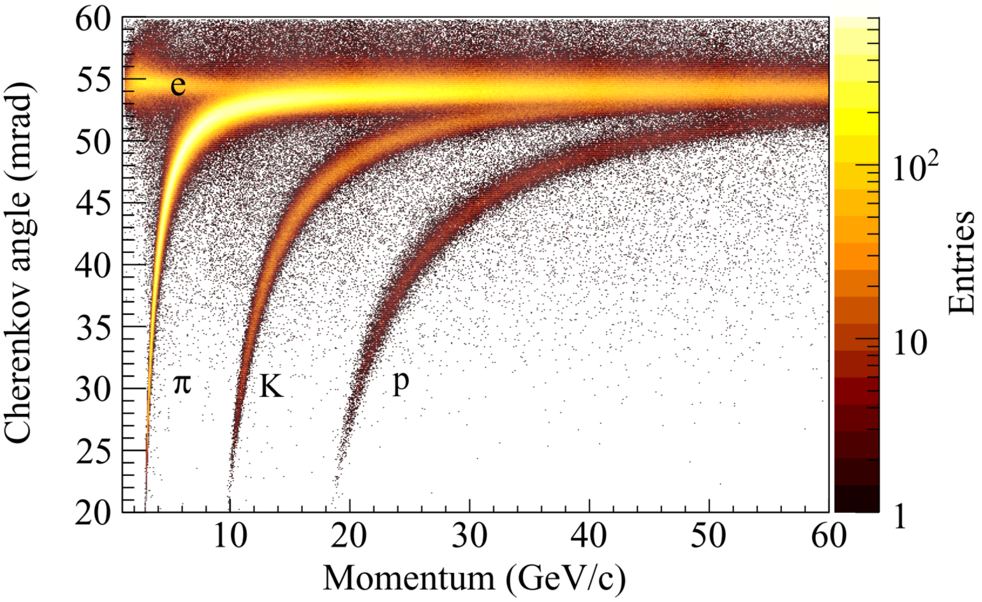

Figure 2.2: RICH-1 Cherenkov angle versus particle momentum for different particle species. From Ref. [8].

angle for reconstructed rings on the particle momentum for different particle species. At low momenta, above the thresholds of about 3 GeV/c for π and 10 GeV/c for K, the bands corresponding to those two mesons are clearly separated, and identification is possible. However, when the particles reach higher momenta, the Cherenkov angles become similar, rendering it increasingly difficult to distinguish pions from kaons. Especially above 45 GeV/c, a clear distinction is only possible in rare cases.

Chapter 3

Methods

In this chapter, an overview of the methods and formalisms used to analyze the COMPASS data is given. After a brief summary of the properties of light mesons, the scattering amplitude describing the studied processes will be constructed. Then, the partial-wave analysis approach and the procedure to extract the desired parameters will be explained. Finally, the employed Monte Carlo integration techniques will be discussed briefly. This chapter is a summary of Ref. [9], which gives a general and pedagogical overview of several theoretical concepts of scattering reactions as well as a detailed derivation of the partial-wave analysis formalism.

3.1 Light Mesons

Mesons are hadronic composite systems consisting of one quark q and one antiquark $\bar{q}'$, bound by strong interaction. They can be classified by their quark content, total angular momentum and other quantum numbers such as parity, listed below.

Flavour: The Standard Model contains six flavours of quarks, that are characterized by their flavour quantum numbers. All flavour quantum numbers are conserved by the strong interaction. Light mesons consist of the three lightest quark species, i.e. up (u), down (d), and strange (s) quarks. The u and d quarks are characterized by the so-called *strong isospin* I, or simply isospin, while the strange quark, similar to the remaining heavier quarks, has its own flavour quantum number, *strangeness* S. The isospin symmetry is an approximate symmetry and corresponds to the near mass-degeneracy of the u and d quarks, which translates into the near mass-degeneracy of the proton and the neutron. Isospin is a vector quantity: u and d quarks have $I = 1/2$, but different projections $I_3 = \pm 1/2$. All other quarks have $I = 0$. As a general rule, the charge of a quark and its flavour quantum number have the same sign. The strange quark thus has strangeness $\mathrm{S} = -1$, as it has negative charge.

Spin and Internal Angular Momentum: Quarks are fermions and have spin 1/2. Mesons can therefore be either spin-singlet or spin-triplet states, where the quark spins couple to a total intrinsic spin $S = 0, 1$. Furthermore, the quarks can have a relative orbital angular momentum L. Both of these quantities couple to the total angular momentum, i.e. spin J, of the system, which can take the values $|L - S| \leq J \leq (L + S)$.
Parity: Parity represents the symmetry of the wave function under a point reflection. It is a multiplicative quantum number, and its eigenvalues are $P = \pm 1$ or simply $P = \pm$. Parity is conserved by the strong interaction. In the quark model, the parity of a meson is given by

$$P = (-1)^{L+1} \tag{3.1}$$

It comes from the parity of the L eigenstate $(-1)^L$. The additional factor -1 is the product of the intrinsic parities of quark $(+1)$ and antiquark (-1). States with $P = (-1)^J$, i.e. $J^P = 0^+, 1^-, \ldots$, are said to have *natural parity*, while states with $P = (-1)^{J+1}$, i.e. $J^P = 0^-, 1^+, \ldots$, have *unnatural parity.*
***C* parity and *G* parity:** The C parity is the multiplicative quantum number associated to the charge conjugation operation, which transforms particles into their antiparticles and vice-versa. Only neutral flavorless mesons, i.e. neutral mesons without overall strangeness and heavier flavours, are eigenstates of charge conjugation, and have

$$C = (-1)^{L+S} \tag{3.2}$$

The concept of C parity can be extended to charged flavorless mesons, by introducing G parity. It is defined as applying the charge conjugation operator, followed by a 180° rotation in isospin space around the y axis: $G = C\, \mathrm{e}^{i\pi I_2}$. G parity of flavorless mesons is given by

$$G = (-1)^{L+S+I} \tag{3.3}$$

The strong interaction conserves both C and G parity.

Mesons, consisting of one quark and one antiquark, obey certain rules for their quantum numbers. They can, for example, only have $I = 0, 1$ or $\mathrm{S} = 0, 1$. States with quantum numbers that are not compatible with the quark model are called *exotic*. Flavor-exotic states have forbidden flavor, e.g. strangeness $\mathrm{S} = 2$, while spin-exotic states have forbidden J^{PC} quantum numbers, e.g. $J^{PC} = 1^{-+}$. Exotic states are hypothesized to consist of other configurations than one quark and one antiquark. Several possibilities exist: *hybrids* contain a quark-antiquark pair and excited gluon fields, *tetraquarks* have two $q\bar{q}'$ pairs and *glueballs* consist only of gluons.

Mesons are classified into groups via their quantum numbers, detailed above. The Particle Data Group's naming scheme for flavorless mesons depends on the particle's isospin $I = 0, 1$ and J^{PC} quantum numbers. The spin J is added as a subscript except for pseudoscalar ($J^{PC} = 0^{-+}$) and vector ($J^{PC} = 1^{--}$) mesons. Except for some ground states such as the pion, the state's mass in MeV/c^2 is added in parentheses to distinguish the radial excitations, which have the same quantum numbers and hence carry the same name as the corresponding ground state. For example, π_J states are mesons with $I = 1$ and $J^{PC} = 0^{-+}, 2^{-+}, \ldots$, equivalent to ${}^{2S+1}L_J = {}^1(\text{even})_J$ in the simple quark model, with the lowest mass state being the well-known pion. States with $J^{PC} = 1^{-+}$ are spin-exotic π_J states. a_J states have $I = 1$ and $J^{PC} = 0^{++}, 1^{++}, \ldots$, i.e. ${}^{2S+1}L_J = {}^3(\text{odd})_J$. Light mesons carrying strangeness, i.e. kaons, are symbolized by K_J if they have unnatural parity or by K^*_J if they have natural parity.

3.2 Partial-Wave Analysis (PWA) Model

In the following, a model for the scattering amplitude of the processes to be investigated will be built. Single-diffraction dissociation reactions are inelastic scattering processes of the form

$$\text{beam} + p \to (1 + 2 + \ldots + n) + p \tag{3.4}$$

where a high-energetic beam hadron interacts strongly with a target proton, producing an n-body final-state and a recoil proton. Under the assumption that intermediate resonances X with specific quantum numbers dominate the process, it can be divided into two subprocesses: (i) the production of X via an inelastic two-body scattering reaction beam $+\, p \to X + p$ and (ii) the decay of X into the n-body final state $(1 + 2 + \ldots + n)$.

Subprocess (i) depends on the invariant mass m_X of the n-body final state and the two Mandelstam variables s and t, where s is the squared center-of-momentum energy

$$s = (p_\text{beam} + p_\text{target})^2 = (p_X + p_\text{recoil})^2 \tag{3.5}$$

and t is the transferred squared four-momentum

$$t = (p_\text{beam} - p_X)^2 = (p_\text{target} - p_\text{recoil})^2 \;. \tag{3.6}$$

However, s is constant in fixed-target experiments such as COMPASS, so that its dependence falls away. Additionally, $t < 0$ in scattering processes. In order to deal only with positive values, it can be equivalently replaced by the reduced squared four-momentum transfer

$$t' := |t| - |t|_{\min} \tag{3.7}$$

where $|t|_{\min}$ is the minimal value of $|t|$, i.e. $|t|$ at zero scattering angle.

The n-body decay (ii) is determined by the kinematic distribution of the final-state particles, which depends on a set τ_n of $(3n-4)$ phase-space variables, as well as m_X.

The intensity distribution of the process in Eq. (3.4) is given by

$$\mathcal{I}(m_X, t', \tau_n) := \frac{\mathrm{d}N}{\mathrm{d}m_X\,\mathrm{d}t'\,\mathrm{d}\Phi_n(m_X, \tau_n)} \propto \left| \sum_a \mathcal{T}_a\,(m_X, t')\,\Psi_a(m_X, \tau_n) \right|^2 \tag{3.8}$$

with N being the number of produced events and $\mathrm{d}\Phi_n(m_X, \tau_n)$ being the differential phase-space element. The latter can be expressed by the phase-space density of states $\rho_n(m_X, \tau_n)$ in the variables m_X and τ_n:

$$\mathrm{d}\Phi_n(m_X, \tau_n) = \rho_n(m_X, \tau_n)\,\mathrm{d}\tau_n \tag{3.9}$$

The intensity distribution is a direct measure for the scattering amplitude, which is factorized into two parts in Eq. (3.8): a transition amplitude $\mathcal{T}\,(m_X, t')$ describing the production and propagation of an intermediate state X and a decay amplitude $\Psi\,(m_X, \tau_n)$ describing its decay into the $(1 + 2 + ... + n)$ final-state, i.e. the kinematic distribution of the final-state particles. Different intermediate states, distinguished by the index a that is discussed later in Section 3.3.1, can contribute and have to be summed over coherently. The information about the intermediate states X and the resonances present therein is contained in the transition amplitudes. In order to extract it from the data, the decay amplitudes have to be known. They are thus calculated in advance with the model presented in Sections 3.2.1 to 3.2.4.

3.2.1 Isobar Model

To model the decay of the intermediate resonances X into final states with $n > 2$, the isobar model is used. In this approach, the n-body decay is described as a chain of subsequent two-body decays via additional intermediate resonances ξ called *isobars*. The decay amplitude $\Psi\,(m_X, \tau_n)$ can then be expressed as the product of two-body decay amplitudes of the successive decays. The model assumes no interaction between final-state particles. The structure of this two-body decay amplitude is detailed in Section 3.2.2, and examples for two- and three-body spinless final states are given in Section 3.2.3.

3.2.2 Two-Body Decay Amplitude

The two-body decay amplitude describes the propagation of a resonance r with total spin J_r and spin projection M_r and its decay $r \to 1 + 2$ into two daughter particles in the r rest frame. As the two particles 1 and 2 are emitted back-to-back in the rest frame, the kinematics of the decay are fully described by the polar angle ϑ_r and the azimuthal angle ϕ_r of one of the daughter particles.

The decay amplitude can be factorized into two parts: (i) an angular part, which is completely defined by the angular-momentum quantum numbers of the parent and the daughter particles and is given by the Wigner D-functions [10], and (ii) a dynamical part, which describes the dependence of the amplitude on the invariant mass m_r of the $(1, 2)$ system and needs to be modelled.

$$\mathcal{A}_{r\to 1+2}(m_r, \vartheta_r, \phi_r) = \underbrace{f_{r\to 1+2}(\vartheta_r, \phi_r)}_{\text{angular part}} \times \underbrace{\mathcal{D}_r(m_r)\, \alpha_{r\to 1+2}\, F_{L_r}(m_r)}_{\text{dynamical part}} \tag{3.10}$$

The propagator term $\mathcal{D}_r(m_r)$ will be further discussed in Section 3.2.4. The complex-valued coupling $\alpha_{r\to 1+2}$ describes the strength and phase of the decay and is assumed to be independent of m_r. The barrier factor $F_{L_r}(m_r)$ describes the suppression of higher orbital angular momenta L_r between the daughter particles at low masses m_r. One also has to choose appropriate coordinate systems in which the decays are described. They are presented in Section 3.2.5.

3.2.3 Decay Amplitudes for $n = 2$ and $n = 3$ Final States

The decay amplitude for a two-body final state is simply given by the two-body decay amplitude of X in Eq. (3.10). Assuming the final-state particles are spinless, as is the case for π and K, introduces the additional simplification that the Wigner D-function in the angular part reduces to spherical harmonics $Y_{J_X}^{M_X}$ with J_X being the total angular momentum of X and M_X its projection. This yields

$$\Psi_{X\to 1+2}(m_X, \vartheta_X, \phi_X) = Y_{J_X}^{M_X}(\vartheta_X, \phi_X)\, \mathcal{D}_X(m_X)\, \alpha_{X\to 1+2}\, F_{L_X}(m_X)\ . \tag{3.11}$$

For a three-body final state, the decay is modelled as a first decay $X \to \xi + 3$ of X into an isobar ξ and a bachelor particle, followed by a second decay $\xi \to 1 + 2$ of the isobar. The decay amplitude of this process is obtained via recursive application of Eq. (3.10). The three final-state particles 1, 2, and 3 are again spinless. However, the intermediate isobar resonance may have non-zero spin J_ξ, which is described in the *helicity basis* further defined in Section 3.2.5. This renders the angular part of the X decay more complicated than in Eq. (3.11). In the helicity formalism, the isobar spin J_ξ is included by coherently summing over the possible helicities λ of the isobar, i.e. its spin projection onto the direction of momentum. The coupling of the isobar spin J_ξ and the orbital angular momentum L between ξ and particle 3 to the spin state of X is expressed by the Clebsch-Gordan coefficient $(L, 0\,; J_\xi, \lambda \,|\, J_X, \lambda)$. An additional normalization term depending on L arises. The final formula for the decay amplitude of X into three spinless final-state particles via an additional isobar is

$$\begin{aligned} &\Psi_{X\to(1+2+3)}(m_X, \vartheta_X, \phi_X, m_\xi, \vartheta_\xi, \phi_\xi) \\ &\quad = \sqrt{\frac{2L+1}{4\pi}}\, \mathcal{D}_X(m_X)\, \alpha_{X\to\xi+3}\, F_L(m_X) \\ &\qquad \times \sum_\lambda (L, 0\,; J_\xi, \lambda \,|\, J_X, \lambda)\, D^{J_X}_{M\lambda}(\vartheta_X, \phi_X, 0) \\ &\qquad\quad \times Y^{M_\xi}_{J_\xi}(\vartheta_\xi, \phi_\xi)\, \mathcal{D}_\xi(m_\xi)\, \alpha_{\xi\to 1+2}\, F_{J_\xi}(m_\xi)\ . \end{aligned} \tag{3.12}$$

As will be explained in Section 3.3.4, the decay amplitude, including the propagator terms of all isobar resonances, must be calculable without any free parameters. To this end, the unknown couplings $\alpha_{X\to 1+2}$ for $n = 2$ or $\alpha_{X\to\xi+3}$ and $\alpha_{\xi\to 1+2}$ for $n = 3$ are pulled out of the decay amplitude, under the assumption that they are independent of m_X or any phase-space variable. In order to make no assumptions about the resonances present in the intermediate state, the propagator term $\mathcal{D}_X(m_X)$ of X cannot be modelled, unlike the isobar propagator terms which will be discussed in Section 3.2.4. It is thus also factorized out of the decay amplitude, and can be absorbed by the transition amplitudes $\mathcal{T}(m_X, t')$, together with the decay couplings. The transition amplitudes then also include information about the decay channel, and contain all unknown quantities.

3.2.4 Parametrization of Propagator Terms

In most cases, the propagator terms $\mathcal{D}_\xi(m_\xi)$ of the isobar resonances in Eq. (3.12) can be approximated well by relativistic Breit-Wigner amplitudes

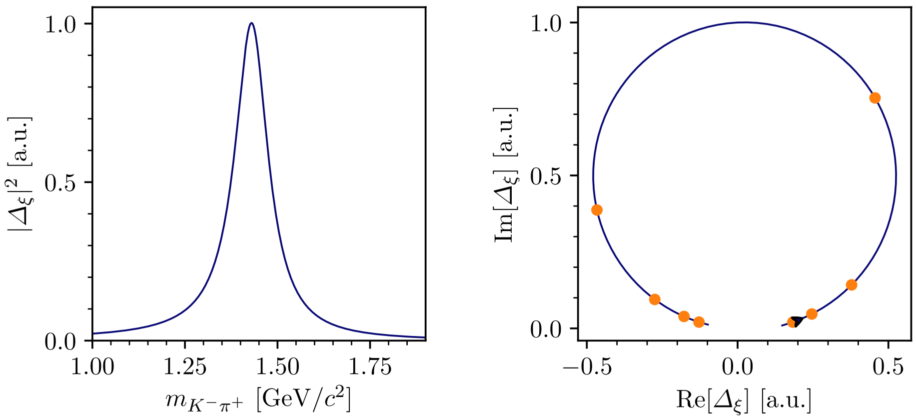

Figure 3.1: Breit-Wigner amplitude $\mathcal{D}_\xi \overset{\text{(here)}}{=} \Delta_\xi$ of the $K_2^*(1430)$ with $m_0 = 1430$ MeV/c^2 and $\Gamma_0 = 100$ MeV/c^2. (left) Intensity as a function of the invariant mass $m_{K^-\pi^+}$. (right) Argand diagram of the real and imaginary parts of the amplitude. From Refs. [11, 12].

with nominal mass m_0 and constant width Γ_0 (illustrated in Fig. 3.1 for the $K_2^*(1430)$ resonance):

$$\mathcal{D}_r(m_r; m_0, \Gamma_0) = \frac{m_0\,\Gamma_0}{m_0^2 - m_r^2 - i\,m_0\,\Gamma_0} \tag{3.13}$$

The parametrization of an isobar resonance through Breit-Wigner amplitudes is an approximation, which is viable only under certain conditions: (i) the width of the resonance must be small enough. For broader resonances, up to a point, the constant width Γ_0 can be replaced by a mass-dependent width $\Gamma(m_\xi)$ (see e.g. Ref. [9, Eq. 154]). (ii) The resonance must not lie close to the threshold of a decay channel (e.g. $\pi\pi$ or KK). (iii) The resonance must not lie close to other resonances with the same quantum numbers.

The Breit-Wigner approximation is usually not applicable for $\pi\pi$, $K\pi$ and KK S-wave resonances with $J^P = 0^+$, as many of these resonances, especially at low masses, contradict at least one of those limitations. Therefore, special parametrizations must be employed. An example of such a parametrization for a $K\pi$ S-wave isobar is presented in Fig. 3.2. The difference to the simple Breit-Wigner parametrization in Fig. 3.1 is apparent.

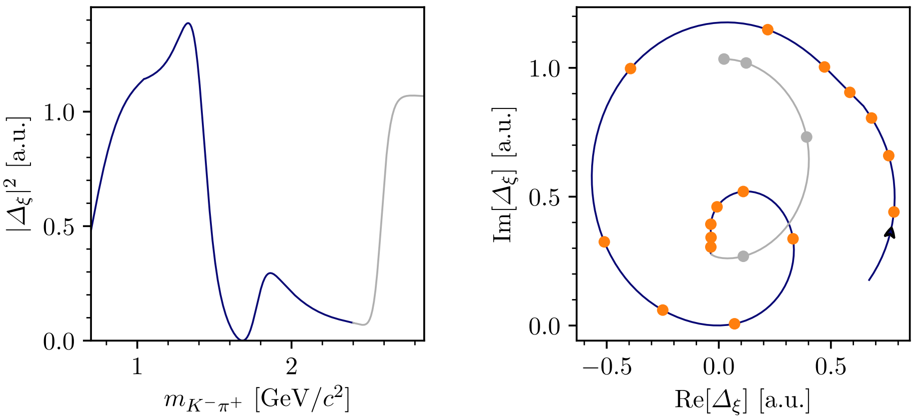

Figure 3.2: Palano-Pennington parametrization of the $K\pi$ S-wave dynamical amplitude $\mathcal{D}_r \overset{\text{(here)}}{=} \Delta_\xi$. (left) Intensity as a function of the invariant mass $m_{K^-\pi^+}$. (right) Argand diagram of the real and imaginary parts of the amplitude. From Refs. [11, 12].

3.2.5 Coordinate Systems

The reference frames used to describe the subsequent two-body decays are presented in Fig. 3.3. The Gottfried-Jackson frame (GJ) is used to describe the decay of the intermediate states X into an isobar and a bachelor particle, which is labelled "rest" in Fig. 3.3). The GJ frame is a rest frame of X with the z_{GJ} axis along the direction of the beam particle and the y_{GJ} axis along the normal of the production plane (see Fig. 3.3). The polar angle ϑ_{GJ} and the azimuthal angle ϕ_{GJ} of one of the daughter particles of X are sufficient to characterize the angular distribution of both isobar and bachelor particle.

For the isobar decay, the helicity frame (HF) is used to describe the angular distribution. It is constructed by boosting from the GJ frame into the rest frame of the isobar and taking the z_{HF} axis along the original direction of the isobar. The unit vector for the y_{HF} axis is given by $\hat{y}_{\mathrm{HF}} \propto \hat{z}_{\mathrm{parent}} \times \hat{z}_{\mathrm{HF}}$, with $\hat{z}_{\mathrm{parent}}$ being the direction of the z axis in the parent rest frame. As the isobar is at rest in the helicity frame, the angular distribution can again be described by the polar angle ϑ_{HF} and the azimuthal angle ϕ_{HF} of one of the daughter particles of the isobar.

The decay angles are chosen to be part of the $(3n-4)$ phase-space variables τ_n. For final states with $n = 2$, there are no isobar decays and hence $\tau_2 =$

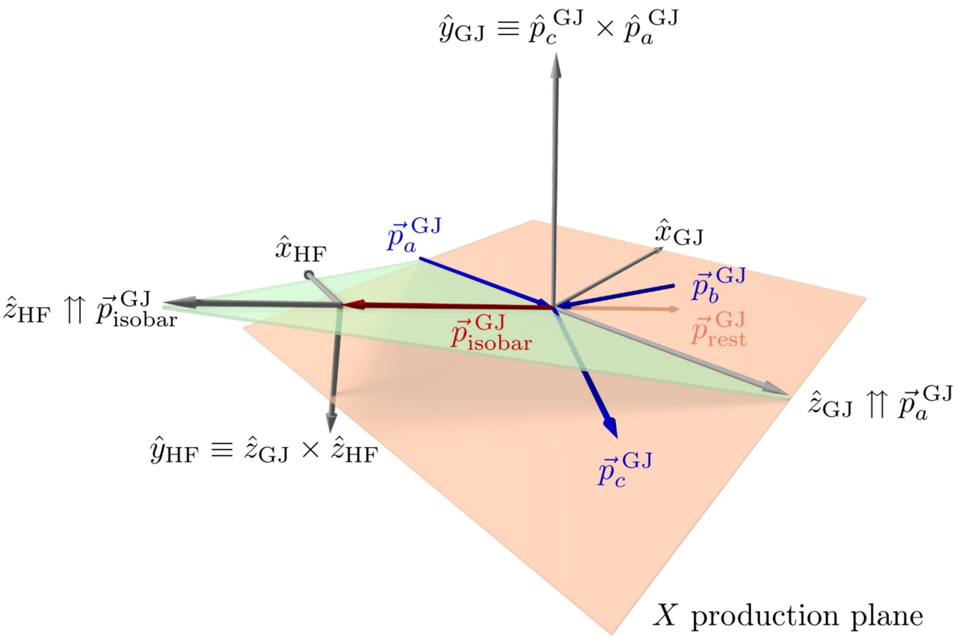

Figure 3.3: Illustration of the reference frames used in the reaction $a + b \to X + c$, where a is the beam particle and b/c are the target/recoil proton. The decay $X \to \text{isobar} + \text{rest}$ is described in the Gottfried-Jackson frame (GJ), while the isobar decay is described in the helicity frame (HF). From Ref. [9].

$(\vartheta_{\mathrm{GJ}}, \phi_{\mathrm{GJ}})$. For $n = 3$, the phase-space variables consist of the decay angles and the invariant mass of the isobars, e.g. $\tau_3 = (\vartheta_{\mathrm{GJ}}, \phi_{\mathrm{GJ}}, m_\xi, \vartheta_{\mathrm{HF}}, \phi_{\mathrm{HF}})$.

3.3 Partial-Wave Decomposition

3.3.1 Partial Waves

In diffractive dissociation reactions, the possible quantum numbers for X are limited only by the conservation laws of the strong interaction. These quantum numbers, presented in Section 3.1, consist of isospin I, spin J, its projection M, and parity P. If the mesonic state is non-strange, G-parity, and if it is also neutral, C-parity, can be defined in addition. The decay amplitude $\Psi(m_X, \tau_n)$ is completely defined by the set $i := (I^{(G)}\, J^{P(C)}\, M)$ of X quantum numbers and by its decay mode expressed for $n = 3$ spinless final-state particles by the isobar ξ and the orbital angular momentum L between the isobar and the bachelor particle, i.e. $j := (\xi, L)$. The transition amplitude depends on the X quantum numbers i. By including the decay couplings α_k as discussed in Section 3.2.3, the newly defined transition amplitude also carries information about the coupling to a certain decay channel j.

The index a defined as

$$a \equiv (i, j) \tag{3.14}$$

represents a certain *partial wave*. The production of an intermediate state X with quantum numbers i and its decay chain j is thus described by the transition and decay amplitudes $\mathcal{T}_a(m_X, t')$ and $\Psi_a(m_X, \tau_n)$.

3.3.2 Intensity distribution

The intensity distribution is written as a truncated, coherent sum of partial waves denoted by the index a, i.e.

$$\mathcal{I}(m_X, t', \tau_n) = \left| \sum_a^{N_\text{waves}} \mathcal{T}_a(m_X, t')\, \Psi_a(m_X, \tau_n) \right|^2 \tag{3.15}$$

As it is in general not feasible to model the dependence of the transition amplitudes on m_X and t', the event sample is divided into small (m_X, t') cells. Under the assumption that the m_X and t' bins are narrow enough (e.g. the mass bins should be significantly narrower than the width of a typical mesonic resonance), the $\mathcal{T}_a$ are assumed to be constant in a given (m_X,t') cell. The final goal of the analysis is to extract the set of unknown transition amplitudes $\{\mathcal{T}_a\}$ in each (m_X, t') cell using the fact that the decay amplitudes Ψ_a and hence the τ_n dependence of the amplitudes is known. The $\mathcal{T}_a$ contain information about the resonances contained in the intermediate states X. Resonances are characterized by an increase in intensity and a phase movement of 180° at the resonance mass, which is observable across the m_X bins (illustrated e.g. in Fig. 3.1). This approach, applicable for large datasets, does not make any assumption on the resonance content of the transition amplitudes other than the truncation of the partial-wave expansion, i.e. the set of waves included in the sum. Before discussing methods of determining $\mathcal{T}_a$ in Section 3.3.4, two extensions of the model are introduced in Section 3.3.3.

3.3.3 Incoherent Contributions

Equation (3.15) assumes that all partial waves are fully coherent. Depending on the studied process, certain effects can lead to incoherence of the intermediate states X. Two important examples are discussed below.

In order to incorporate parity conservation in the strong-interaction scattering process into the PWA model, an additional quantum number, the *reflectivity* ε, is defined. It is often convenient to define the spin states in the reflectivity basis, where states have $M \geq 0$ and $\varepsilon = \pm 1$ such that the multiplicity of the spin states of $2J + 1$ is conserved. Because of parity conservation, states with different reflectivities do not interfere, and the amplitudes are thus summed over incoherently, i.e.

$$\mathcal{I}(\tau_n; m_X, t') = \sum_{\varepsilon=\pm 1} \left| \sum_{a}^{N^{\varepsilon}_{\text{waves}}} \mathcal{T}^{\varepsilon}_a(m_X, t')\, \Psi^{\varepsilon}_a(\tau_n; m_X) \right|^2 \tag{3.16}$$

In the high-energy limit, the reflectivity ε corresponds to the naturality η of the exchange particle between beam and target particles. Since at high energies, the exchange is assumed to be dominated by Pomeron exchange with $\eta = +1$, it is often sufficient to take into account only waves with positive reflectivities.

Another incoherent effect to consider is the possible contamination of the data by misreconstructed or partially reconstructed events that pass through the event selection process because of their similarity to the desired signal. This background is modelled by incoherently adding a wave with an isotropic distribution in the phase space, the so-called *flat wave*, to the intensity distribution. As the corresponding decay amplitude is constant, one can set $\Psi_{\text{flat}} \equiv 1$ such that

$$\mathcal{I}(\tau_n; m_X, t') = \sum_{\varepsilon=\pm 1} \left| \sum_{a}^{N_{\text{waves}}} \mathcal{T}^{\varepsilon}_a(m_X, t')\, \Psi^{\varepsilon}_a(\tau_n; m_X) \right|^2 + |\mathcal{T}_{\text{flat}}(m_X, t')|^2 \tag{3.17}$$

3.3.4 Maximum-Likelihood Method

To estimate the unknown values of the transition amplitudes $\mathcal{T}_a^\varepsilon$ in Eq. (3.17), we apply the maximum-likelihood method. The maximum-likelihood fit is performed independently in each (m_X, t') cell by maximizing the likelihood function $\mathcal{L}$, which is the joint probability density of the data set given the parameter values $\{\mathcal{T}_a^\varepsilon\}$.

In general, for a dataset $\vec{x} \coloneqq (x_1, ..., x_N)^T$ of N independent random variables each following the same probability density function $f(x_k, \{\theta_i\})$ with a set of unknown parameters $\{\theta_i\}$, the likelihood function is given by

$$\mathcal{L}(\{\theta_i\}; \vec{x}) = \prod_{k=1}^{N} f(x_k, \{\theta_i\}) \ . \tag{3.18}$$

The maximum likelihood estimate $\{\hat{\theta}_i\}$ is given by those parameter values that maximize the likelihood function, i.e.

$$\{\hat{\theta}_i\} = \arg\max_{\{\theta_i\}} \mathcal{L}(\{\theta_i\}; \vec{x}) \ . \tag{3.19}$$

If the number N of data points is not predetermined but is a result of the measurement and therefore also a random variable, the likelihood function in Eq. (3.18) is extended by a Poisson distribution with the expected number of events λ, i.e.

$$\mathcal{L}_{\text{ext}}(\{\theta_i\}, \lambda; \vec{x}, N) = \underbrace{\frac{\lambda^N e^{-\lambda}}{N!}}_{\substack{\text{Poisson} \\ \text{distribution}}} \ \underbrace{\prod_{k=1}^{N} f(x_k, \{\theta_i\})}_{= \mathcal{L}(\{\theta_i\}; \vec{x})} \ . \tag{3.20}$$

In the case of the partial-wave analysis, the intensity model in Eq. (3.17) can be used to construct the probability density distribution of the events if some modifications are applied. Firstly, the model describes the phase-space distribution of the produced events, i.e. the events a hypothetical, perfect detector would measure. However, in reality, the *acceptance* ϵ of the setup must be taken into account. Here, the term acceptance is used to characterize all effects causing loss of events, ranging from the efficiencies of individual detectors to the efficiency of the event reconstruction and selection. The acceptance depends on the kinematic variables τ_n, m_X, t'. From here on, a specific (m_X, t') cell is considered and the m_X, t' dependence is omitted to ease notation. The measured number of events in the cell as predicted by the model in Eq. (3.17) is given by

$$N_{\text{pred}}^{\text{meas}} = \int \mathrm{d}\Phi_n(\tau_n)\, \epsilon(\tau_n)\, \mathcal{I}(\tau_n) \; . \tag{3.21}$$

To obtain a model for the actual intensity distribution measured by the detector, Eq. (3.17) has to be weighted by the acceptance. This intensity distribution then has to be normalized to get the probability density function of the measured events given the parameters $\{\mathcal{T}_a^{\varepsilon}\}$ in a certain (m_X, t') bin:

$$f(\tau_n; \{\mathcal{T}_a^{\varepsilon}\}) = \frac{\rho_n(\tau_n)\, \epsilon(\tau_n)\, \mathcal{I}(\tau_n; \{\mathcal{T}_a^{\varepsilon}\})}{\int \mathrm{d}\tau'_n\, \rho_n(\tau'_n)\, \epsilon(\tau'_n)\, \mathcal{I}(\tau'_n; \{\mathcal{T}_a^{\varepsilon}\})} \tag{3.22}$$

Inserting this into Eq. (3.20) yields the extended likelihood function for the PWA model, with the expected number of events in the Poisson distribution given by Eq. (3.21),

$$\begin{aligned} \mathcal{L}_{\text{ext}}(\{\mathcal{T}_a^{\varepsilon}\}; \{\tau_{n,k}\}, N) &= \frac{(N_{\text{pred}}^{\text{meas}})^N\, \mathrm{e}^{-N_{\text{pred}}^{\text{meas}}}}{N!} \prod_{k=1}^{N} \frac{\rho_n(\tau_{n,k})\, \epsilon(\tau_{n,k})\, \mathcal{I}(\tau_{n,k}; \{\mathcal{T}_a^{\varepsilon}\})}{\int \mathrm{d}\tau'_n\, \rho_n(\tau'_n)\, \epsilon(\tau'_n)\, \mathcal{I}(\tau'_n; \{\mathcal{T}_a^{\varepsilon}\})} \\ &= \frac{\mathrm{e}^{-N_{\text{pred}}^{\text{meas}}}}{N!} \prod_{k=1}^{N} \rho_n(\tau_{n,k})\, \epsilon(\tau_{n,k})\, \mathcal{I}(\tau_{n,k}; \{\mathcal{T}_a^{\varepsilon}\}) \; . \end{aligned} \tag{3.23}$$

As the actual value of the likelihood function at the maximum is irrelevant for the parameter estimation, Eq. (3.23) can be simplified further by dropping all constant factors. To obtain a numerically better behaved expression, the logarithm of $\mathcal{L}_{\text{ext}}$ is used, which converts the product over the measured events into a sum. Furthermore, numerical methods traditionally find the minimum of a given function, which is why the negative log-likelihood function $-\ln \mathcal{L}_{\text{ext}}$ is minimized. The final expression for the likelihood function is

$$
\begin{aligned}
&-\ln \mathcal{L}_{\text{ext}}(\{\mathcal{T}_a^{\varepsilon}\}; \{\tau_{n,k}\}, N) \\
&\quad = -\sum_{k=1}^{N} \ln \mathcal{I}(\tau_{n,k}; \{\mathcal{T}_a^{\varepsilon}\}) - N_{\text{pred}}^{\text{meas}}(\{\mathcal{T}_a^{\varepsilon}\}) \\
&\quad = -\sum_{k=1}^{N} \ln \left[\sum_{\varepsilon=\pm 1} \left| \sum_{a}^{N_{\text{waves}}} \mathcal{T}_a^{\varepsilon} \Psi_a^{\varepsilon}(\tau_{n,k}) \right|^2 + |\mathcal{T}_{\text{flat}}|^2 \right] \\
&\qquad + \sum_{\varepsilon=\pm 1} \sum_{a,b}^{N_{\text{waves}}} \mathcal{T}_a^{\varepsilon} \mathcal{T}_b^{\varepsilon *} \underbrace{\int \mathrm{d}\tau_n \, \rho_n(\tau_n) \, \epsilon(\tau_n) \, \Psi_a^{\varepsilon}(\tau_n) \Psi_b^{\varepsilon *}(\tau_n)}_{= \, ^{\text{acc}}I_{ab}^{\varepsilon}} \\
&\qquad + |\mathcal{T}_{\text{flat}}|^2 \underbrace{\int \mathrm{d}\tau_n \, \rho_n(\tau_n) \, \epsilon(\tau_n)}_{= \, ^{\text{acc}}I_{\text{flat}}} \; .
\end{aligned}
\tag{3.24}
$$

As the transition amplitudes are independent of the phase-space variables τ_n, they can be pulled out of the integrals in Eq. (3.24). One can then construct the so-called *accepted integral matrix* in each m_X and t' bin, whose elements $^{\text{acc}}I_{ab}^{\varepsilon}$ are calculated by performing an integration of the decay amplitudes of two waves a and b over the accepted phase space $\mathrm{d}\Phi_n(\tau_n)\,\epsilon(\tau_n)$:

$$
^{\text{acc}}I_{ab}^{\varepsilon} \coloneqq \int \mathrm{d}\tau_n \, \rho_n(\tau_n) \, \epsilon(\tau_n) \, \Psi_a^{\varepsilon}(\tau_n) \Psi_b^{\varepsilon *}(\tau_n) \tag{3.25}
$$

and

$$
^{\text{acc}}I_{\text{flat}} \coloneqq \int \mathrm{d}\tau_n \, \rho_n(\tau_n) \, \epsilon(\tau_n) \; . \tag{3.26}
$$

Here, Eq. (3.9) has been used to replace $\mathrm{d}\Phi_n(\tau_n)$ by the density of states $\rho_n(\tau_n)\mathrm{d}\tau_n$. A special case is the *phase-space* integral matrix, where $\epsilon(\tau_n) = 1$, i.e.

$$
I_{ab}^{\varepsilon} \coloneqq \int \mathrm{d}\tau_n \, \rho_n(\tau_n) \, \Psi_a^{\varepsilon}(\tau_n) \Psi_b^{\varepsilon *}(\tau_n) \; . \tag{3.27}
$$

As was already discussed in Section 3.2.3, the decay amplitudes, and consequently the integrals $^{\text{acc}}I_{ab}^{\varepsilon}$ defined in Eq. (3.25), are formulated such that they do not contain any free parameters. It is therefore possible to precalculate the decay amplitudes at the phase-space coordinates $\tau_{n,k}$ of all measured events k. Also, the integral matrix can be precalculated using Monte Carlo integration methods (see Section 3.4) before maximizing the likelihood function in Eq. (3.24). This reduces the computation time needed to evaluate the likelihood function drastically and is required so that the maximization process becomes feasible in terms of computational resources. However, this approach has a severe downside: the dynamical amplitudes of all isobar resonances, and especially the propagator terms discussed in Section 3.2.4, have to be known exactly. One has to decide in advance not only which isobar resonances to include in the PWA model, but also which parameterizations and resonance parameters describe them best.

Maximizing Eq. (3.24) enforces that the number of measured events $N_{\mathrm{pred}}^{\mathrm{meas}}$ predicted by the model, defined in Eq. (3.21), and the actual measured number of events N are equal, i.e.

$$N_{\mathrm{pred}}^{\mathrm{meas}}(\{\mathcal{T}_a^{\varepsilon}\}) \equiv N \ . \tag{3.28}$$

This normalizes the intensity distribution $\mathcal{I}(\tau_n)$ such that it is given in numbers of produced events. An arbitrary scaling factor between the transition and decay amplitudes can be chosen such that the decay amplitudes satisfy

$$\int \mathrm{d}\Phi_n(\tau_n; m_X) |\Psi_a^{\varepsilon}(\tau_n; m_X)|^2 = 1 \ . \tag{3.29}$$

This fixes the unit of the transition amplitudes. Their squares, called *partial-wave intensities*, have the same unit as the intensity: they represent the expected number of produced events in wave a.

3.4 Monte Carlo Methods

The integral matrices defined in Eqs. (3.25) and (3.27) are precalculated using Monte Carlo integration techniques before performing the maximum-likelihood fit. To this end, N_{MC} Monte Carlo events, are generated uniformly in the n-body phase space of the final-state particles. The integral matrix element I_{ab} is approximated by

$$I_{ab} = \int \mathrm{d}\Phi_n(\tau_n) \Psi_a(\tau_n)\, \Psi_b^*(\tau_n) \approx \frac{V_n}{N_{\mathrm{MC}}} \sum_{k=1}^{N_{\mathrm{MC}}} \Psi_a(\tau_{n,k})\, \Psi_b^*(\tau_{n,k}) \tag{3.30}$$

where $V_n \coloneqq \int \mathrm{d}\Phi_n(\tau_n)$ is the n-body phase-space volume. To calculate the accepted integral matrix ${}^{\mathrm{acc}}I_{ab}$, a different Monte Carlo data sample, which has $N_{\mathrm{MC}}^{\mathrm{acc}}$ events and is weighted by the acceptance $\epsilon(\tau_n)$, must be used. To this end, the N_{MC} phase-space Monte Carlo events are processed through the simulation of the detector setup, the event reconstruction and the selection procedure, similarly to real data. Just like Eq. (3.30), the integrand is evaluated at those events, which gives

$$ {}^{\mathrm{acc}}I_{ab} = \int \mathrm{d}\Phi_n(\tau_n)\,\epsilon(\tau_n)\,\Psi_a(\tau_n)\,\Psi_b^*(\tau_n) \approx \frac{V_n}{N_{\mathrm{MC}}} \sum_{k=1}^{N_{\mathrm{MC}}^{\mathrm{acc}}} \Psi_a(\tau_{n,k})\,\Psi_b^*(\tau_{n,k}) \ . \tag{3.31} $$

The values of the matrix elements calculated using Eqs. (3.30) and (3.31), respectively, have statistical uncertainties. The Monte Carlo data samples must therefore be large enough so that the uncertainties become negligible compared to the statistical uncertainties of the data.

The Monte Carlo data samples also have additional applications. Using the generated and accepted phase-space events mentioned above, one can get an approximation of the acceptance

$$ \epsilon(m_X, t', \tau_n) \approx \frac{N_{\mathrm{MC}}^{\mathrm{acc}}(m_X, t', \tau_n)}{N_{\mathrm{MC}}(m_X, t', \tau_n)} \tag{3.32} $$

in bins of the kinematic variables (m_X, t', τ_n). Using a set of predetermined transition amplitudes $\{\mathcal{T}_a^\varepsilon\}$, e.g. from results of earlier experiments, weighted Monte Carlo events similar to real data can be generated. This is done by weighting the N_{MC} events with the intensity model in Eq. (3.17). These events can be used as pseudodata to study the partial-wave analysis method, because the expected outcome of the fit result, i.e. the set of transition amplitudes $\{\mathcal{T}_a^\varepsilon\}$, is known.

Part I

Partial-Wave Analysis and Monte Carlo Studies of the $K^-K^+\pi^-$ Decay Channel

Chapter 4

The $K^-K^+\pi^-$ Channel

The COMPASS collaboration has performed a detailed analysis of a large dataset of $\pi^- + p \to \pi^-\pi^+\pi^- + p$ diffractive dissociation reactions, where many 3π intermediate-state resonances (i.e. a_J and π_J resonances) have been studied [1–3]. Interesting discoveries have been made, such as a new axial-vector meson $a_1(1420)$ decaying into $f_0(980)\pi^-$, or the spin-exotic $\pi_1(1600)$ decaying into $\rho(770)\pi^-$. The reaction studied here, $\pi^- + p \to K^-K^+\pi^- + p$, is a partner channel to $\pi^-\pi^-\pi^+$ production because both initial and final states possess equal quantum numbers. Therefore, the same three-body resonances should be observable as intermediate states X^-.

However, compared to $\pi^-\pi^-\pi^+$ production, the reaction probability is suppressed kinematically because kaons have a larger mass than the pions ($m_{K^\pm} = 493.7$ MeV/c^2 versus $m_{\pi^\pm} = 139.6$ MeV/c^2). This leads to a higher three-body mass threshold $m^{\text{min}}_{KK\pi} = 2\ m_{K^\pm} + m_{\pi^\pm} = 1.127$ GeV/c^2 (cf. $m^{\text{min}}_{3\pi} = 0.4187$ GeV/c^2). This causes a suppression of ground-state resonances such as the $a_1(1260)$ and the $a_2(1320)$, which dominate the 3π channel and are already very well known. The $KK\pi$ channel hence enables the investigation of excited-state resonances, in particular resonances with higher spins J.

In addition, the $K^-K^+\pi^-$ channel has two distinct choices for the isobar ξ in the decay $X^- \to \xi + (\pi^- \text{ or } K^-)$. The isobar ξ can either decay into K^+K^- or into $K^+\pi^-$, as depicted in Fig. 4.1. This means that the $\rho(770)\pi$ decay mode, which has a large branching fraction for many 3π resonances, does not appear in $KK\pi$. This opens an opportunity to search for decay modes with smaller branching fractions and for decay modes into kaon resonances. The latter would provide insight into the $s\bar{s}$ content of the states, which would be interesting for example for the $\pi_1(1600)$. The $KK\pi$ channel also allows us to study decays with isobar resonances that couple more to K^+K^-, such as various f_0 resonances, which are candidates for exotic mesons. Particularly interesting is the $f_0(980) \to KK$ channel, where the elusive $a_1(1420)$ signal was found in the 3π data [1, 3].

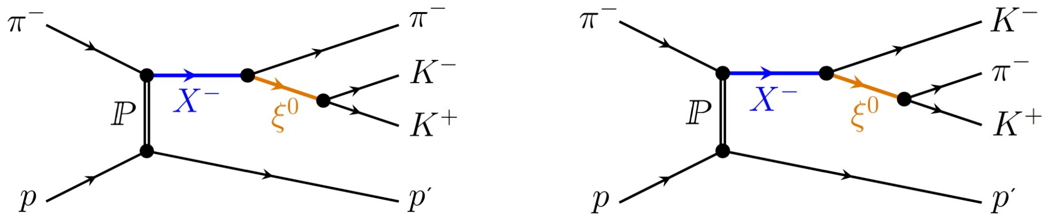

Figure 4.1: The two possible topologies for the X^- decay via an isobar ξ^0 , which is either a K^+K^- or a $K^+\pi^-$ resonance. From Ref. [7].

4.1 Selection of the $K^-K^+\pi^-$ Final State

The goal of the event selection is to select events corresponding to the inelastic scattering process

$$\pi^- + p \to K^- + K^+ + \pi^- + p$$

After reconstruction of the raw data, i.e. after translating the hits in the various detectors into particle tracks, cuts are applied to the data in order to obtain the desired final state. The selection criteria for the $K^-K^+\pi^-$ final state will be briefly described below. They were developed in Ref. [7]. A more in-depth description can be found there.

4.1.1 Selection of the Data

The following criteria are applied to the data:

- **Diffractive Trigger (DT0)**: The DT0 trigger consists of three independent trigger signals:
  - Beam particles set off a signal in scintillating fiber detectors installed upstream of the target. This ensures that the beam is centered.
  - The RPD trigger only leaves events where a proton is recoiling from the target after interaction.
  - A veto system suppresses events with non-interacting beam particles, events with beam particles far from their nominal trajectory, and events with final-state particles outside of the geometrical acceptance of the detector.
- **Exactly one primary vertex**: One primary vertex (i.e. point of interaction) between the beam particle and outgoing charged particles must

be present. If more than one primary vertex is detected, no clear assignment between incoming and outgoing particles is possible. Those events are discarded.

- **Vertex in target volume**: Events where the position of the primary vertex does not match the target volume are excluded. The vertex position must be inside $-65 < Z_{\text{PV}} < -30$ cm along the beam axis and the radial difference from the beam axis must satisfy $R_{\text{PV}} < 1.5$ cm.
- **Charge conservation**: There must be exactly three *charged* particles going out from the vertex position. Additionally, charge conservation with the incoming particle is enforced by requesting that the total charge of the final-state particles is equal to the charge of the beam particle, i.e. $\sum_i^3 Q_i = -1$.
- **Particle Identification**: Identification of the beam particle as well as the final-state particles is required. Beam particles are identified using the CEDAR detectors, while charged final-state particles are identified using the RICH-1 detector. Details will be discussed in the next section (Section 4.1.2).
- **Exclusivity cut**: Once all charged particles have been identified, processes with additional neutral hadrons, such as $\pi^- + p \to K^-K^+\pi^- + \pi^0\pi^0 + p$, still remain. Those are suppressed by demanding energy and momentum conservation, i.e. by comparing the beam energy to the final-state energy, as well as making sure the $K^-K^+\pi^-$ system and the recoil proton are emitted back-to-back in the plane perpendicular to the beam axis.
- **Track Time**: By using the time information of the detectors, background and pile-up are reduced.

After undergoing this selection process, the dataset includes 2.02×10^6 events.

4.1.2 Particle Identification

In order to select only events stemming from the diffractive dissociation reaction $\pi^- + p \to K^-K^+\pi^- + p$, the incoming beam particle as well as the three charged final-state particles have to be identified. The CEDARs mentioned in Section 2.1.1 are used to identify the beam particle as a pion, which make out most of the beam.

An identification of the charged final-state particles is imperative in order to separate the $K^-K^+\pi^-$ channel from the dominant process $\pi^- + p \to \pi^-\pi^+\pi^- + p$, which is much more frequent. According to Monte Carlo studies, a $\sim 9\%$ background of $\pi^-\pi^+\pi^-$ events remains after the PID in the analyzed kinematic range.

The Ring-Imaging Cherenkov (RICH-1) detector performing the identification of the charged final-state particles is described in Section 2.2. The identification is performed using the following procedure [7]: Each detected particle gets assigned a *particle species* S, where $S \in \{\pi, K, p, \text{background}\}$. The RICH-1 detector then gives the likelihood $P(S)$ that the particle is of particle species S. We define the likelihood ratio

$$R(S) = \frac{P(S)}{\max_{S' \neq S} P(S')} , \tag{4.1}$$

where $\max_{S' \neq S} P(S')$ is the maximum likelihood value for the particle species other than S. If R exceeds a certain pre-defined threshold T_{RICH}, i.e.

$$R(S) > T_{\text{RICH}} ,$$

the particle is assigned the PID S, else, no particle species is assigned. The threshold T_{RICH} has been chosen to ensure a high acceptance while keeping the mis-identification low [7]. Here, the same value $T_{\text{RICH}} = 1.15$ as in the analysis of the similar process $K^- + p \to K^-\pi^-\pi^+ + p$ [11, 12] was selected.

As the mis-identification of particles at higher momenta, especially at $|\vec{p}| > 60$ GeV/c, rises substantially and a correct assignment becomes increasingly rare, particle momenta are restricted to:

- $3 < |\vec{p}_\pi| < 60$ GeV/c
- $10 < |\vec{p}_K| < 60$ GeV/c
- $18 < |\vec{p}_p| < 100$ GeV/c

Ideally, all final-state particles are identified. However, as discussed in Section 2.2 and shown in Fig. 2.2, the RICH-1 detector can distinguish pions and kaons reliably only when they have a momentum $|\vec{p}| \lesssim 45$ GeV/c. As the beam momentum of $|\vec{p}_{\text{beam}}| = 190$ GeV/c is distributed among final state particles, all three particles being identified is kinematically excluded. Only a fraction of $K^-K^+\pi^-$ events are thus identified by the RICH-1 (Ref. [7] reports a phase-space acceptance lower than 10%, compared to the acceptance of 49% in the $\pi^-\pi^-\pi^+$ channel [2], where no final-state identification has to be made). In addition to the acceptance being low, it is also non-uniform in the phase-space variables, which causes a significant loss of events for certain decay angles. This is further discussed in Section 5.2.3. In order to distinguish the $K^-K^+\pi^-$ final state from $\pi^-\pi^+\pi^-$, we consider different combinations of particles that have to be identified in the RICH-1 detector, taking into account that the incoming beam particle has been identified as a pion by the CEDAR detectors.

- If one of the negative particles has been identified as a K^-, strangeness conservation restricts the positive particle to K^+ and conservation of isospin $I = 1$ from the beam pion forces the third particle to be a π^-.
- In case one of the negative particles cannot be identified by the RICH-1 as a K^-, the other two particles must be identified as π^- and K^+so that strangeness conservation forces the first particle to be the K^-.

4.2 Kinematic Distributions

This section presents the mass distributions of the $K^-K^+\pi^-$ system and its subsystems, as well as the distribution of the squared momentum transfer t'. Some of the resonances present in the intermediate states X^- can already manifest themselves as structures in the $K^-K^+\pi^-$ three-body-mass distribution. Examining the distribution may hence give indications as to what partial waves to expect. Additionally, analyzing the two-body-mass distributions of the subsystems for resonances is essential, as the isobar model (see Section 3.2.1) assumes perfect knowledge of the resonances present in the different subsystems. These distributions may give indications as to which isobar resonances to include in the PWA model in order for it to be able to reproduce the data.

4.2.1 $K^-K^+\pi^-$ Mass Distribution

Figure 4.2 shows the mass distribution of the $K^-K^+\pi^-$ system. It rises steeply in the range from approximately 1.4 GeV/c^2 to 1.8 GeV/c^2. At the latter mass, the distribution features a first broad peak. The distribution peaks again around 2.2 GeV/c^2, before decreasing slowly towards higher masses without visible structures. As there are only few events below 1.5 GeV/c^2 due to the low acceptance, the mass range of the analysis is constrained to $m_{KK\pi} > 1.5$ GeV/c^2, as indicated by the left orange vertical line in Fig. 4.2.

Unfortunately, this renders a search for the narrow $a_1(1420)$ resonance mentioned in the introduction to Chapter 4 futile. No established states are listed in the Particle Data Group (PDG) [13] at masses higher than 2.5 GeV/c^2. In order to accommodate for possible findings at higher masses, the upper limit is set at $m_{KK\pi} = 3.5$ GeV/c^2.

The $K^-K^+\pi^-$ mass distribution does not exhibit any fine structures that may hint at specific a_J or π_J resonances present as intermediate X^- state. Only two broad peaks at $m_{KK\pi} \simeq 1.8$ GeV/c^2 and $m_{KK\pi} \simeq 2.2$ GeV/c^2 are present in the mass distribution. Two known resonances, $\pi(1800)$ and $\pi_2(1880)$, could cause the former. For the latter however, the PDG does not list established states with matching quantum numbers. In the absence of any clear signals in the distribution, the resonance content of the $K^-K^+\pi^-$ system thus has to be investigated using partial-wave analysis.

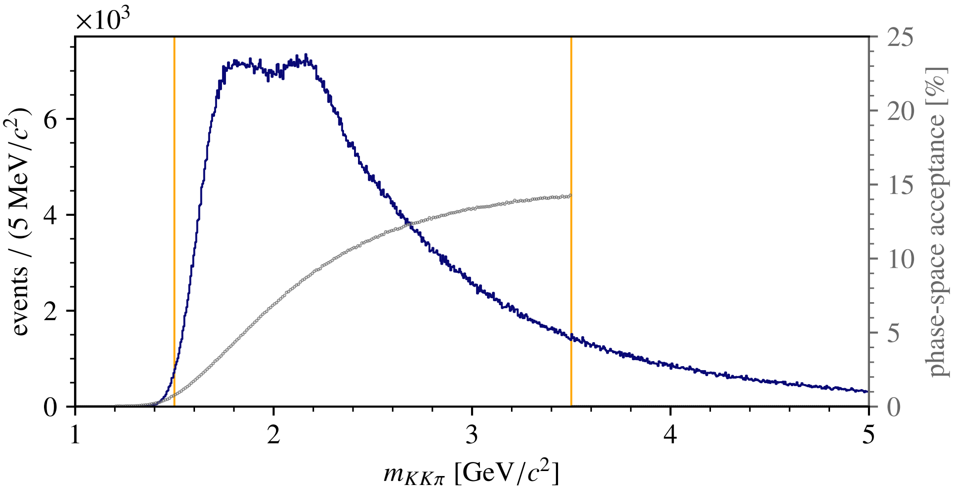

Figure 4.2: Mass distribution of the $K^-K^+\pi^-$ system. The mass range chosen in the analysis is indicated by the vertical orange lines. The acceptance in the $K^-K^+\pi^-$ mass is additionally plotted in grey.

As discussed in Section 3.3.2, the analysis is performed in bins of the $K^-K^+\pi^-$ mass. The mass range $1.5 < m_{KK\pi} < 3.5$ GeV/c^2 is divided into 100 equidistant mass bins, each of 20 MeV/c^2 width.

4.2.2 Two-Body Mass Distributions

The two-body mass distributions of the K^+K^- and $K^+\pi^-$ subsystems are shown in Fig. 4.3. The mass distribution of $K^-\pi^-$ is not shown because it features no visible structures, as expected. Any resonance decaying into $K^-\pi^-$ would have a charge $Q = -2$ and would thus be flavor-exotic. The mass distributions of the other two subsystems show clear structures, corresponding to isobar resonances that decay into $K^+\pi^-$ or K^+K^-, respectively. A prominent narrow peak at $m_{K\pi} \approx 900\ \text{MeV}/c^2$ indicates the presence of the well-known $K^*(892)$. A second, broader peak at about $1.4\ \text{GeV}/c^2$ could be attributed to either the $K_0^*(1430)$ or the $K_2^*(1430)$. In the K^+K^- subsystem, the $\phi(1020)$ can be discerned as a small, narrow spike right above $1\ \text{GeV}/c^2$. It is suppressed because the intermediate state decaying into $\phi(1020)\pi^-$ cannot be produced by the dominant Pomeron exchange and must therefore originate from a different process. The most dominant, rather broad peak at $1.3\ \text{GeV}/c^2$ lies in the mass range of the $f_2(1270)$ and the $f_0(1370)$. A third peak above $1.5\ \text{GeV}/c^2$ might stem from the $f_0(1500)$ or the $f_2'(1525)$. No further peak-like structures are observed above this mass.

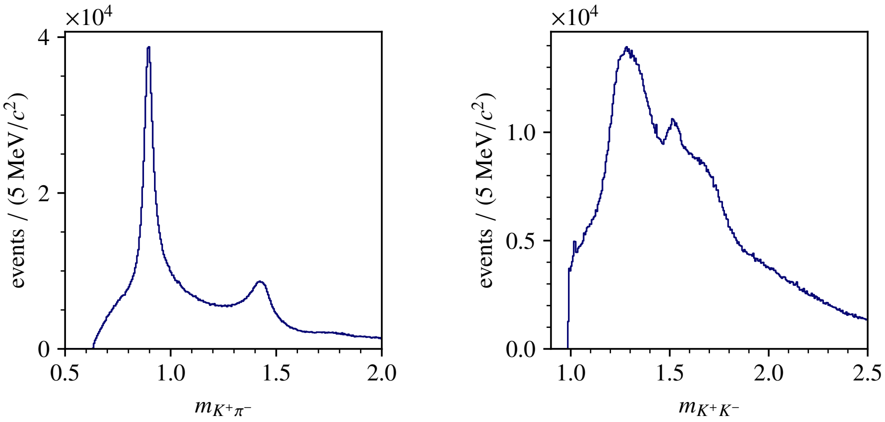

Figure 4.3: Mass distributions of the $K^+\pi^-$ (left) and K^+K^- (right) subsystems.

4.2.3 Distribution of Squared Four-Momentum Transfer

The reduced four-momentum transfer squared t' between beam particle and X^- is defined in Eq. (3.6). Figure 4.4 shows the t' distribution of the data in logarithmic scale, with orange lines indicating the range used in the analysis. An approximately exponentially falling t'-dependence of the data is expected, which is consistent with the measured distribution. As the proton needs a minimal kinetic energy in order to trigger a signal in the Recoil Proton Detector, a lower limit of $t' > 0.1\ (\text{GeV}/c)^2$ is required. An upper limit of $t' < 1.0\ (\text{GeV}/c)^2$ is set because of the vanishing number of events at higher t' values.

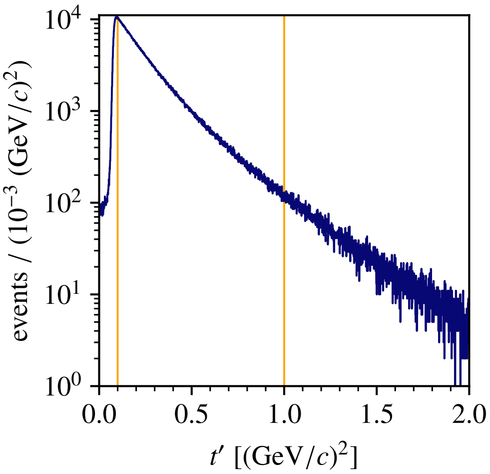

Figure 4.4: t' distribution in logarithmic scale. The t' range chosen in the analysis is indicated by the vertical orange lines.

The t' range of the analysis, $0.1 < t' < 1.0\ \text{GeV}/c^2$, is subdivided into four non-equidistant bins such that the first two bins each contain approximately 1/3 of the total number of events and the last two bins each 1/6. Their borders are listed in Table 4.1

Bin		1		2		3		4	
t' [(GeV/c)^2]	0.10		0.15		0.24		0.34		1.00

Table 4.1: The four t' bins used in the analysis.

Chapter 5

$K^-K^+\pi^-$ Studies

5.1 A First Partial-Wave Decomposition

The goal of this section is to present a first partial-wave decomposition of the COMPASS data on $\pi^- + p \to K^-K^+\pi^- + p$ and to compare the results to those of previous analyses of the same final-state, especially to the results of the partial-wave analysis of the VES collaboration on the reaction $\pi^- + \mathrm{Be} \to K^-K^+\pi^- + \mathrm{Be}$ published in 1994 [14]. This analysis was conducted with a different target and at a lower beam momentum, as well as in a slightly narrower mass range, but is otherwise identical. As discussed in Chapter 3, we decompose the amplitude for the process $\pi^- + p \to K^-K^+\pi^- + p$ into partial-wave amplitudes with well-defined quantum numbers and decay chains.

5.1.1 Partial-Wave Model

As a first attempt, we employ the same waveset as was used by the VES analysis. Table 5.1 lists the waveset used in this first partial-wave decomposition. To define waves, we use the shorthand notation $J^PM^\epsilon\ \xi\ \mathrm{b}\ L$, with the quantum numbers of the intermediate state X,[1] i.e. the total spin J, parity P, spin projection M, reflectivity ϵ, and the isobaric decay described by the isobar resonance ξ, the bachelor particle b and the angular momentum L between the two (see also Eq. (3.14)). The waveset contains 13 waves, 12 of which have unnatural spin-parity and one with natural spin-parity which in addition has spin-exotic quantum numbers, plus a phase-space-isotropic flat wave included to absorb incoherent backgrounds (see Section 3.3.3).

As isobar resonances for the KK subsystem, we include the $[KK]_S$ S-wave, which is a special parametrization of the $J^P = 0^+$ $f_0(500)$ state (see Section 3.2.4 on the parameterization of the propagator terms of isobar reson-

---

[1] The initial state π^- has $I^G = 1^-$ and C parity $+1$. Because of conservation of isospin, C and G parity, this is also valid for all intermediate states. Isospin, C and G parity will thus be omitted in the wave notation.

ances), and the $f_2(1270)$ with $J^P = 2^+$. The $J^P = 0^+$ content of the $K\pi$ subsystem is described by the LASS parameterization $[K\pi]_S$ including the states $K_0^*(700)$ and the $K_0^*(1430)$ [15]. Additionally, we include the well-known $K^*(892)$ resonance clearly observed in the $K\pi$ mass distribution in Section 4.2.2 and the $K_2^*(1430)$ resonance.

The analysis mass range of $1.5 < m_{KK\pi} < 3.5$ GeV/c^2 is subdivided into 100 equidistant mass bins with 20 MeV/c^2 bin width. This is different from the VES analysis, which analyzed the narrower mass range $1.2 < m_{KK\pi} < 2.4$ GeV/c^2 with 40 MeV/c^2 wide mass bins. Additionally, the VES data lies at low t' because of the heavier target used, and thus is not binned in t', while the COMPASS data has been subdivided into four t' bins listed in Table 4.1. The partial-wave analysis is performed independently in each $m_{KK\pi}$ and t' bin, as discussed in Section 3.3.4.

5.1.2 Partial-Wave Intensities

The resulting partial-wave intensities are shown as a function of $m_{KK\pi}$ in Fig. 5.1 in blue. They are summed over all four t' bins. The percent number in the top-right corner of each intensity distribution is the relative intensity of the partial wave. The relative intensity is defined as the ratio of the partial-wave intensity integrated over the analysed mass and t' range to the integral of the total intensity. The latter corresponds to the total number of acceptance-corrected events. Due to interference of the waves, the sum of the relative intensities may differ from 100%. In our case, the difference amounts to 11%. This difference is a measure for the net interference of the waves. For comparison, the results from the VES analysis in Ref. [14] are superimposed as orange data points. The VES points are scaled to match the total acceptance-corrected intensity of the COMPASS fit and to account for the different mass bin widths. Data points that lie outside of the chosen ordinate range are indicated by orange arrows. The uncertainties of the VES measurements, which in some cases are substantial, are omitted.

1	0^-0^+ $[K\pi]_S$ K^- S	4	1^+0^+ $K^*(892)$ K^- S	8	2^-0^+ $K_2^*(1430)$ K^- S
2	0^-0^+ $[KK]_S$ π^- S	**5**	1^+0^+ $[K\pi]_S$ K^- P	**9**	2^-0^+ $f_2(1270)$ π^- S
3	0^-0^+ $K^*(892)$ K^- P	**6**	1^+0^+ $[KK]_S$ π^- P	10	2^-0^+ $K^*(892)$ K^- P
		7	1^+0^+ $K^*(892)$ K^- D	**11**	2^-0^+ $[K\pi]_S$ K^- D
12	3^+0^+ $K^*(892)$ K^- S	13	1^-1^+ $K^*(892)$ K^- P		

Table 5.1: Partial waves used in VES analysis [14]. See text for notation.

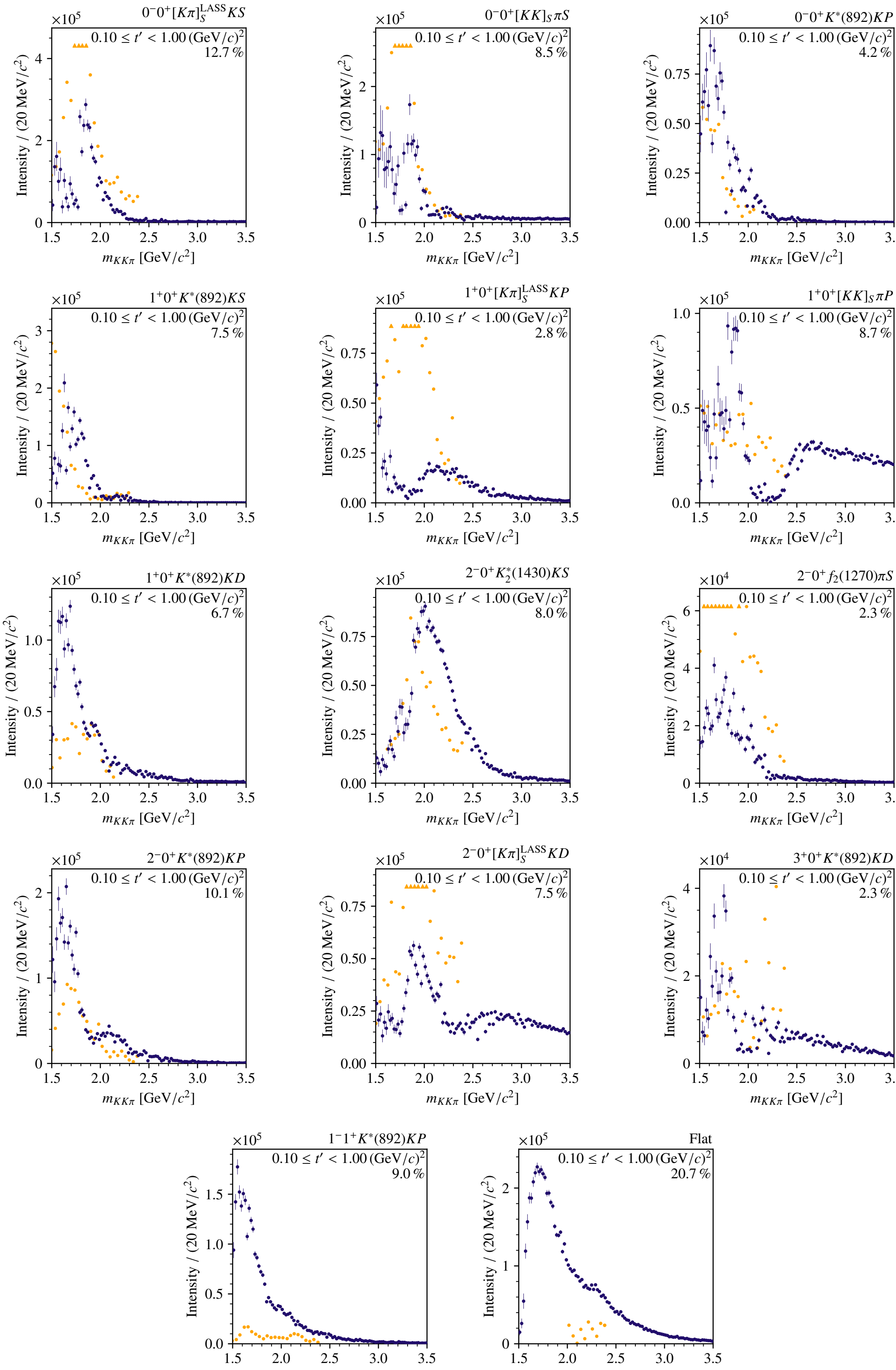

Figure 5.1: Partial-wave intensities, summed over all t' bins. COMPASS results (blue) vs. VES results (orange) from Ref. [14]. The percent number in the top-right corner is the relative intensity of the wave (see text).

5.1.3 Discussion

First of all, the partial-wave intensities are expected to form a smooth distribution, but the obtained intensity distributions of many waves exhibit a significant lack of continuity, especially visible at lower masses. In the $2^-0^+f_2(1270)\pi S$ wave e.g., the intensity in adjacent mass bins does not seem to follow a continuous structure. Another example for this behaviour is the $1^+0^+K^*(892)KS$ wave. The observed fluctuations are larger than expected from uncertainties.

Another worrying fact is that expected resonances are missing in several waves. As mentioned in Chapter 4, the same resonances are expected to appear in the reaction $\pi^- + p \to \pi^-\pi^-\pi^+ + p$ and in $\pi^- + p \to K^-K^+\pi^- + p$. The results of the COMPASS analysis of the former channel are shown in Fig. 5.2 for two waves contained in both the waveset employed in the $\pi^-\pi^-\pi+$ analysis and the waveset in Table 5.1. The $\pi(1800)$ state is observed as a clear peak in the $\pi^-\pi^-\pi^+$ $0^-0^+[\pi\pi]_S\pi S$ wave and should therefore also appear in the equivalent $0^-0^+[KK]_S\pi S$ wave. However, the intensity distribution of this wave presents no such structure around 1.8 GeV/c^2 other than a slight rise in intensity, creating a much narrower peak-like structure at about 1.90 GeV/c^2, which does not agree well with a $\pi(1800)$ signal. Similarly, the $\pi_2(1670)$ resonance is present as a prominent peak in the $2^-0^+f_2(1270)\pi S$ wave in the $\pi^-\pi^-\pi^+$ channel, but the wave's intensity distribution in the $K^-K^+\pi^-$ channel is devoid of any clear peak-like structure.

A further indication of the unreliability of the PWA fit is the very large relative intensity of the flat wave of 20.7%, making it the wave with the largest intensity in the waveset. The flat wave is a phase-space-isotropic distribution, as explained in Section 3.3.3, and should have a relative intensity in the order of at most a few percent. Its intensity distribution should not exhibit any particular structures. In our fit however, the intensity distribution of the flat wave also shows pronounced substructure with a large peak between 1.6 and 1.8 GeV/c^2 and a second one around 2.3 GeV/c^2. Intensity thus seems to be redistributed from other waves into the flat wave, which suggests that, to the fit, the phase-space distributions of some waves appear nearly isotropic.

Using the same waveset as the analysis of the VES collaboration enables a wave-by-wave comparison of the intensity distributions. While minor differences between the COMPASS and the VES results are to be expected, the intensity distributions in the common mass range of both analyses $1.5 < m_{KK\pi} < 2.4$ GeV/c^2 and the observed structures should be very similar. However, the agreement between the two analyses results varies from wave to wave and also depends significantly on the $K^-K^+\pi^-$ mass range. One can

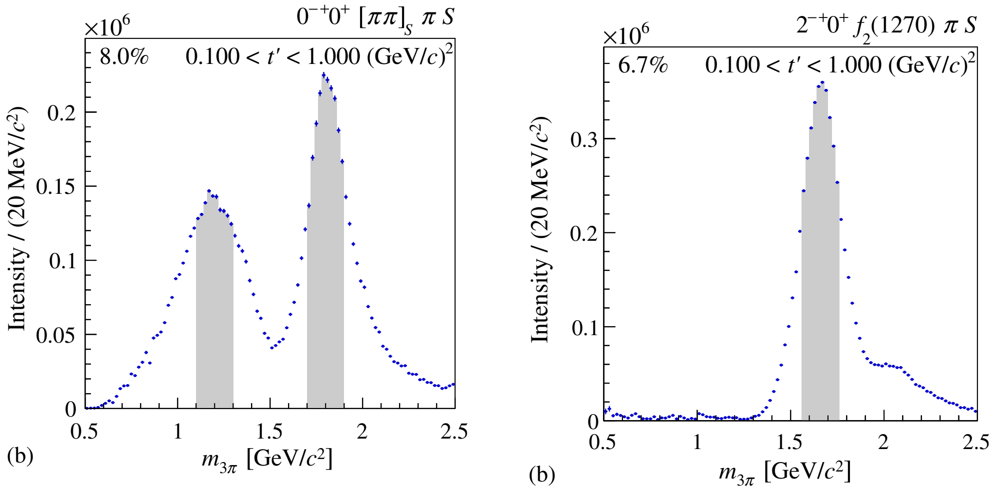

Figure 5.2: Partial-wave intensities of the $0^{-}0^{+}[\pi\pi]_S\pi S$ (left) and the $2^{-}0^{+}f_2(1270)\pi S$ (right) waves from the COMPASS analysis of $\pi^- + p \to \pi^-\pi^-\pi^+ + p$ [1].

distinguish three different cases: First, in certain waves, the intensity distributions contain less events below 2 GeV$/c^2$. This is the case for the two $J^P = 0^-$ waves with $[K\pi]_S$ and $[KK]_S$ isobars. In the VES analysis, the intensity distributions of the waves show a clear peak at 1.8 GeV$/c^2$ which can be attributed to the prominent $\pi(1800)$ resonance. The intensity distributions of the COMPASS data seem to follow the high-mass tail of the $\pi(1800)$, but in the $m_{KK\pi}$ region below 2 GeV$/c^2$, the intensity is considerably lower than in the VES results. A similar behavior is observed in the $1^{+}0^{+}[K\pi]_S KP$, $2^{-}0^{+}[K\pi]_S KD$ and $2^{-}0^{+}f_2(1270)\pi S$ waves. In the latter, the VES analysis identifies the $\pi_2(1670)$ resonance also seen in the COMPASS $\pi^-\pi^-\pi^+$ analysis.

The missing intensity seems to reappear in other waves. The $1^{+}0^{+}K^{*}(892)KD$ and $2^{-}0^{+}K^{*}(892)KP$ waves contain more events than the intensity distributions of the VES results especially below $m_{KK\pi} < 2$ GeV$/c^2$. In the first of those two waves, a peak can be seen in the intensity distribution that is absent from the VES counterpart. The high relative intensity of 9.0% of the $1^{-}1^{+}K^{*}(892)KP$ wave is also surprising, as intermediate states contained therein would be spin-exotic and should have minor contributions in comparison with the other waves. At certain masses, the intensity is up to 7-8 times higher than in the VES analysis, in which the $J^P M^\epsilon = 1^{-}1^{+}$ wave only contains little intensity. At least some of the higher intensity can however be explained by difference in t' of both analyses. Waves with spin projection $M = 1$ are suppressed at low t' and thus in the VES data, which has $t' < 0.08$ (GeV/c)^2, while the COMPASS data is taken at higher $0.1 < t' < 1.0$ (GeV/c)^2.

The intensity distributions of two waves, $1^+0^+[KK]_S\pi S$ and $3^+0^+K^*(892)KD$, actually look relatively similar to those of the VES analysis, or are at least in rough agreement especially considering the high uncertainties of the VES measurement. However, no resonance is observed in those waves in either analysis.

Apart from these three situations, two special cases can be distinguished. The $2^-0^+K_2^*(1430)KS$ wave features a rather clear peak-like structure that is much broader than the very narrow peak in the VES intensity distribution. This wave could contain e.g. the $\pi_2(1880)$ resonance. The observed peak however lies at higher masses of about 2.1 GeV/c^2. It is thus unclear if this peak is caused by a resonance, and if yes, which it could be. A second special case is the flat wave, which high intensity was already discussed above. The VES analysis only has flat wave intensity at $m_{KK\pi} > 2$ GeV/c^2, when the quality of their fit becomes worse, essentially because of the absence of a reliable parametrization of the K^+K^- subsystem at higher m_{KK}. Even at this mass range $2.0 < m_{KK\pi} < 2.4$ GeV/c^2, the flat wave intensity of the VES analysis is smaller than in the COMPASS fit.

To recapitulate, the presented partial-wave decomposition fit seems to have significant problems especially in the lower mass range from 1.5 GeV/c^2 to about 2.0 GeV/c^2. The resulting intensities show a lack of continuity in many waves. Additionally, the flat wave has a high intensity and structure, whereas expected structures, such as the $\pi(1800)$ resonance, are absent from our results. There are significant discrepancies with the $K^-K^+\pi^-$ analysis of the VES collaboration [14]. It thus seems that the fit cannot reliably estimate the values of the transition amplitudes $\mathcal{T}_a$.

5.1.4 Distinguishability and Integral Matrix

The findings discussed in Section 5.1.3 point towards a consequential leakage of intensity between the waves. This indicates that the fit seems to have difficulties to distinguish different waves and thus to correctly determine the values of their transition amplitudes. This distinguishability issue may arise if the kinematic distributions of waves in the phase-space variables τ_3 that are described by the decay amplitudes $\Psi_a(\tau_3; m_{KK\pi})$ become too similar, i.e. when the decay amplitudes are not orthogonal. This possibility is further supported by the large flat-wave intensity. A measure for this similarity of two waves a and b is the modulus of the corresponding element of the phase-space integral matrix defined in Eq. (3.27):

$$|I_{ab}(m_{KK\pi})| = \left| \int \mathrm{d}\tau_3 \, \rho_3(\tau_3; m_{KK\pi}) \, \Psi_a(\tau_3; m_{KK\pi}) \Psi_b(\tau_3; m_{KK\pi}) \right| \tag{5.1}$$

A modulus of 0 means that the decay amplitudes of the two waves are orthogonal, while a modulus of 1 indicates that the decay amplitudes are identical so that the waves become indistinguishable mathematically.[2]

As the integral matrix in Eq. (5.1) depends on $m_{KK\pi}$, one can calculate one matrix for each mass bin. In order to investigate the $m_{KK\pi}$ dependence, the left column of Fig. 5.3 shows $|I_{ab}|$ for the set of 13 waves listed in Table 5.1 for two mass bins in the low-t' region. The first mass bin in the range $1.80 < m_{KK\pi} < 1.82\ \mathrm{GeV}/c^2$ has been chosen to probe the distinguishability of waves in the region in which two resonances $\pi(1800)$ and $\pi_2(1880)$ are expected, and where large deviations from the VES analysis are observed in the data. The second bin in the range $2.20 < m_{KK\pi} < 2.22\ \mathrm{GeV}/c^2$ lies in the region of better agreement with the VES analysis, and also in a region where resonances are still expected. The waves are represented by numerical indices ranging from 1 to 13 as given in Table 5.1. Since I_{ab} is Hermitian, $|I_{ab}|$ is symmetric.

The phase-space integral matrix has mostly elements with a modulus close to zero. This means that many waves are distinguishable, at least in principle. However, some waves have non-zero matrix elements, especially $I_{1,2}$ between the $0^-0^+[K\pi]_S KS$ and the $0^-0^+[KK]_S\pi S$ wave has a large modulus of about 0.8. Hence, both waves have similar phase-space distributions and may therefore be hard to distinguish even with perfect acceptance. The second-largest element is $|I_{9,11}|$ with a modulus of 0.5, which indicates that the fit might have difficulties distinguishing the $2^-0^+ f_2(1270)\pi S$ and the $2^-0^+[K\pi]_S KD$ wave. All other elements have moduli below 0.4.

While the moduli of most elements of the phase-space matrix are zero, the structure of the integral matrix changes significantly when acceptance comes into play. The accepted integral matrix

$$\begin{aligned} &|{}^{\mathrm{acc}}I_{ab}(m_{KK\pi}, t')| \\ &\quad = \left| \int \mathrm{d}\Phi(\tau_3; m_{KK\pi}) \, \epsilon(\tau_3; m_{KK\pi}, t') \, \Psi_a(\tau_3; m_{KK\pi}) \Psi_b(\tau_3; m_{KK\pi}) \right| \end{aligned} \tag{5.2}$$

with $\epsilon(\tau_3; m_{KK\pi}) < 1$, defined in Eq. (3.25), takes into account effects from the acceptance of the experiment in the phase-space variables. If these effects

---

[2] Due to the normalization of the decay amplitudes, the diagonal elements I_{aa} are all 1.

render some partial-wave amplitudes harder to distinguish, for example because the acceptance in certain phase-space regions in which the amplitudes differ is low, and the angular distribution is thus suppressed, the corresponding off-diagonal element becomes > 0. The right column of Fig. 5.3 shows $|{}^{\mathrm{acc}}I_{ab}(m_{KK\pi}, t')|$ in the two mass bins discussed above. Waves that already had high matrix elements, such as $0^-0^+[K\pi]_S KS$ and $0^-0^+[KK]_S \pi S$, become even more similar, i.e. $|{}^{\mathrm{acc}}I_{1,2}|$ is even closer to unity. What is worse, however, is that many other elements become large as well, which means that the ability of the fit to differentiate between those waves becomes significantly worse when the acceptance is taken into account. This is further visible in Fig. 5.4, in which histograms of the matrix elements are plotted for the phase-space and the accepted integral matrices.[3] One can clearly see that the accepted integral matrix possesses many more elements with high absolute values. The acceptance thus has a considerable effect on the distinguishability of the waves and hence the fit reliability. This effect will be further discussed in Section 5.2.3.

Comparing the matrix elements in the two mass bins $1.80 < m_{KK\pi} < 1.82\ \mathrm{GeV}/c^2$ and $2.20 < m_{KK\pi} < 2.22\ \mathrm{GeV}/c^2$ shows that for both I_{ab} and ${}^{\mathrm{acc}}I_{a,b}$, the moduli of the off-diagonal elements increase at lower masses. This means that the orthogonality of the waves improves toward higher masses. This is consistent with results from the comparison with the VES data discussed above. However, the distinguishability issues in the fit are still significant even at higher $K^-K^+\pi^-$ masses.

To conclude, the first partial-wave decomposition of the COMPASS $K^-K^+\pi^-$ dataset shown in Fig. 5.1 brings to light significant issues with the fit, especially large leakage of intensity between the partial waves. These findings are supported by the study of the integral matrices shown in Fig. 5.3, which uncovered the inability of the fit to distinguish between certain partial waves, especially at lower masses and because of the detector acceptance. The ability of the fit to reliably extract partial-wave amplitudes from the data and the effects of the acceptance thereon have to be investigated further. Therefore, studies with Monte Carlo pseudodata are performed and discussed in the next section.

---

[3] Only the elements from the lower triangle of the Hermitian matrices, and without the main diagonals, have been plotted

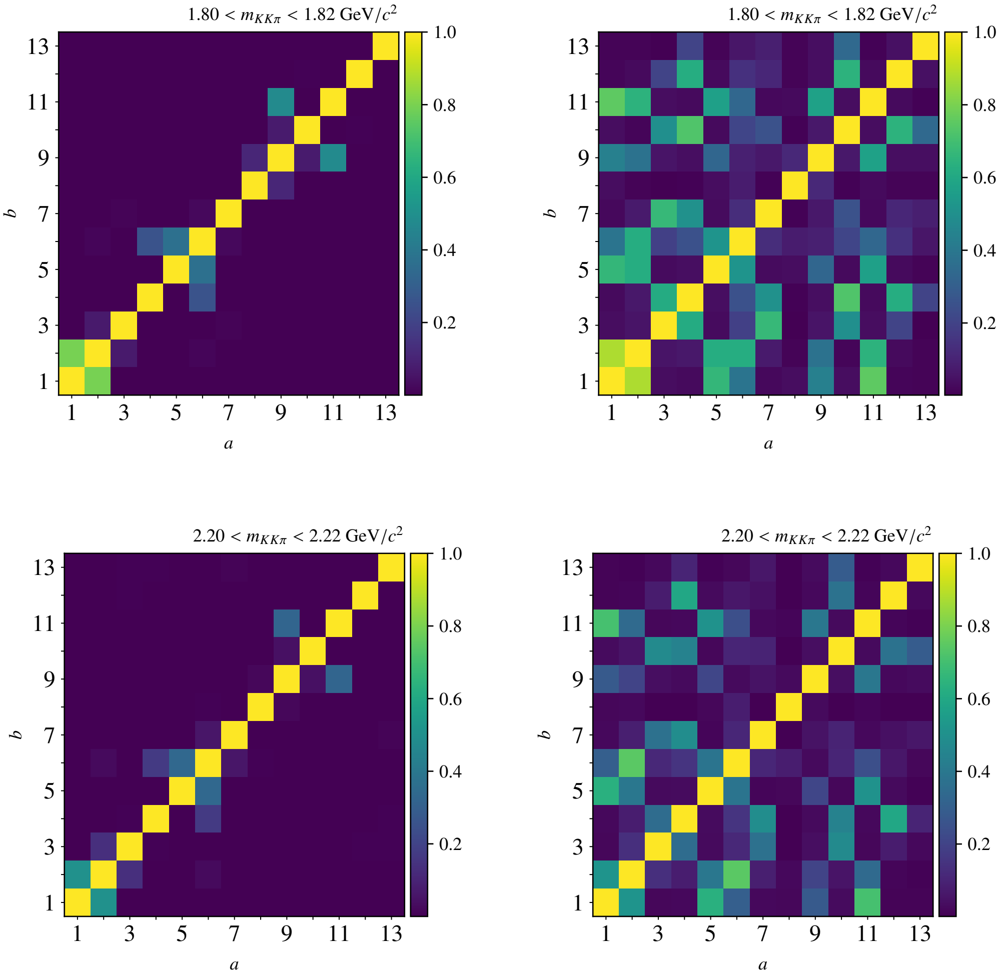

Figure 5.3: Integral matrix elements $|I_{ab}|$ (left column) and $|^{\mathrm{acc}}I_{ab}|$ (right column) in two different mass bins (rows) and for $0.10 < t' < 0.15$ $(\mathrm{GeV}/c)^2$.

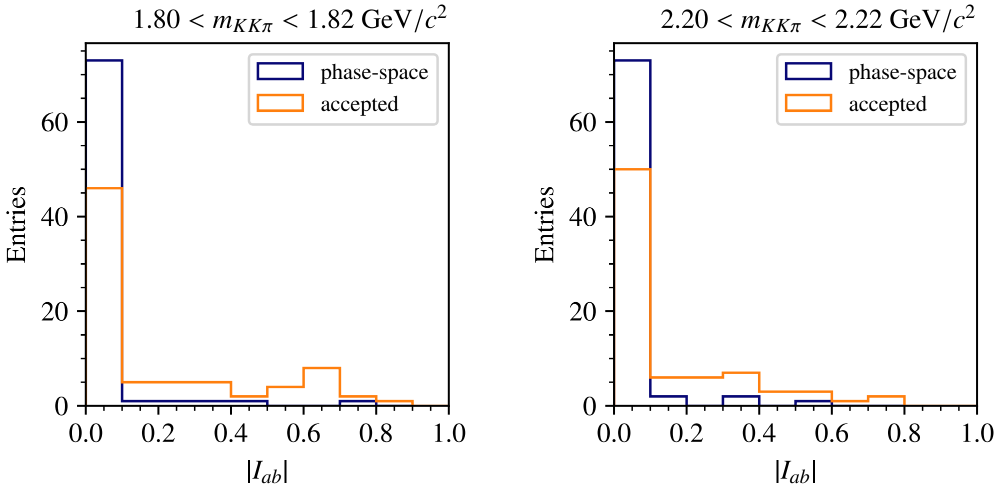

Figure 5.4: Histograms of the moduli of the phase-space and accepted integral matrix elements $|I_{ab}|$ in two different mass bins and for $0.10 < t' < 0.15$ $(\mathrm{GeV}/c)^2$.

5.2 Pseudodata Studies

In this section, the partial-wave decomposition procedure is applied to two sets of artificially-generated Monte Carlo (MC) pseudodata with known partial-wave content. This allows us to compare the transition amplitudes estimated by the fit with the corresponding amplitudes that were used to generate the MC data, and thus to study the reliability of the PWA fit procedure in the $\pi^- + p \to K^-K^+\pi^- + p$ channel. In Section 5.2.1, we first discuss how the two MC datasets were generated. The acceptance and its distribution in the phase-space variables is examined in detail in Section 5.2.3. Results of the analyses of the two MC datasets are presented in Sections 5.2.2 and 5.2.4.

5.2.1 Generation of the Monte Carlo Pseudodata

In order to generate the pseudodata, first, Monte Carlo events with an uniform distribution in phase space are generated, similar to those used for the calculation of the phase-space integral matrix in Section 3.4. These events are then weighted with the intensity model in Eq. (3.17) in order to resemble real events produced by the investigated process. To generate data according to this model, values for the transition amplitudes $\mathcal{T}_a$ of chosen partial waves a are needed as input. The choice of transition amplitudes will now be presented. In order to make the distribution as realistic as possible, the complex-valued transition amplitudes of each wave are taken from the results of the VES analysis [14] presented in Section 5.1, by combining their measured intensity and phase values. For practical reasons, only a subset of waves from the VES analysis waveset are included. The six selected partial waves are marked by bold indices in Table 5.1. They correspond to the waves with the highest intensities in the considered mass range and they also include clear resonance structures. They have X^- quantum numbers $J^P = 0^-$, 1^+ and 2^-, and include mainly KK and $K\pi$ S-wave isobars, with the exception of one wave with the $f_2(1270)$ as isobar resonance.

We study four exemplary 20 MeV/c^2 wide mass bins, all in the low t' region $0.1 < t' < 0.15$ (GeV/c)^2 as the t' dependence plays only a minor role for our studies. The mass-bin centers located at $m_{KK\pi} =$ 1.61, 1.81, 2.01, and 2.21 GeV/c^2 cover different resonance regions and regions with different detector acceptance. The mass bins at 1.81 and 2.21 GeV/c^2 have already been presented in Section 5.1.4. The additional bin at 1.61 GeV/c^2 helps us to investigate the behavior at very low masses, close to the point where the acceptance vanishes, while the bin at 2.01 GeV/c^2 is located at intermediate masses and helps us to better interpolate between the 1.81 and 2.21 GeV/c^2 bins. Following the above prescription, we obtain the first MC dataset with 1.77×10^6 events, which are distributed in the four mass bins according to the intensity model with known input values of the transition amplitudes. These events essentially correspond to the produced events in real data, i.e. the real events that would be measured by a detector with a perfect acceptance. The intensity distribution is shown in Fig. 5.5a.

A second set of pseudodata is generated by incorporating in addition the effects of the acceptance ϵ of the setup. This is done by processing the generated MC events of the first sample through the detector simulation, the event reconstruction and the selection chain similar to the processing of real data.[4] Doing this drastically reduces the number of events down to a set of 108 000 MC events. As expected, the intensity distribution in the considered mass bins changes, which can be seen in Fig. 5.5b. The events in each mass bin follow the distribution of $\epsilon(\tau_3)\,\mathcal{I}(\tau_3)$, and the number of events in each bin is given by Eq. (3.21). This second MC dataset enables us to study the effects of the acceptance on the fit procedure.

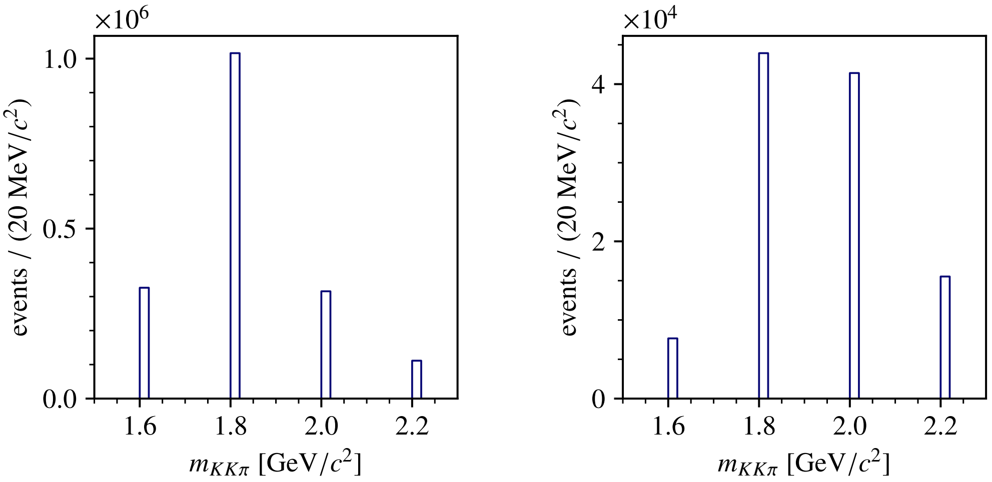

(a) Generated pseudodata.

(b) Accepted pseudodata.

Figure 5.5: Mass distributions of the two sets of Monte Carlo pseudodata.

---

[4] This is also similar to the processing of the Monte Carlo events used for the calculation of the accepted integral matrix in Section 3.4.

5.2.2 Pseudodata Fits with Perfect Acceptance

The first study that can be performed is to simply test the PWA fit procedure with the first set of MC pseudodata that does not include the detector acceptance, i.e. we study the case of perfect acceptance $\epsilon = 1$. First, we perform a PWA fit using exactly the same set of six waves as was used to generate the MC data. However, in the PWA of the real data, the exact partial-wave content of the data is a-priori unknown and the chosen waveset thus cannot be perfectly accurate. To study such a scenario, we perform a second PWA fit with a waveset that includes more waves than the six waves with which the MC pseudodata were generated.

In this section, one fit result with the exact set of waves and one fit with an extended set will be presented. Instead of fitting the entire dataset of 1.77×10^6 events, the two following fits are performed on a smaller subsample of 108 000 events in order to be able to roughly compare the results with those of later fits performed on the accepted MC pseudodata events (see Section 5.2.4).

5.2.2.1 Fits with the Exact Waveset

Figure 5.6 shows the results from a PWA fit with perfect acceptance in the four mass bins including only those six waves into the PWA model that are actually present in the data. Note that one wave is chosen to serve as a reference for the phases of the other waves and thus has a real-valued transition amplitude.

One can see in all four mass bins that the transition amplitudes estimated by the fit are similar to the input values. Overall, the fit seems to attribute the values of the transition amplitudes correctly. However, there are still small differences between the input values and the fit output. A measure to quantify those differences is the *chi-square value* χ^2 of the transition amplitudes. It is calculated from the squared differences of the values $\{y_i\}$ of the fit parameters, which are the real and imaginary parts of the transition amplitude values given by the fit, i.e. $\{y_i\} = \{\mathrm{Re}(\mathcal{T}_a^{\mathrm{fit}}),\ \mathrm{Im}(\mathcal{T}_a^{\mathrm{fit}})\}$, to the corresponding input values $\{\mu_i\} = \{\mathrm{Re}(\mathcal{T}_a^{\mathrm{input}}),\ \mathrm{Im}(\mathcal{T}_a^{\mathrm{input}})\}$, weighted by the inverse of the covariance matrix (precision matrix), i.e.

$$\chi^2 = (y_1 - \mu_1, \dots, y_n - \mu_n) \begin{pmatrix} \sigma_1^2 & \dots & \mathrm{cov}(y_1, y_n) \\ \vdots & \ddots & \vdots \\ \mathrm{cov}(y_n, y_1) & \dots & \sigma_n^2 \end{pmatrix}^{-1} \begin{pmatrix} y_1 - \mu_1 \\ \vdots \\ y_n - \mu_n \end{pmatrix}. \tag{5.3}$$

Here $\mathrm{cov}(y_i, y_j)$ is the covariance of the parameters y_i and y_j, and $\mathrm{cov}(y_i, y_i) = \sigma_i^2$ is the variance of y_i.

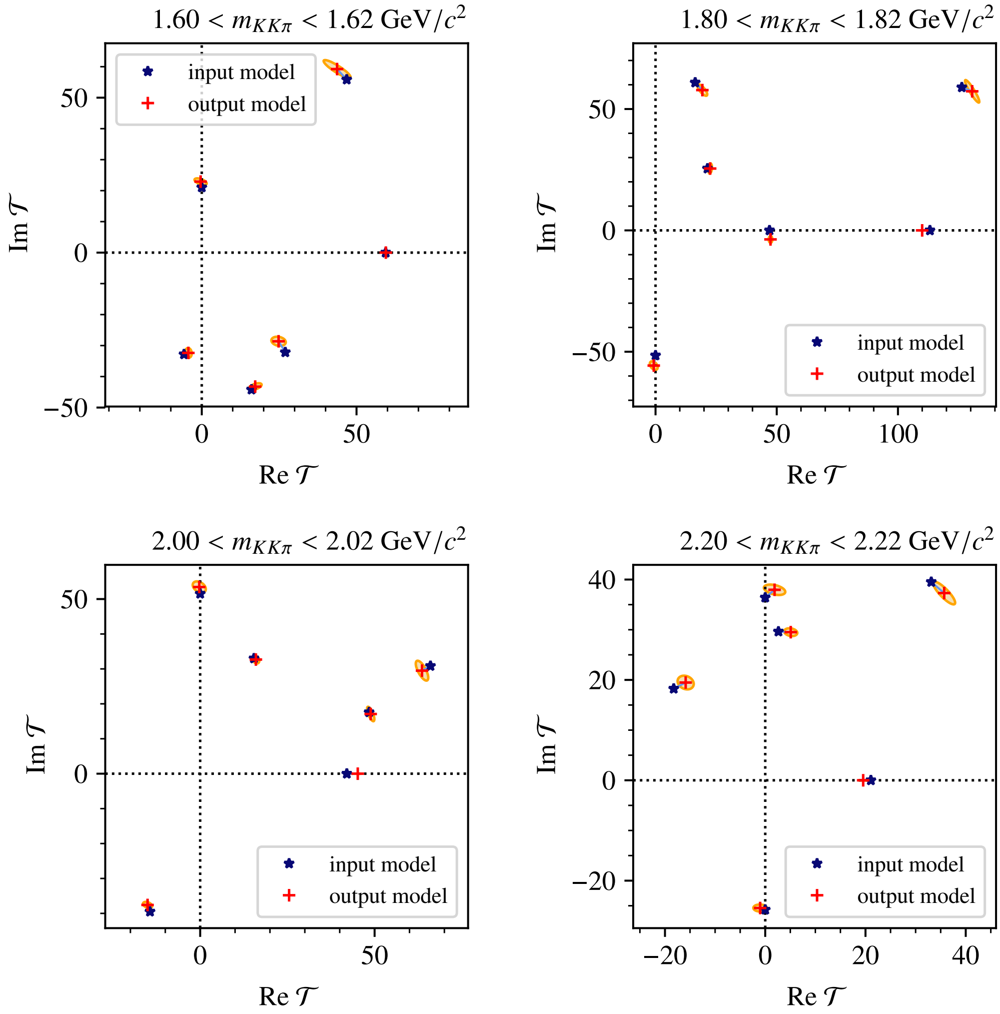

Figure 5.6: Results of the PWA fits of the MC pseudodata subsample of 108 000 events with perfect detector acceptance and the exact PWA waveset in four $m_{KK\pi}$ bins: The Argand plots show the transition amplitudes. The input amplitudes used to generate the MC pseudodata are shown in blue and the output amplitudes from the PWA fit in red, with the corresponding uncertainty ellipses in orange. Corresponding amplitudes are connected by light-blue lines.

Ideally, if the data are Gaussian distributed, the expectation value of χ^2 corresponds to the number of degrees of freedom, which is here equal to $2N-1$, where N corresponds to the number of transition amplitudes, i.e. the number of partial waves. One can define the *reduced* chi-square

$$\chi^2_{\text{red}} = \frac{\chi^2}{\text{n.d.f.}} \tag{5.4}$$

which has an expectation value of 1. The χ^2_{red} values for the fit results in Fig. 5.6 are shown in Fig. 5.9a. As can be seen, the χ^2_{red} values lie slightly above 1, except for the mass bin at $m_{KK\pi} = 1.81\ \text{GeV}/c^2$, which has a larger value of $\chi^2_{\text{red}} = 2.96$. This corresponds to a P-value of only 0.0006, which means that the discrepancies between the input transition amplitude values and the fit outcome in this mass bin are statistically significant.

5.2.2.2 Variation of the Number of Events

In order to further investigate these discrepancies, a PWA fit is performed using the entire MC dataset, i.e. 1.77×10^6 events. The results are shown in Fig. 5.7. The estimated transition amplitude values are close to those of the previous fit. Due to the considerably larger number of events used for the fit, the uncertainties of the transition amplitudes decrease significantly. However, the differences to the model values do not shrink with the uncertainties. This results in a significant increase of the reduced chi-square values of the fit as defined in Eqs. (5.3) and (5.4), which are shown in Fig. 5.9b. The χ^2_{red} values correspond to P-values smaller than 10^{-5} in all $m_{KK\pi}$ bins, indicating that the differences are unlikely to stem from fluctuations of the data, but rather come from a bias intrinsic to the model.

5.2.2.3 Fits with the Extended Waveset

We perform a third partial-wave decomposition with a waveset containing more partial waves than just the six waves used to generate the MC data. Here, a total of 49 waves with different X^- quantum numbers and isobar resonances are included (see Table A.1). As discussed above, this situation is more akin to fits of real data. Again, the subset of MC pseudodata with 108 000 events is used. The results of those fits in four mass bins are shown in Fig. 5.8. Except for the mass bin at $1.61\ \text{GeV}/c^2$, the results looks similar to those in Fig. 5.6: The fit results and the input values are in good agreement, although some minor differences in the amplitudes of the six waves used as input model are still present. The intensities of most of the 42 partial waves that are not

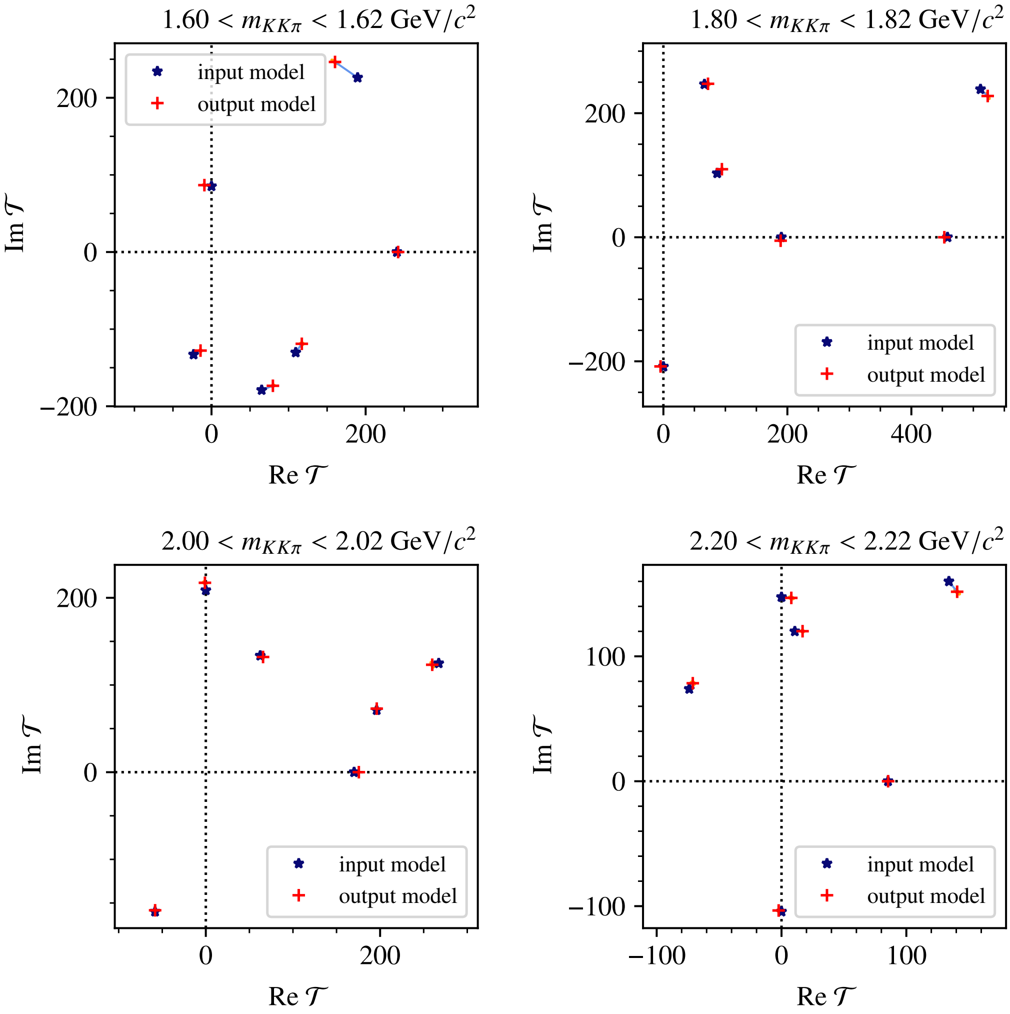

Figure 5.7: Results of the PWA fits of the complete set of MC pseudodata with 1.77×10^6 events with perfect detector acceptance and the exact PWA waveset in four $m_{KK\pi}$ bins: The Argand plots show the transition amplitudes. The input amplitudes used to generate the MC pseudodata are shown in blue and the output amplitudes from the PWA fit in red, with the corresponding uncertainty ellipses in orange. Corresponding amplitudes are connected by light-blue lines.

present in the MC data are consistent with zero within their uncertainties, i.e. their amplitudes are clustered around the origin. This is a good sign, as there does not seem to be any significant redistribution of intensity into non-input waves. The only notable difference from zero is the rather high intensity of the flat wave (located on the real axis) for $m_{KK\pi} = 1.81\ \mathrm{GeV}/c^2$, although the amplitude of this wave has a quite large uncertainty. The behavior of the fit is different in the low-mass bin at $1.61\ \mathrm{GeV}/c^2$. Here, larger discrepancies between the fitted amplitudes and the model input appear. Although most non-input waves are still in good agreement with zero, some deviate further away from the origin than is the case in the higher mass bins. Especially the flat wave has a large, non-zero amplitude. The uncertainties of some partial wave amplitudes also are significantly larger than in the other fits.

The χ^2_{red} values in the four mass bins are shown in Fig. 5.9c. Here, two sets of values are shown. First, one can compute the χ^2_{red} statistic taking into account the amplitudes of the entire waveset of the fit, as an estimator of the fit quality in general. Those values are consistent with the deviations discussed above. The higher χ^2_{red} value of about 2.2 at $1.6\ \mathrm{GeV}/c^2$ underlines the worsening of the fit in this mass bin. In the $1.81\ \mathrm{GeV}/c^2$ mass bin, the main contribution to the χ^2_{red} value of about 2.0 comes from the non-zero flat-wave intensity. In the two higher-mass bins, the chi-square χ^2_{red} value is close to 1, which is partly also due to the additional free parameters from the 42 non-input waves. In order to investigate the effect of the additional waves on the estimation of the transition amplitudes with which the MC data were generated, χ^2_{red} values are calculated considering only the differences and covariances of the amplitudes of the six input waves. One can see that the χ^2_{red} values computed in this way are in two of the four mass bins noticeably higher than the values taking into account all waves. However, those χ^2_{red} values are close to the values from the first PWA fit with a perfect waveset (see Section 5.2.2.1 and cf. Fig. 5.9a). It thus seems that the addition of waves into the waveset does not significantly alter the estimates of the partial-wave amplitudes of the waves that are actually contained in the data.

5.2.2.4 Conclusions

Overall, the PWA fits of the MC pseudodata seem to be able to estimate the values of the partial-wave transition amplitudes quite accurately in the case of perfect acceptance. Some small differences with respect to the input values, however, remain, and cannot be explained by the fluctuations of the data. In the case of an extended PWA fit waveset, we observe some changes of the amplitudes at lower masses especially for the flat wave, and some amplitudes

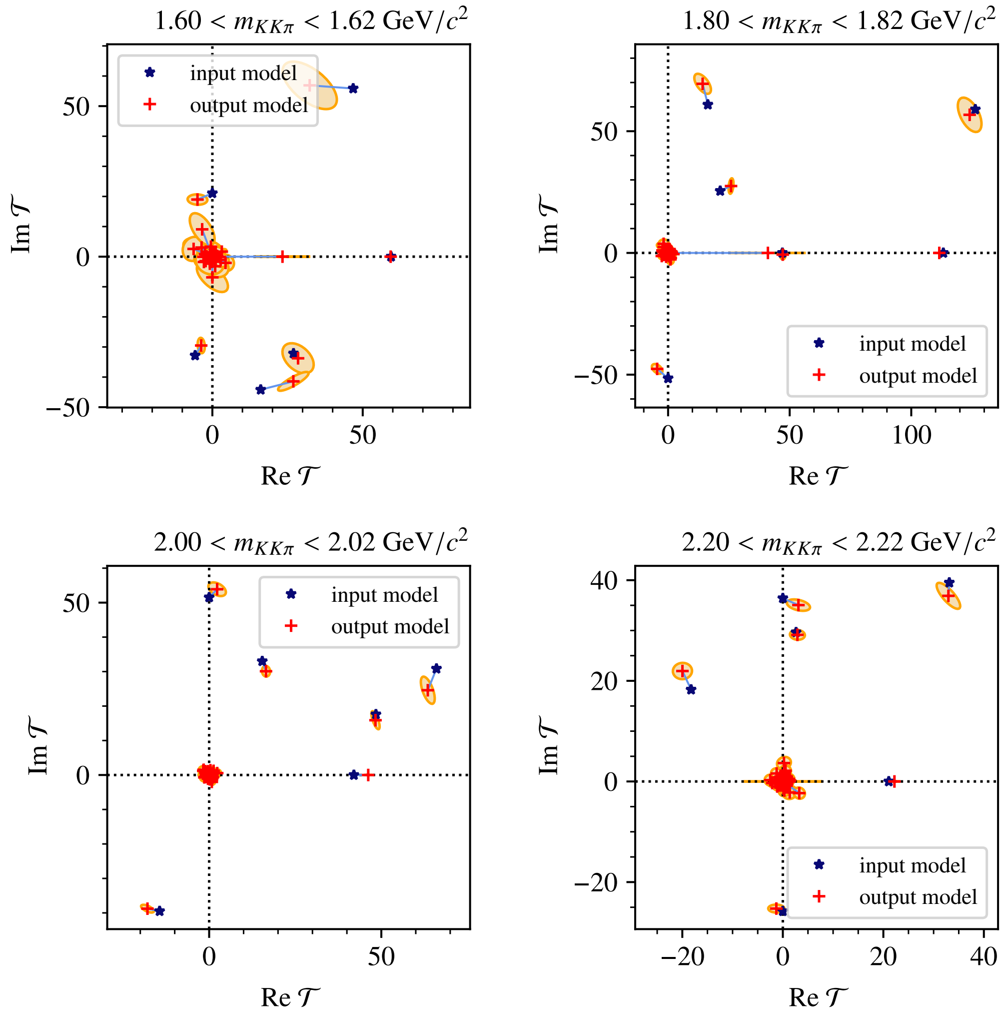

Figure 5.8: Results of the PWA fits of the MC pseudodata subsample with 108 000 events with perfect detector acceptance and an extended PWA waveset in four $m_{KK\pi}$ bins: The Argand plots show the transition amplitudes. The input amplitudes used to generate the MC pseudodata are shown in blue and the output amplitudes from the PWA fit in red, with the corresponding uncertainty ellipses in orange. Corresponding amplitudes are connected by light-blue lines.

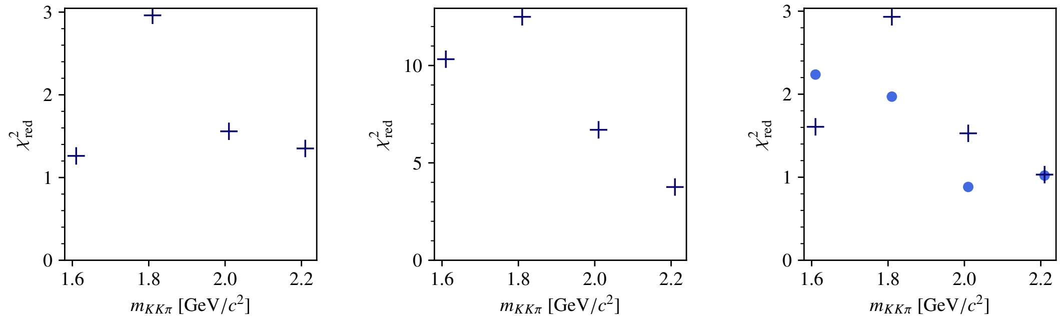

(a) χ^2_{red} of fit shown in Fig. 5.6.

(b) χ^2_{red} of fit shown in Fig. 5.7.

(c) χ^2_{red} of fit shown in Fig. 5.8.

Figure 5.9: Reduced chi-square values χ^2_{red} of the PWA fits of pseudodata presented in Section 5.2.2. For the fit with an extended waveset (c), the χ^2_{red} values calculated with only the six input waves are indicated by dark-blue crosses and those taking into account all waves by light-blue dots.

seem to be less clearly determined. This hints to the fact that the fit has trouble distinguishing some partial waves even with perfect acceptance, which is consistent with the observations from the phase-space integral matrix in Section 5.1.4. The waves with the largest moduli of the integral matrix elements are mostly waves with KK and $K\pi$ S-wave isobars. Five of the six waves used to generate the MC pseudodata are of this kind. According to the VES analysis, the waves with KK and $K\pi$ S-wave isobars, especially the $0^-0^+[KK]_S\pi S$ and $0^-0^+[K\pi]_S KS$ waves, contain most of the intensity also in the real data. Since they all have $J_\xi = 0$, there is no angular dependence in the decay of the isobar (usually described by the angles ϑ_{HF} and ϕ_{HF}; see Section 3.2.5). This can already lead to distinguishability issues. For waves that in addition have no angular momentum between the isobar and the bachelor particle, such as the $0^-0^+[KK]_S\pi S$ or the $0^-0^+[K\pi]_S KS$ wave, there is also no angular dependence in the X^- decay (usually described by the angles ϑ_{GJ} and ϕ_{GJ}; see Section 3.2.5). This means that, for those waves, the only difference lies in the distribution of the phase-space variable m_ξ. As mentioned in Section 3.2.4, the scalar isobar resonances are often very broad and hence difficult to resolve. Consequently, waves with KK and $K\pi$ S-wave isobars are parameterized by broad distributions in the subsystem mass m_ξ, rendering the waves even harder to distinguish by the fit.

However, in the case of perfect acceptance, the fit results still are in good agreement with the expected outcomes. The discrepancies observed in the two studies are minor, and while they could be caused by the above-mentioned problems, they cannot explain the much larger issues encountered in the real-data fits in their entirety. The behavior of the real-data fits thus does not seem to stem from these inherent problems with the partial-wave analysis model, but must rather come from a different source. A likely candidate are effects from the detector acceptance, which will be discussed in the following Sections 5.2.3 and 5.2.4.

5.2.3 Detector Acceptance

In this section, we discuss the main causes of acceptance loss in the $K^-K^+\pi^-$ channel. Here, the concept of acceptance, already briefly discussed in Section 3.3.4, includes the individual acceptances and efficiencies of each detector as well as the acceptance of the event reconstruction and selection process. The overall acceptance is low, and - more importantly - depends significantly on the kinematics of the $K^-K^+\pi^-$ final-state particles (see e.g. Fig. 4.2). The reasons for this will be investigated in more detail.

5.2.3.1 RICH Particle Identification and Momentum Distributions

The most significant contribution to the low acceptance of the experiment comes from the final-state particle identification by the RICH-1 detector, which has been discussed in Sections 2.2 and 4.1.2. It has already been mentioned there that the RICH-1 detector can efficiently separate π^- and K^- only at low particle momenta $|\vec{p}| \lesssim 45$ GeV/c. However, the momenta of the final-state particles have to add up to the total beam momentum of 190 GeV/c. As a consequence, even if not all final-state particles, but only certain combinations are identified, many $K^-K^+\pi^-$ events are rejected because these combinations of particles are not in the right momentum ranges. This causes "holes" in the momentum distributions of the final-state particles, as shown in Figs. 5.10a and 5.10b. The distribution of the K^- momentum peaks at about 45 GeV/c, then falls rapidly towards higher momenta. In this region, the K^- is identified. Between about 60 GeV/c and 100 GeV/c, no events can be detected. For $|\vec{p}_{K^-}| > 100$ GeV/c, the total momentum of the π^-K^+ pair is lower than 90 GeV/c, which means that the two particles can in some cases be identified. This causes the increase of events at high $|\vec{p}_{K^-}|$. The momentum distribution of the π^- shows a slightly different structure: at low $|\vec{p}_{\pi^-}| < 50$ GeV/c, the π^- and K^+ can be identified if the latter particle is also in the right momentum range. Alternatively, for some events, the K^- can be identified, which would mean that the K^+ has a high momentum outside the RICH acceptance. At high $|\vec{p}_{\pi^-}| > 50$ GeV/c, the only events that can contribute are those where the K^- has low momentum and can thus be identified.

These observations are summarized in the two-dimensional distribution of $|\vec{p}_{\pi^-}|$ vs. $|\vec{p}_{K^-}|$ in Fig. 5.10c. The one-dimensional distribution of either $|\vec{p}_{K^-}|$ or $|\vec{p}_{\pi^-}|$ in Fig. 5.10a and Fig. 5.10b, respectively, are obtained by integrating over the momentum of the other particle, respectively. For perfect acceptance, one would expect the two-dimensional histogram to be filled approximately evenly by a triangular shape given by momentum conservation, i.e. $|\vec{p}_{\pi^-}| + |\vec{p}_{K^-}| + |\vec{p}_{K^+}| = 190$ GeV/c. However, in the measured distribution, two approximately triangle-shaped empty sections can be distinguished, where no events are detected. The upper one is located at $|\vec{p}_{\pi^-}| > 60$ GeV/c and $|\vec{p}_{K^-}| > 60$ GeV/c, where none of the two particles π^-, K^- can be identified. The lower triangular "hole" in the distribution at $|\vec{p}_{\pi^-}| < 60$ GeV/c and $|\vec{p}_{K^-}| > 60$ GeV/c comes from the fact that if the K^- cannot be identified, then both remaining particles π^- and K^+ must be identified, and identifying one of the two would be insufficient.

5.2.3.2 Angular Acceptance

The “holes” in the momentum distributions discussed in the previous section translate into similar “holes” in the angular distribution of the acceptance, i.e. regions in the phase-space variables θ_{GJ}, ϕ_{GJ}, θ_{HF}, and ϕ_{HF}, in which the acceptance is close to zero. This means only few events can be detected in those phase-space regions. Such regions are especially pronounced in the distribution of the acceptance in θ_{GJ} and ϕ_{GJ} as shown in Fig. 5.11. These two angles describe the decay of the X^-, in this specific case into a $K^+\pi^-$ isobar and a bachelor K^-. One can clearly see that the acceptance has a strong dependence on both phase-space variables. There is a large area in which the acceptance is close to zero, and regions with higher acceptance only exist at certain angles. This can be explained by the following reasoning: at $\cos\theta_{\mathrm{GJ}}$ close to $+1$, the $K^+\pi^-$ system is emitted in forward beam direction, and thus has a higher momentum in the lab frame. In the rest frame of X^-, the bachelor K^- is emitted in opposite direction to $K^+\pi^-$ and is thus slower in the lab frame, which means it has a higher probability of being identified by the RICH detector. For $\cos\theta_{\mathrm{GJ}}$ close to -1, the opposite happens: the $K^+\pi^-$ system is slower and can in some cases be identified by the RICH detector, which is why the acceptance there increases slightly. In the large $\cos\theta_{\mathrm{GJ}}$ region in between those extremes however, no particle has the right momentum to be identified, and hence no events are registered. Similar dependence of the acceptance is observed in the distribution of θ_{GJ} and ϕ_{GJ} in the case of a K^+K^-

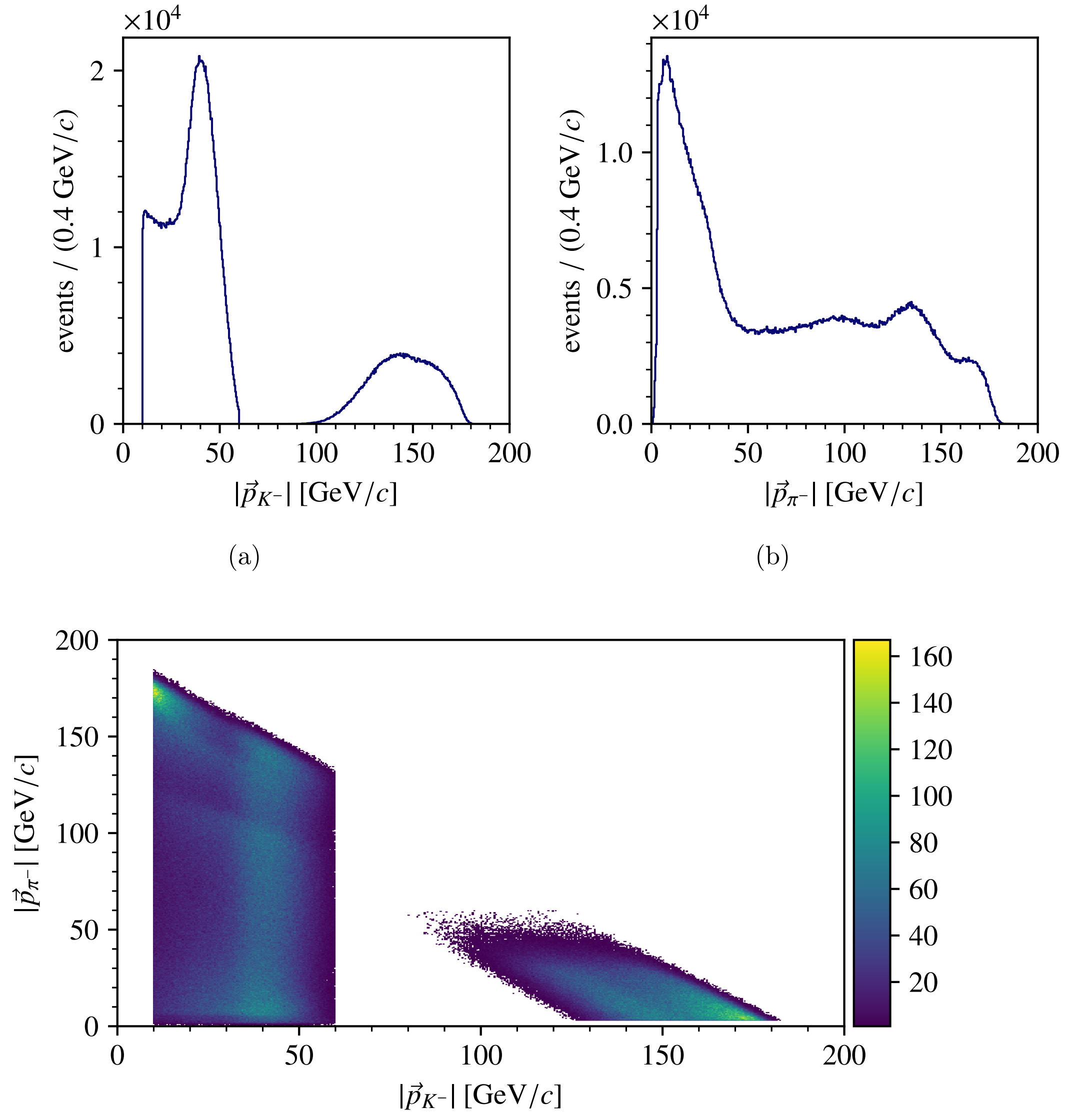

(a)

(b)

(c)

Figure 5.10: Momentum distributions of the real data. (a) Distribution of $|\vec{p}_{K^-}|$. (b) Distribution of $|\vec{p}_{\pi^-}|$. (c) Two-dimensional distribution of $|\vec{p}_{\pi^-}|$ and $|\vec{p}_{K^-}|$.

isobar and in the distributions of θ_{HF} and ϕ_{HF}. They are plotted in Figs. A.2 and A.3.

The zero-acceptance regions in the phase-space can significantly alter the distinguishability of certain waves. The fit cannot distinguish between the angular distributions of two waves if those angular distributions differ predominantly in the regions where there is no acceptance and thus no data. As the concerned regions are rather large, many waves are potentially affected. This is consistent with the accepted integral matrices in Fig. 5.3, where many waves have matrix elements with large moduli, and thus are potentially difficult to distinguish.

However, the acceptance seems to improve towards higher $m_{KK\pi}$ values. Comparing the upper and lower plot in Fig. 5.11, which correspond to the 1.8 GeV/c^2 and 2.2 GeV/c^2 region respectively, one can see that the overall acceptance increases, but also that the area of the zero-acceptance region becomes slightly smaller. Yet, it still remains rather large at higher masses.

In order to study the effect of the angular dependence of the acceptance on the partial-wave decomposition, fits of MC pseudodata that are weighted by the detector acceptance are performed in the next Section 5.2.4.

5.2.4 Pseudodata Fits with Realistic Acceptance

We investigate the effects of the detector acceptance, discussed in Section 5.2.3, on the PWA fit result by using the MC pseudodata sample that was processed through detector simulation, reconstruction and event selection (see Section 5.2.1). This sample contains 108 000 events. Two PWA fits are performed on these data, one including only the set of six waves that are contained in the MC data and a second one including additional waves.

5.2.4.1 Fits with the Exact Waveset

To summarize the result of the PWA with the six waves contained in the data, Fig. 5.12 shows the estimated transition amplitude in the complex plane and the corresponding input values, i.e. the values used to generate the MC pseudodata. We observe significant differences between the results of the PWA fits presented here and those of the MC dataset with perfect acceptance presented in Section 5.2.2. As the behavior of the PWA fits differs greatly between the four mass bins, they will be discussed separately. The fit in the mass bin at 1.8 GeV/c^2 is not able to reproduce the input values for the transition amplitudes at all. All amplitudes exhibit significant differences w.r.t. the input

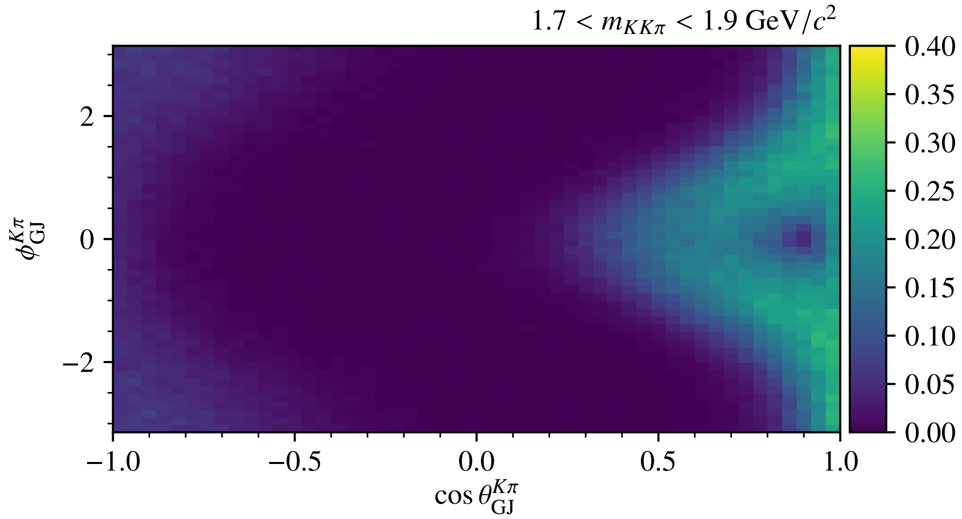

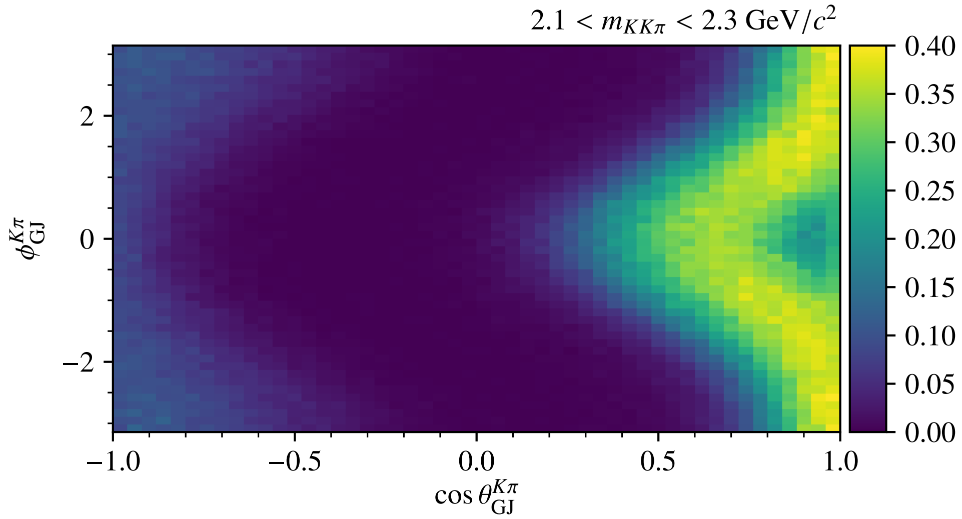

Figure 5.11: Dependence of the acceptance on the phase-space variables ϕ_{GJ} and $\cos\theta_{\mathrm{GJ}}$ that describe the decay of X^- into a $K^+\pi^-$ isobar and a bachelor K^-. (Top) Acceptance in the 1.8 GeV/c^2 mass region. (Bottom) Acceptance in the 2.2 GeV/c^2 mass region.

value. The differences appear mostly in the phase of the amplitudes: All amplitudes have shifted phases, except the one that serves as reference and hence has a fixed phase of 0°. Many waves also have a significantly different intensity. The fit result thus is unreliable in this mass range. Going to the lower-mass bin at 1.6 GeV/c^2, the deviations become even worse. There, basically any similarity between the input amplitudes and the fit output is lost. However, at higher masses, in the 2.0 GeV/c^2 and 2.2 GeV/c^2 mass bins, the situation seems to gradually improve. While there are still significant differences for a few waves, the input and output amplitudes become close for most of the other waves. The behavior of the PWA fits at higher masses is more similar to the one with perfect acceptance (see Fig. 5.6). It seems that although the loss of acceptance discussed in Section 5.2.3 is still significant at higher masses, it has a considerably smaller effect on the PWA fit than at lower masses.

The $m_{KK\pi}$ dependence of the reliability of the PWA fits is illustrated further in Fig. 5.13, which shows the partial-wave intensities of three selected waves, and in Fig. 5.16a, which shows the chi-square values of the fits. At low masses, the large differences of the partial-wave amplitudes translate into extremely high χ^2_{red} values. At 2.0 GeV/c^2 and 2.2 GeV/c^2, however, the fit finds more accurate partial-wave intensities, and the smaller differences between fit result and model translate into χ^2_{red} values much closer to 1.

5.2.4.2 Fits with the Extended Waveset

Similar to the approach in Section 5.2.2.3, we perform a second PWA fit with the same MC dataset but using a larger PWA waveset consisting of 49 waves (see Table A.1). The Argand plots of the resulting transition amplitudes and the input values are shown in Fig. 5.14. As expected, the additional waves in the PWA model disturb the fit in every mass bin. As in the previous fit in Section 5.2.4.1, the effects are most drastic in the 1.6 GeV/c^2 mass bin, where many non-model waves are found with significant intensities. The estimated transition amplitudes bear no resemblance with the input values. At 1.8 GeV/c^2, some non-model waves, especially the flat wave, have non-zero intensities, and there are considerable differences between the input values and the fit estimates. At higher masses, most non-model waves, except notably the flat wave, are compatible with zero intensity.

For the six input waves, we observe larger discrepancies between the input values and the fit estimates than in the fit with exact waveset (cf. Fig. 5.12). Overall, the reliability of the PWA fits thus becomes even worse when adding waves to the PWA model that are not present in the data. Unfortunately, this situation is more akin to the real-data case, as discussed in Section 5.2.2.

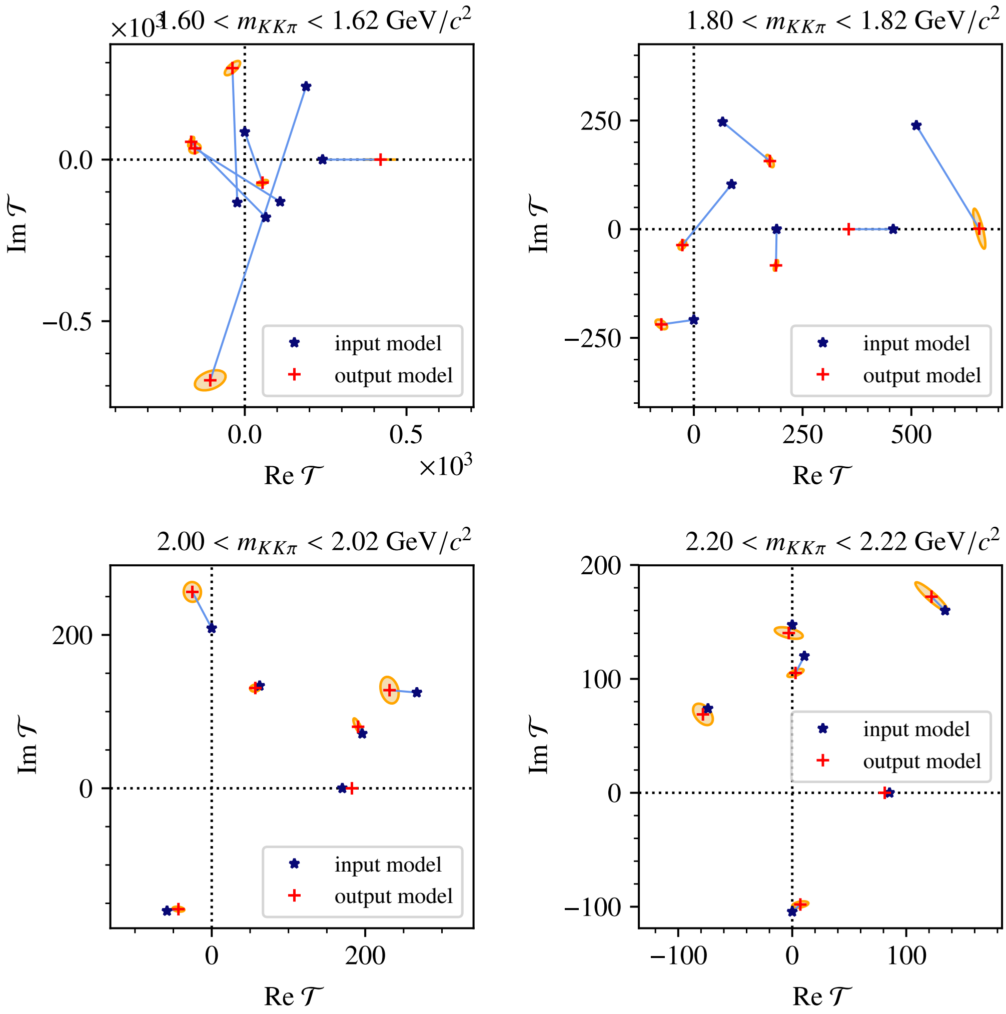

Figure 5.12: Results of the PWA fits of the MC pseudodata with realistic detector acceptance and the exact PWA waveset in four $m_{KK\pi}$ bins: The Argand plots show the transition amplitudes. The input amplitudes used to generate the MC pseudodata are shown in blue and the output amplitudes from the PWA fit in red, with the corresponding uncertainty ellipses in orange. Corresponding amplitudes are connected by light-blue lines.

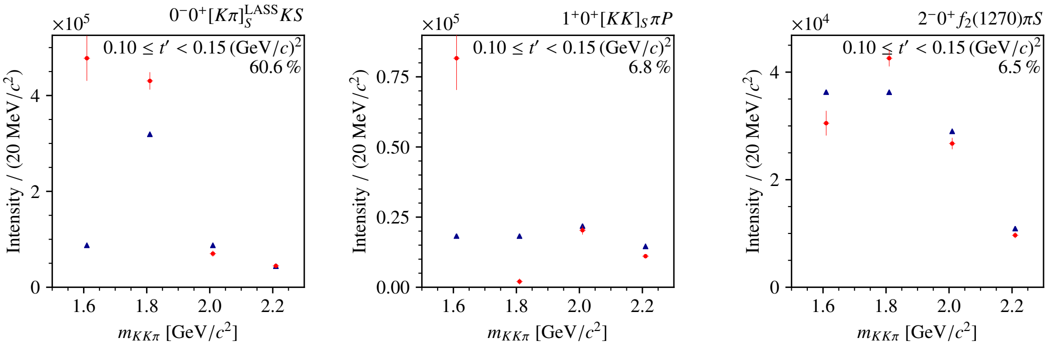

Figure 5.13: Intensities of three selected partial waves from the pseudodata fits with realistic detector acceptance and the exact PWA waveset in four mass bins. The input model intensities are shown in blue and the intensities estimated by the fit in red.

Fig. 5.15 shows the intensities of three selected partial waves, comparing input values and fit results in the four mass bins. One can see significant differences between fit and input especially for the two lower-mass bins. The χ^2_{red} values, shown in Fig. 5.16b, are calculated again taking into account all waves, and taking only into account the six waves with which the MC pseudodata were generated. The values are overall high in the first three mass bins, then drop down to a few units in the last bin. Comparing the χ^2_{red} values that take into account only the six model waves (dark blue crosses in Fig. 5.16b) with Fig. 5.16a, which shows the corresponding values for the fit with the perfect PWA model, we see that the values for the two lower-mass bins are reduced. This is because the PWA fit result for the larger waveset has much larger uncertainties. At 2.0 GeV/c^2, the χ^2_{red} value is much larger for the PWA fit with the extended waveset. This indicates that the fit in this bin has more difficulties in correctly finding the amplitude values in the presence of additional waves.

5.2.4.3 Conclusions

Including the effects of acceptance into the MC pseudodata alters the PWA fit significantly, compared to the previous studies without acceptance (see Section 5.2.2). Overall, the reliability of the PWA fit seems to suffer a lot when performed on the accepted MC dataset. Drastic differences in the PWA fit behavior can be observed between the various mass bins. At low masses, below 2.0 GeV/c^2, the fit fails to estimate the values of the transition amplitudes cor-

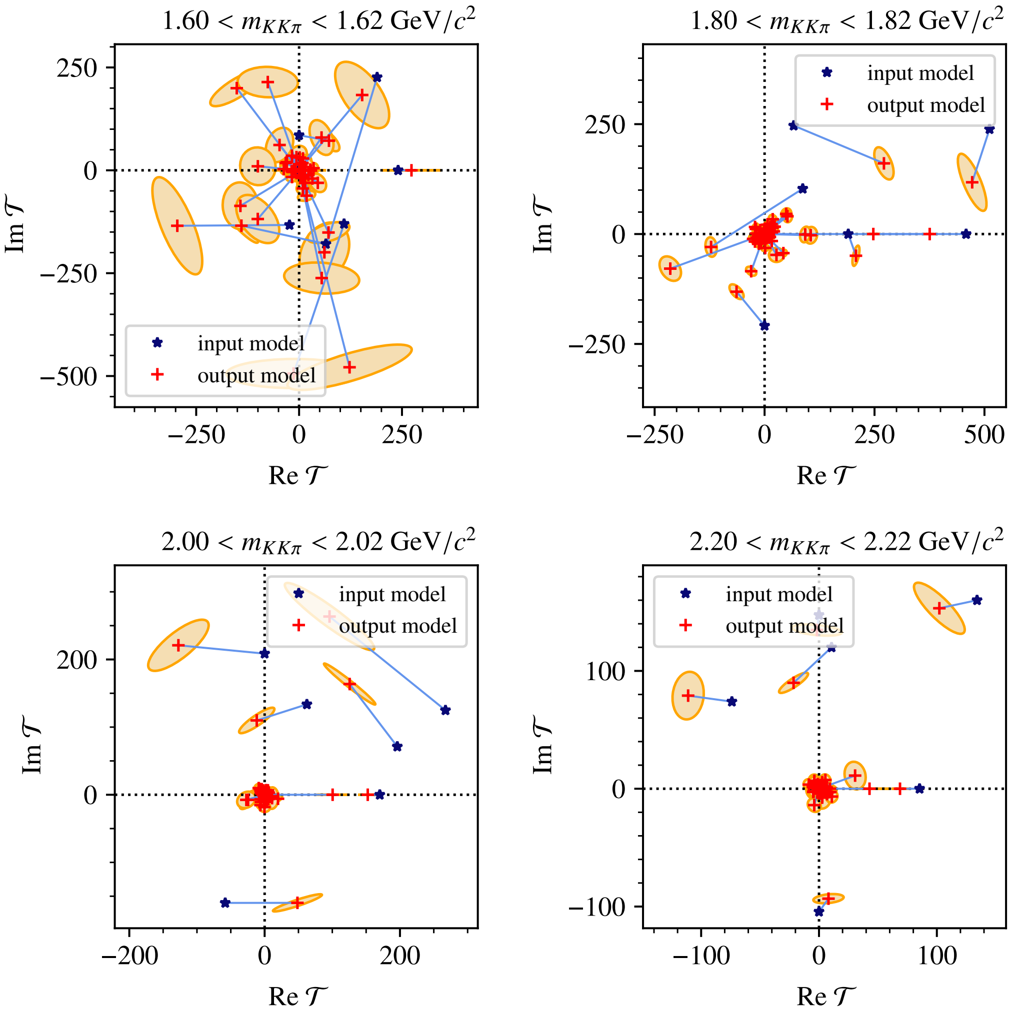

Figure 5.14: Results of the PWA fits of the MC pseudodata with realistic detector acceptance and an extended PWA waveset in four $m_{KK\pi}$ bins: The Argand plots show the transition amplitudes. The input amplitudes used to generate the MC pseudodata are shown in blue and the output amplitudes from the PWA fit in red, with the corresponding uncertainty ellipses in orange. Corresponding amplitudes are connected by light-blue lines.

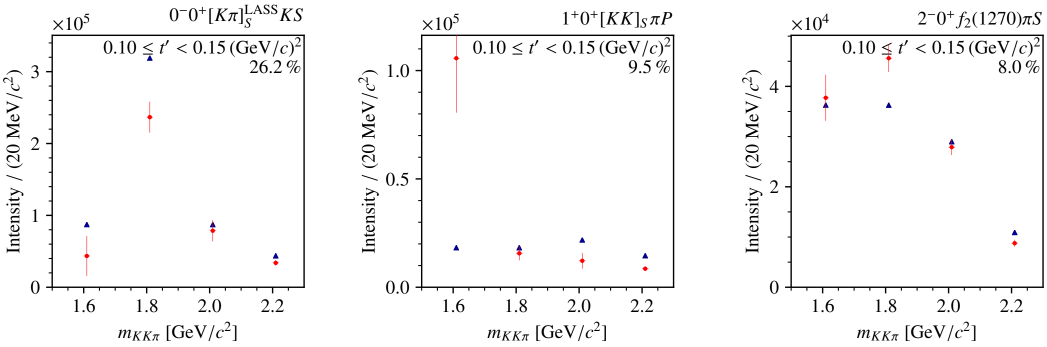

Figure 5.15: Intensities of three selected partial waves from the pseudodata fits with realistic detector acceptance and an extended PWA waveset in four mass bins. The input model intensities are shown in blue and the estimates by the fit intensities in red.

rectly, and the results of the fit are not compatible with the values with which the MC pseudodata were generated. At higher masses, above ca. 2.0 GeV/c^2, there is a better agreement between the fit results and the expectations. However, when adding more waves to the PWA fit model, the fit worsens also at high masses. The appearance of a high flat-wave intensity at all masses is especially notable.

It is important to note that the MC pseudodata studies are still idealized in certain aspects, so that a direct quantitative comparison to real-data fits is not possible. Firstly, for real data, the exact waveset is unknown. As seen in Section 5.2.4.2, when the PWA waveset is too large, the fit deteriorates further even at masses above 2 GeV/c^2. One also has to take into account the possibility that the real-data analysis waveset is too small and thus lacks important waves, or contains the wrong waves. Secondly, the acceptance for the generation of pseudodata is obtained via a simulation of the detector setup, which might not be perfectly accurate. The same detector model is used in the PWA fit to weight the model, as described in Section 3.3.4. This means that for fits to MC data, the acceptance correction is perfect, which is not the case for real data. Additional discrepancies between model and data arise from the parametrizations of the isobar amplitudes used in the PWA model, which might deviate from the data, as well as the parametrization of non-resonant contributions.

The fits performed on the MC pseudodata still give us hints on the reliability of the real-data fit. The results with pseudodata exhibit similarities to the (presumed) issues encountered in the real-data fit, such as the substantial

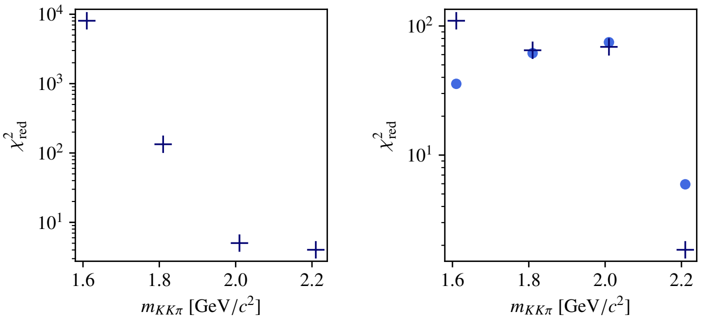

(a) χ^2_{red} of fit shown in Fig. 5.12.

(b) χ^2_{red} of fit shown in Fig. 5.14.

Figure 5.16: Reduced chi-square values χ^2_{red} of the PWA fits of pseudodata presented in Section 5.2.4 (note the logarithmic scale). For the fit with an extended waveset (b), the χ^2_{red} values calculated with only the six input waves are indicated by dark-blue crosses and those taking into account all waves by light-blue dots.

redistribution of intensity across the waves and the high flat-wave intensity. One can therefore conclude that the limited acceptance is almost certainly the primary source of the problems encountered in the real-data fit. Unfortunately, this can neither be improved nor corrected in the data. According to our studies, the fit is expected to be especially unreliable at low masses. The mass region between 1.5 and 2.0 GeV/c^2 in the real data is quite crucial for the identification of well-known resonances such as the $\pi_2(1670)$, the $\pi(1800)$ and the $\pi_2(1880)$, which could be used to cross-check the results with other analyses. Beyond 2.0 GeV/c^2, the PWA fit seems to become more reliable. Unfortunately, at such high masses, results from other experiments are scarce and cannot be used to validate our fit. Any results in the real data would be ambiguous at best without confirmation of the validity of the fit by e.g. the identification of other well-known resonances, which is rendered impossible by the low acceptance in the mass region around such resonances.

As explained in Section 5.2.3, the major part of the acceptance loss comes from the required identification of the final-state particles to separate $K^-K^+\pi^-$ from $\pi^-\pi^-\pi^+$, and the only possibility of significantly improving this would be to add additional particle-identification detectors to the COMPASS setup. However, one factor that can possibly be improved is the selection of which partial waves are included into the PWA model. The so-called waveset selection will be discussed and applied in Section 5.3 on real and pseudodata.

5.3 Waveset Selection

As its name indicates, the waveset selection is a process that selects, out of a large pool of waves, those partial waves that contribute most significantly to the data. In this section, we will briefly outline the method of waveset selection, discuss the construction of the pool from which the waves are selected, and finally present the results of the selection performed on the sets of MC pseudodata and real data that were introduced in Sections 5.1 and 5.2, respectively. More information on the waveset selection method can be found in Refs. [11, 12, 16].

5.3.1 Motivation and Methods

In principle, the partial-wave analysis model allows for an infinite number of partial waves to contribute in the sum in Eq. (3.17). However, not all waves contribute significantly to the intensity. With only a limited dataset and finite computational resources, including an infinite number of partial waves is evidently impossible. Thus, a certain set of waves, which we include into the PWA model, needs to be selected carefully. As was already briefly discussed in Section 5.2.4.3, the choice of the waves to include constitutes a non-trivial model-selection problem. Using a too large waveset may lead to overfitting, where the PWA model starts describing fluctuations of the data. Using a too small waveset could lead to missing interesting signals in the left-out waves. It may also leave structures in the data stemming from these missing waves undescribed. The resulting tension between the data and the model may cause artificial structures in the extracted amplitudes of the selected waves.

Traditionally, PWA wavesets are constructed by hand, i.e. by iteratively adding and removing waves based on certain criteria, one of which could be e.g. whether the wave that has been added has significant intensity and/or structure.[5] Such a manual selection is problematic, as it may introduce an observer bias to the waveset and is only based on subjective selection criteria and hence difficult to reproduce. The relative fit quality of two wavesets can be inferred in certain cases by their likelihood ratio, as the latter is χ^2-distributed for *nested models* only. However, no absolute goodness-of-fit criterion exists, and, in the case of the PWA, interference makes it impossible to build nested models. Certain waves correlate (meaning their individual inclusion into the model only marginally improves the fit, but the inclusion of the subset of waves improves it significantly), rendering a step-by-step construction of the model

---

[5] Such a manual waveset construction was also tried for $K^-K^+\pi^-$, it is described in Appendix A.1

waveset very difficult: all combinations of waves would have to be tested, which is impossible by hand.

Because of these problems, techniques have been developed to construct an optimally-sized waveset from data with the least subjectivity as possible. These techniques have a common approach: First, one assembles a large set of waves containing all waves that potentially contribute to the data: this is called the *wavepool*. Its construction is discussed in Section 5.3.2. Then, a waveset selection fit is performed using all waves in the wavepool. In order to circumvent overfitting, which would be inevitable with a large waveset, additional regularization techniques must be employed in the fit procedure. To this end, a so-called *regularization*, or *penalty term* $\ln \mathcal{L}^a_{\text{reg}}$, is added to the the log-likelihood function in Eq. (3.24) for each wave a. These additional terms impose a penalty on the likelihood which **grows with the partial-wave intensities** $|\mathcal{T}_a|^2$. That way, the intensity of waves that are only weakly supported by the data is suppressed by the model, thereby deselecting them. There are different choices for the penalty term; here, the so-called Cauchy regularization is used:

$$\ln \mathcal{L}^a_{\text{reg}}(\mathcal{T}_a; \Gamma_a) = -\ln \left[1 + \frac{|\mathcal{T}_a|^2}{\Gamma_a^2} \right] \,. \tag{5.5}$$

Its shape in the plane of a transition amplitude $\mathcal{T}_a$ is shown in Fig. 5.17. The maximum of $\ln \mathcal{L}^a_{\text{reg}}$ at $\mathcal{T}_a = 0$ favors low intensities for insignificant waves. The free parameters Γ_a in the penalty terms set the strength of the regularization. The same values Γ_a are used as in Refs. [11, 12].

Introducing the penalty term can lead to multimodality in the log-likelihood function, i.e. the appearance of local minima in addition to the global minimum of the function. In order to circumvent this issue, multiple fit attempts with randomly chosen start values are performed for each waveset-selection fit (in our case, we perform 150 fit attempts). The fit attempt considered 'best' is the one with the highest log-likelihood value. Ideally, most fit attempts find similar solutions, in which case the multimodality is uncritical.

Waves that show significant intensity in the regularized fit are added to the PWA waveset and a refit without the regularization terms is performed with the selected waveset.[6] This method has been successfully used to determine wavesets as a function of m_X and t' for both the $\pi^-\pi^-\pi^+$ and $K^-\pi^-\pi^+$ final states [11, 12, 16].

---

[6] This is done because the penalty term imposes a bias especially on waves with small intensity. The results with and without penalty term should be quite similar in higher-intensity waves.

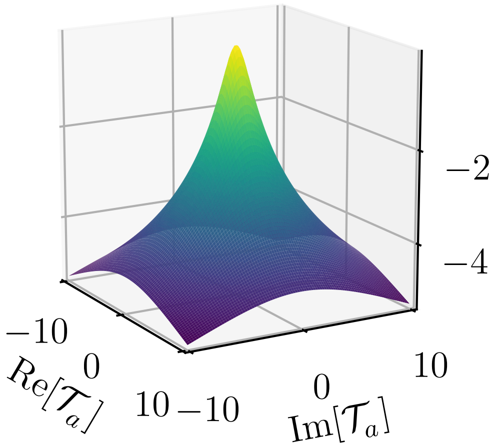

Figure 5.17: Cauchy regularization term $\ln \mathcal{L}^a_{\text{reg}}$ in the complex plane of a transition amplitude $\mathcal{T}_a$. From Refs. [11, 12].

5.3.2 Construction of the Wavepool

In order to perform a waveset selection, we first have to construct a pool of waves as large as possible, i.e. containing all waves that could contribute significantly to the data while imposing as few limitations as possible. We restrict the total spin of X^- to $J \leq 6$, the corresponding spin projection to $M = 0,\ 1$ and only allow waves with positive reflectivity (see Section 3.3.3). Also, we have to choose which isobar resonances appear in the decays. We include isobar resonances with masses up to 2 GeV/c^2 that have been observed decaying into K^+K^- or $K^+\pi^-$. This results in 15 resonances for the K^+K^- subsystem and 7 resonances for the $K^+\pi^-$ subsystem, which are listed together with their main properties in Table 5.2. This selection, which is kept as broad as possible, results in a wavepool containing 673 waves. The aim of the waveset selection is now to select those waves out of the wavepool that contribute most to the data. This is presented in the following sections.

5.3.3 Waveset Selection on Pseudodata

In this section, we perform the waveset selection on the sets of Monte Carlo pseudodata described in Section 5.2.1. Similarly to the studies on pseudodata discussed in Section 5.2, this enables us to verify the reliability of the waveset-

Table 5.2: Isobar resonances included in the PWA wavepool used for the waveset selection, as well as values of their masses and widths used in the analysis. The isobar S-waves cannot be modeled by simple Breit-Wigner resonances (see Section 3.2.4), their Breit-Wigner masses and widths are thus omitted.

	resonance	J^{PC}	mass [MeV/c^2]	width [MeV/c^2]
KK	$f_0(500)$ or σ	0^{++}	K^+K^- S-wave	
	$f_0(980)$	0^{++}	990	70
	$\phi(1020)$	1^{--}	1019.461	4.266
	$f_2(1270)$	2^{++}	1275.5	186.7
	$f_0(1370)$	0^{++}	1350	350
	$f_2(1430)$	2^{++}	1430	40
	$\rho(1450)$	1^{--}	1465	400
	$f_0(1500)$	0^{++}	1504	109
	$f_2'(1525)$	2^{++}	1525	73
	$f_2(1565)$	2^{++}	1562	134
	$\rho_3(1690)$	3^{--}	1688.8	161
	$\rho(1700)$	1^{--}	1720	250
	$f_0(1710)$	0^{++}	1723	139
	$f_2(1950)$	2^{++}	1944	472
	$f_2(2010)$	2^{++}	2011	202
$K\pi$	$K_0^*(700)$ or κ	0^{+}	$K^+\pi^-$ S-wave	
	$K^*(892)$	1^{-}	895.81	47.4
	$K_0^*(1430)$	0^{+}	$K^+\pi^-$ S-wave	
	$K_2^*(1430)$	2^{+}	1432.4	109
	$K^*(1680)$	1^{-}	1717	322
	$K_3^*(1780)$	3^{-}	1776	159
	$K_0^*(1950)$	0^{+}	$K^+\pi^-$ S-wave	

selection procedure for the $K^-K^+\pi^-$ channel because the partial-wave content of the data, and thus the expected outcome of the selection, is known. The waveset selection is performed first on the MC data with perfect acceptance

(Section 5.3.3.1) and then on the MC data with realistic acceptance (Section 5.3.3.2).

5.3.3.1 Pseudodata with Perfect Acceptance

First, we perform the selection process on the set of MC pseudodata that does not include the effects of the detector acceptance. In order to investigate a possible mass-dependence of the procedure, it is performed in the four $m_{KK\pi}$ bins that have been introduced in Sections 5.1.4 and 5.2.1. We will present the results for two mass bins located at 1.81 GeV/c^2 and 2.21 GeV/c^2.

Fig. 5.18 shows the result of the waveset selection for the mass bin at 1.81 GeV/c^2. The intensities of the 673 partial waves in the wavepool obtained in the best regularized fit are plotted as blue points *in descending order*, i.e. the wave with rank 1, on the leftmost side of the plot, is the wave with the highest intensity; the wave with rank 2 has the second-highest intensity, etc. We see a clear structure in the plot: the intensity curve is not completely continuous but features a steep drop around a wave-intensity rank of 140. This is the point where the regularization term is taking effect. The waves can be classified into two categories: the waves left of the drop have a “significant” intensity, i.e. more than 1 event/(20 MeV/c^2), and are hence selected, while the waves right of the drop are forced to a lower intensity by the regularization term, and thus are deselected. The regularization of the fit thus seems to work at least in principle. However, there are some issues with the fit results. The intensity of the six waves that were used to generate the MC pseudodata are marked in the plot by red triangles. In the lower plot of Fig. 5.18, which shows the intensities of only the largest 20 waves, we can see that the fit misestimates the wave intensity significantly for the second- and fourth-largest waves. The wave with rank 4 is found with a higher intensity by the fit than its actual input intensity. Additionally, the fit finds at rank 5 a wave with large intensity which is not contained in the pseudodata. This wave has a larger intensity than two of the input waves. This already shows that the fit encounters some difficulties selecting the correct waves. However, a much more significant problem of this waveset-selection fit is the location of the intensity drop. As the MC pseudodata were generated using only six partial waves, the intensity drop caused by the regularization terms should ideally occur right after those six waves, or at most around rank 10. Contrary to our expectation, in our fit, there is no clear drop right ion this region. Despite the regularization terms, many waves not present in the MC data are found with a too large intensity.

This already shows that the waveset-selection fit has difficulties finding the

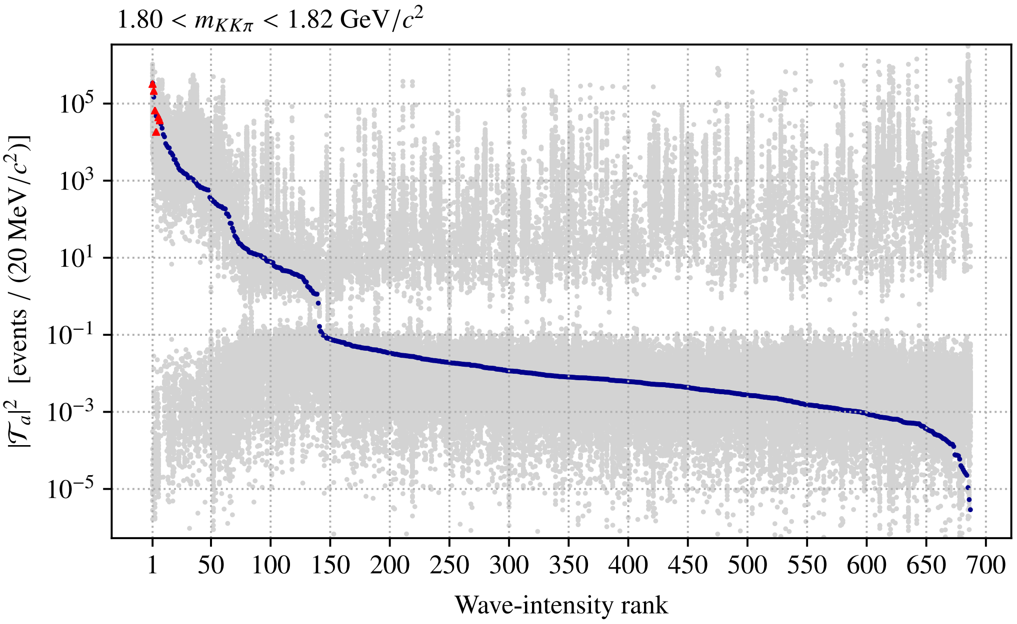

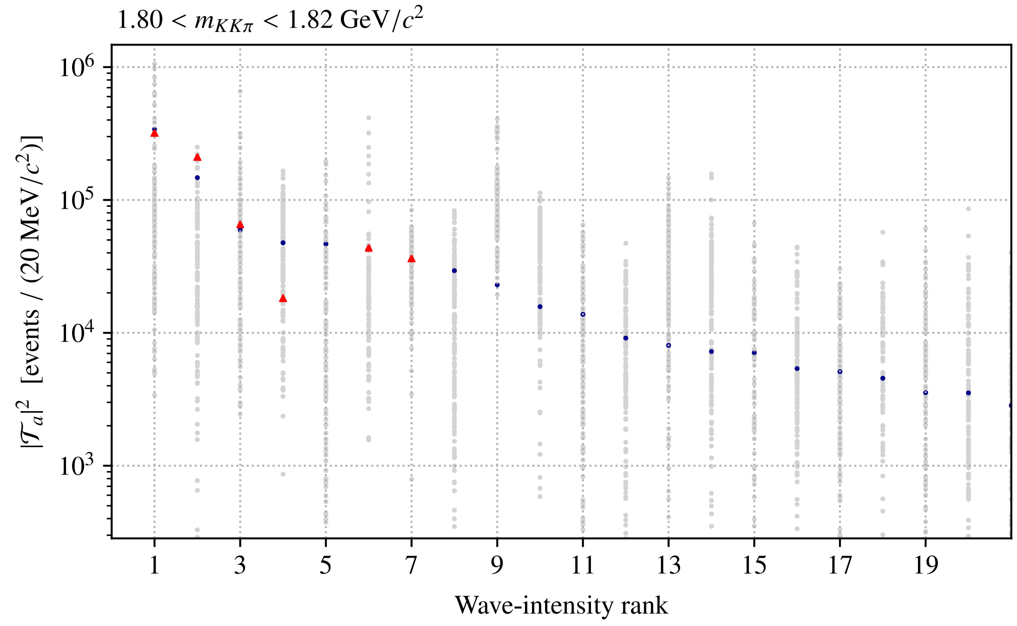

Figure 5.18: Result of the waveset-selection fit performed on the MC pseudodata sample with perfect acceptance in the mass region $1.80 < m_{KK\pi} < 1.82$ GeV/c^2. The upper plot shows the partial-wave intensities $|\mathcal{T}_a|^2$ of all waves in the wavepool, sorted according to the best fit attempt while the lower plot shows a close-up of the 20 waves with highest intensity. The best fit attempt is marked in blue, while the other 149 fit attempts are drawn in gray. The input intensities of the six waves that were used to generate the MC data are represented by red triangles.

correct waveset even in this idealized pseudodata case without the effects of acceptance. Yet another indication of the unreliability of the waveset selection is the strong multimodality of the fit. As explained in Section 5.3.1, 150 fit attempts have been performed. In Fig. 5.18, the waves are ordered according to their intensity as found in the 'best' fit attempt, i.e. the one with the highest likelihood value (blue points). The corresponding intensities obtained in the other 149 fit attempts are shown by gray points. We observe a large spread in the results from different fit attempts; they seem to often find quite different solutions. Normally, waves that are clearly deselected by the best fit attempt should also have little intensity in most of the other attempts. However, in our case, no wave is deselected in all attempts, and even waves with intensity above rank 200 to 300 are still found with large intensities in several fit attempts. Vice versa, even the highest-intensity waves in the best fit are deselected in some fit attempts. To gain more insight, we study the log-likelihood difference of the fit attempts with respect to the best attempt, which distribution is shown by the blue histogram in Fig. 5.21 (left). The 50 fit attempts with the highest likelihoods are marked in orange. Although many fit attempts have a likelihood value close to the maximum (situated on the origin of the abscissa), approx. 2/3 of the fit attempts have likelihood values that are far away from the maximum. In Fig. 5.19, the 50 fit attempts with the highest likelihood values are highlighted in orange (except the best fit attempt, which is plotted in blue as usual). One can see that the spread of intensity values is large even among these 50 best fit attempts.

The previous pseudodata studies discussed in Section 5.2 have shown that the reliability of the PWA fit depends heavily on $m_{KK\pi}$. In order to investigate the mass dependence of the waveset-selection fit, Fig. 5.20 shows the wave intensities resulting from the waveset selection fit for $2.20 < m_{KK\pi} < 2.22\ \text{GeV}/c^2$.

The sorted intensity distribution of the waves exhibits a clear drop around a wave-intensity rank of 75, as well as some smaller, less pronounced drops at higher intensities. There are still many waves that, although not present in the MC data, are attributed relatively large intensities by the fit. However, overall, the waveset selection seems to encounter less difficulties in this higher-mass region. Contrary to real data, where the amount of selected waves depends on the three-body mass because the intensity of the partial waves depends on $m_{KK\pi}$, the MC pseudodata have been generated with the same six waves contributing in all mass bins, and no such fluctuations are expected. We see that at $m_{KK\pi} = 2.21\ \text{GeV}/c^2$, fewer waves are located to the left of the intensity drop, i.e. are selected by the fit (c.f. Figs. 5.18 and 5.20). This

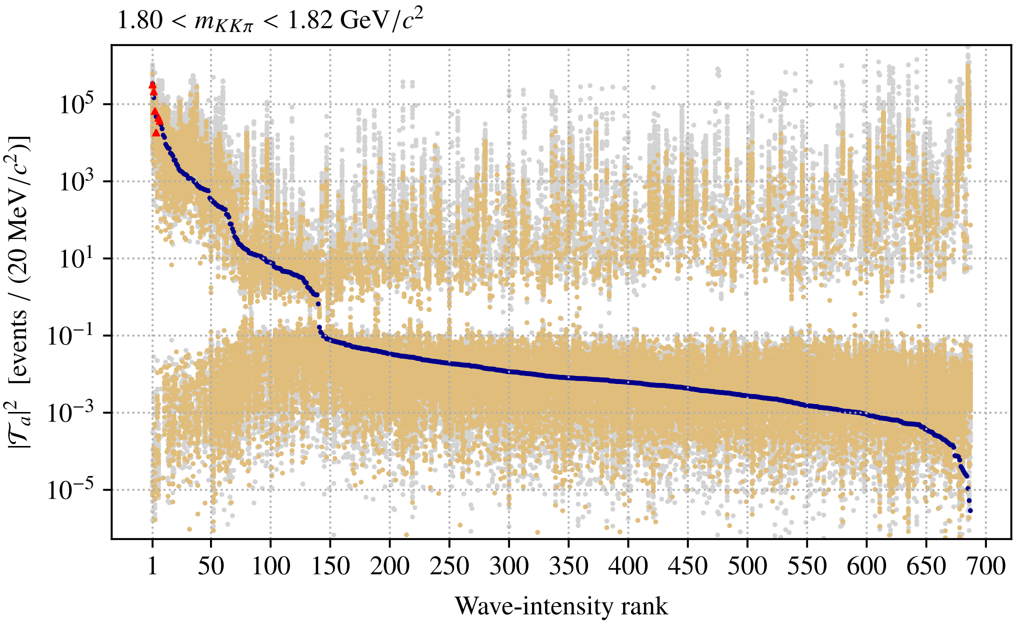

Figure 5.19: Similar to Fig. 5.18 (top), but with the 50 fit attempts with the highest likelihood values highlighted in orange.

is already an improvement. More importantly, in the waveset-selection fit at 2.21 GeV/c^2, the six input waves are actually the waves with the highest intensities, contrary to the fit at lower mass. Also, one can see a slight intensity drop, by a factor of about four, right after those six waves, which shows that the regularization term does reduce the intensity of all non-input waves, albeit by varying amounts. The distribution of the likelihood difference of the attempts w.r.t. the best fit attempt is shown in Fig. 5.21 (right). We still observe a large spread in the intensities of the different fit attempts, but the values of their likelihoods lie closer together.

The above studies show that, for the $K^-K^+\pi^-$ channel, the waveset-selection procedure unfortunately performs only poorly at best, even in the idealized case where we do not take into account acceptance effects and use a small PWA model containing only six waves. The multimodality of the waveset-selection fit shows the distinguishability problems of the PWA model that we already discussed in Section 5.1.4. Because many of the waves have similar phase-space distributions, the PWA model is able to describe the data similarly well using

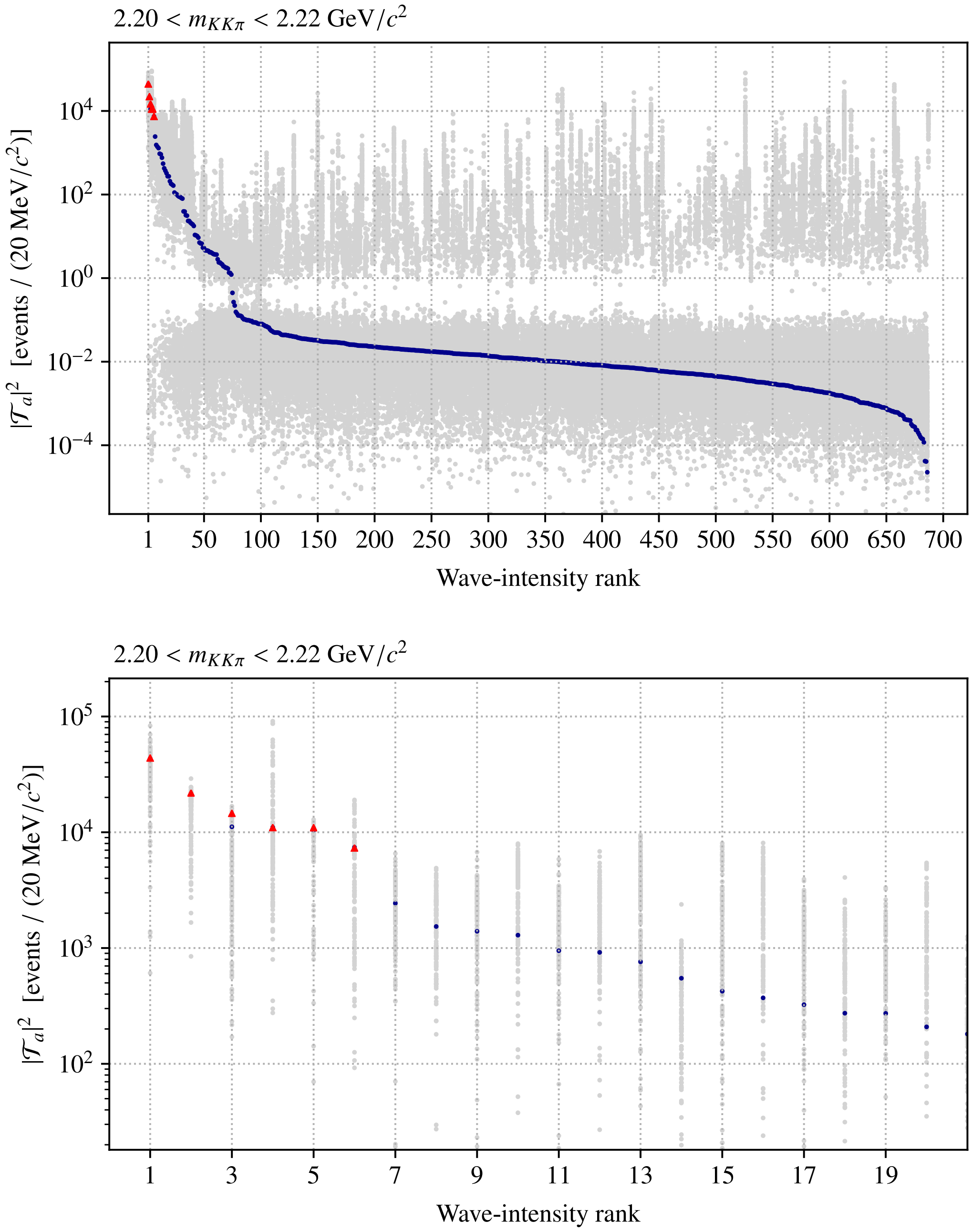

Figure 5.20: Similar to Fig. 5.18, but showing the results of the waveset-selection fit on the MC pseudodata sample with perfect acceptance, in the mass region $2.20 < m_{KK\pi} < 2.22$ GeV/c^2.

several different wavesets. As was expected from the previous studies, the fit reliability also depends on the $KK\pi$-system mass. While still far from perfect, the waveset selection seems to work better at higher $m_{KK\pi}$ above 2 GeV/c^2.

5.3.3.2 Pseudodata with Realistic Acceptance

In order to investigate the effects of the detector acceptance on the waveset-selection process, we perform the waveset-selection fit on the MC pseudodata samples that have been weighted with the acceptance. The results from this fit are shown in Fig. 5.22 for the mass bins at 1.81 GeV/c^2 and 2.21 GeV/c^2, respectively. The intensities of all 673 waves resulting from the best fit attempt are plotted in descending order, similar to Figs. 5.18 and 5.20. For both mass bins, clear drops in the intensity are visible around the wave-intensity ranks 110 and 40, respectively. From the previous pseudodata studies in Section 5.2, we expect a significant worsening of the reliability of the waveset selection when introducing acceptance effects. This is indeed the case, especially at masses below 2.2 GeV/c^2. At 1.81 GeV/c^2, one can clearly see that the result of the waveset-selection fit is at odds with the input-wave intensities. The input waves are not among the highest-intensity waves. Several non-input waves are found with even higher intensities. Even worse: four out of the six

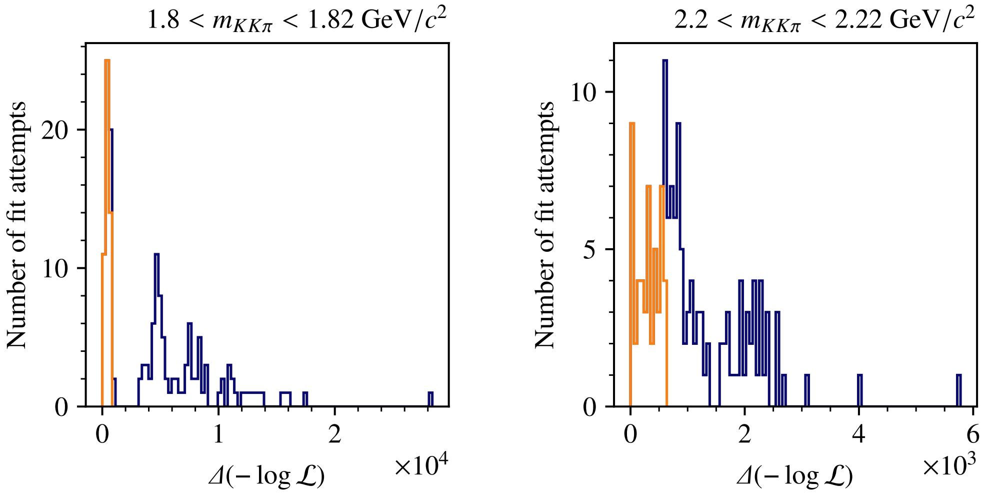

Figure 5.21: Distribution of the likelihood difference w.r.t. the highest likelihood $\Delta(-\log\mathcal{L})$ for 150 fit attempts of the waveset selection fit performed on the MC pseudodata sample with perfect acceptance for two mass bins. The 50 best attempts are marked in orange.

input waves are deselected by the fit, i.e. are found with almost no intensity. The partial-wave intensities have large spreads in the results of the different fit attempts. The distribution of the likelihood differences w.r.t. the best fit attempts is shown in Fig. 5.24 (left). Only a few fit attempts are close in likelihood to the best attempt, while most cluster roughly 1000 units in $\log\mathcal{L}$ away. We conclude that when including the acceptance effects, the waveset selection fails completely in the 1.8 GeV/c^2 mass range, and the results are, unfortunately, unusable.

This is also true for the 1.61 GeV/c^2 mass bin. Even at 2.01 GeV/c^2, the waveset selection exhibits similar issues as discussed above. Only at 2.21 GeV/c^2, the waveset selection improves somewhat. Firstly, only 40 waves are selected by the fit, and the selected waves include all six input waves. The set of selected waves is hence considerably smaller than in the other three mass bins. As can be seen in the close-up of the first 50 waves in Fig. 5.23, the input waves are among the highest-intensity waves, although for three waves, there are significant differences between their fitted intensities and the input values. The multimodality again leads to a large spread of the intensities across the fit attempts, but the number of fit attempts in which deselected waves have high intensities is considerably lower than at lower masses. The fit attempts also lie closer in likelihood, which can be seen in Fig. 5.24 (right).

To conclude, the waveset-selection procedure does not yield the expected results when applied on the sets of $K^-K^+\pi^-$ pseudodata with and without effects of the detector acceptance. Already with perfect acceptance, the waveset-selection fit does not manage to select the correct waveset. Similar to previous studies in Section 5.2.4, the reliability of the waveset-selection fit deteriorates significantly when using a realistic detector acceptance. In addition, all waveset-selection fits suffer from an unexpectedly high multimodality. We observe a large dependence of the reliability of the waveset-selection fit on $m_{KK\pi}$: results below 2.0 to 2.2 GeV/c^2 are unusable; the situation improves slightly above this mass range. The reliability of the waveset-selection fits performed on real data is expected to suffer from similar issues. Nevertheless, some results from a waveset selection of the real $K^-K^+\pi^-$ data will be presented in the next section, along with some additional indications on the (un)trustworthiness of the results.

5.3.4 Waveset Selection on Real Data

In this section, we present the results of a waveset-selection fit that was performed on the real dataset (see Chapter 4) in all mass bins in the range $1.5 < m_{KK\pi} < 3.5$ GeV/c^2 and in the lowest t' bin $0.1 < t' < 0.15$ (GeV/c)^2.

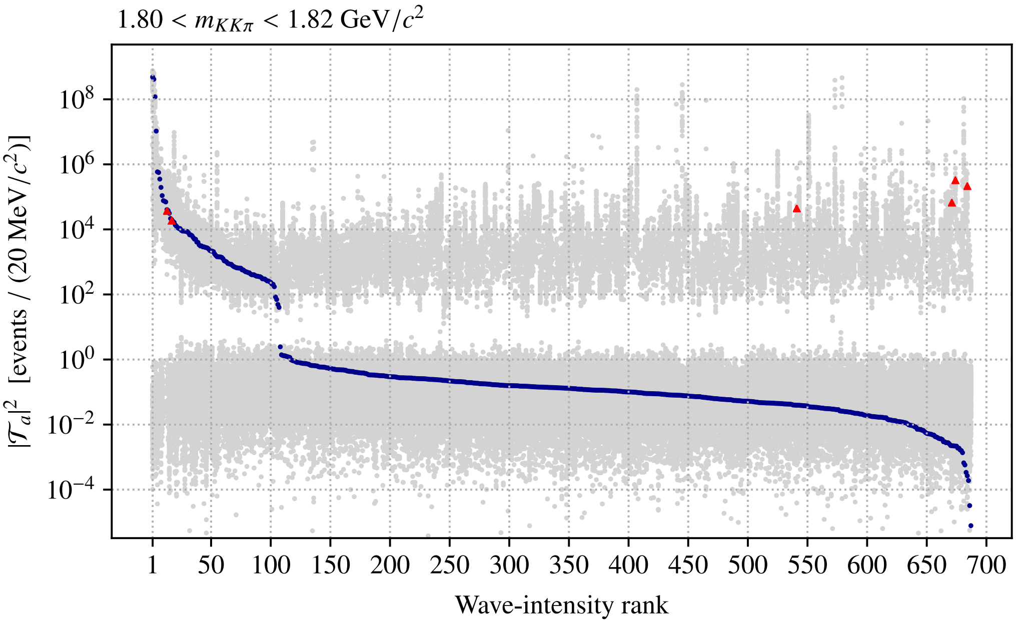

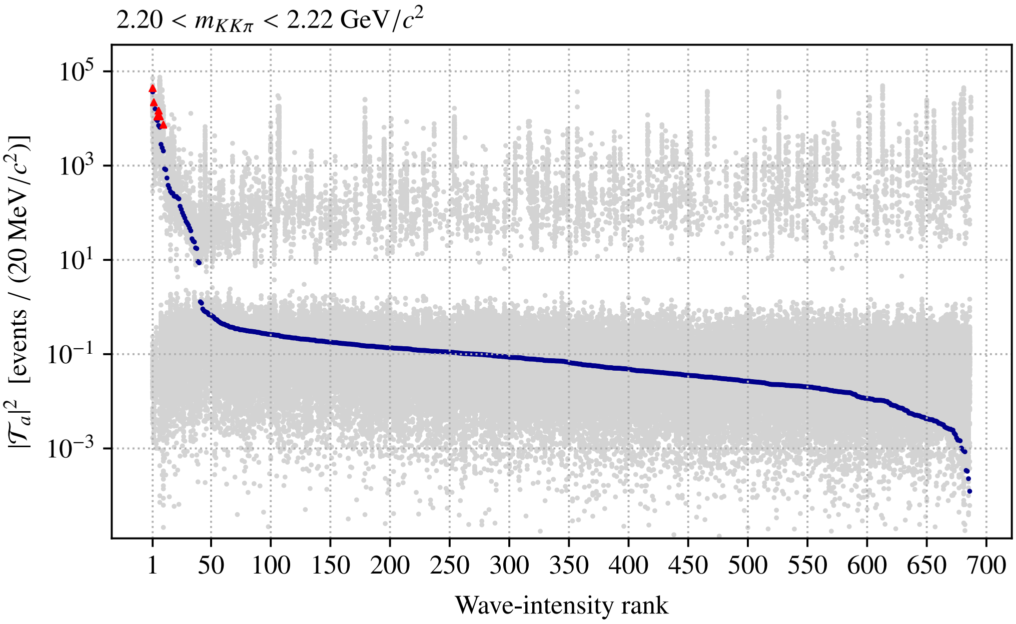

Figure 5.22: Similar to Fig. 5.18, but showing the results of the waveset selection on the accepted MC pseudodata sample, in the mass regions $1.80 < m_{KK\pi} < 1.82$ GeV/c^2 (upper plot) and $2.20 < m_{KK\pi} < 2.22$ GeV/c^2 (lower plot).

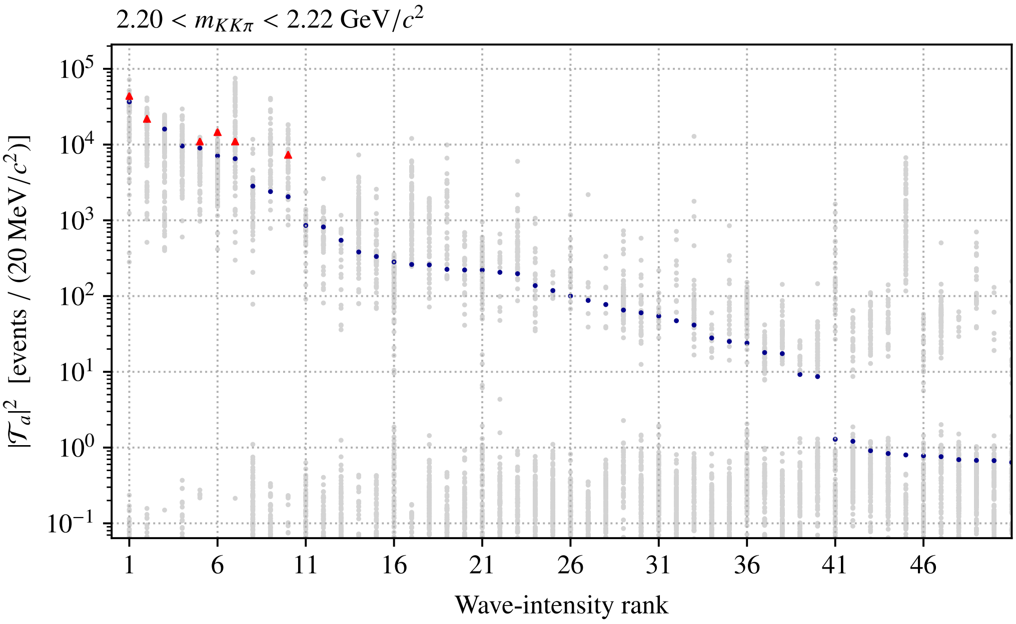

Figure 5.23: Close-up of Fig. 5.22 (bottom), showing the 50 waves with highest intensities in the waveset-selection fit performed on the accepted MC pseudodata sample at $2.20 < m_{KK\pi} < 2.22$ GeV/c^2.

The wavepool used in the fit is the one same as in the MC studies (see Sections 5.3.2 and 5.3.3). One notable difference is the use of a new parametrization for the $K\pi$ S-wave, where the wave amplitude is split up into two elements $[K\pi]_S^{K\pi}$ and $[K\pi]_S^{K\eta}$, representing the different decay channels of the isobar resonance, which can interfere. This parametrization was taken from Refs. [11, 12] and is described in more detail there. The parametrization does not differ significantly from the LASS parametrization [15] that we used before in the first real-data PWA (see Section 5.1) and in the pseudodata studies (see Section 5.2), but it describes the data slightly better.

Figure 5.25 shows the intensities of all waves in the wavepool ranked by intensity, in a similar fashion as Figs. 5.18, 5.20 and 5.22, for the two bins at $m_{KK\pi} = 1.81$ GeV/c^2 and $m_{KK\pi} = 2.21$ GeV/c^2. For the best fit attempt, the regularization term does take effect: a very clear drop in intensity is observed around wave-intensity ranks 110 and 140, respectively. As was discussed in Section 5.3.3, this unfortunately does neither validate the procedure's reliabil-

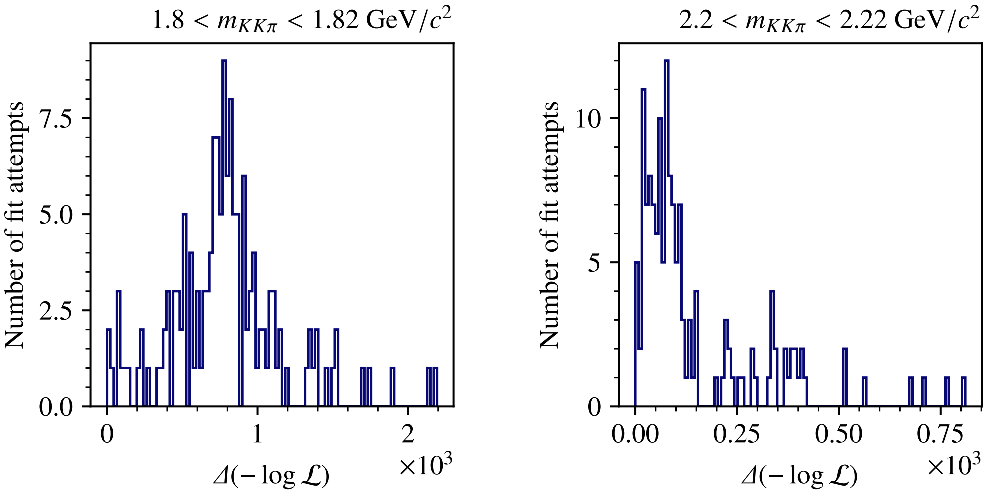

Figure 5.24: Distribution of the likelihood difference w.r.t. the highest likelihood $\Delta(-\log\mathcal{L})$ for 150 fit attempts of the waveset selection fit performed on the accepted MC pseudodata sample for two mass bins.

ity, nor does it mean that the selected waves are those actually present in the data. Similar to the MC studies, the wave intensities found in the other 149 fit attempts (gray points) have a large spread indicative of the high multimodality of the waveset-selection fit. Here, contrary to the pseudodata studies, the correct results are obviously unknown, so that no direct validation of the fit results can be given. However, the intensity distribution of the partial waves in $m_{KK\pi}$ may give indications on the reliability of the fit. Figure 5.26 shows the intensity distributions of the ten largest waves as a function of $m_{KK\pi}$. First of all, we can compare those waves to the waveset used in the VES analysis [14]. If the waveset-selection results are correct, the two sets should contain the same waves. Firstly, we see that four out of the ten waves in Fig. 5.26 are waves with $K\pi$ S-wave isobars. While the $0^-0^+[K\pi]_S KS$ and $2^-0^+[K\pi]_S KD$ do have significant intensity in our and in the VES results, the two other waves with $K\pi$ S-wave isobars, i.e. the $2^-1^+[K\pi]_S KD$ and $3^-0^+[K\pi]_S KF$ waves, do not appear in the VES waveset. Except for the $2^-0^+K_2^*(1430)KS$ wave, which has the tenth-largest intensity, the other selected waves are also not present in the VES waveset. In addition, the intensity distributions in Fig. 5.26 exhibit unphysical properties. We especially see a clear lack of continuity in the intensity distributions of all waves, i.e. waves are selected with large intensity in some $m_{KK\pi}$ bins, but deselected by the regularization term in adjacent bins.

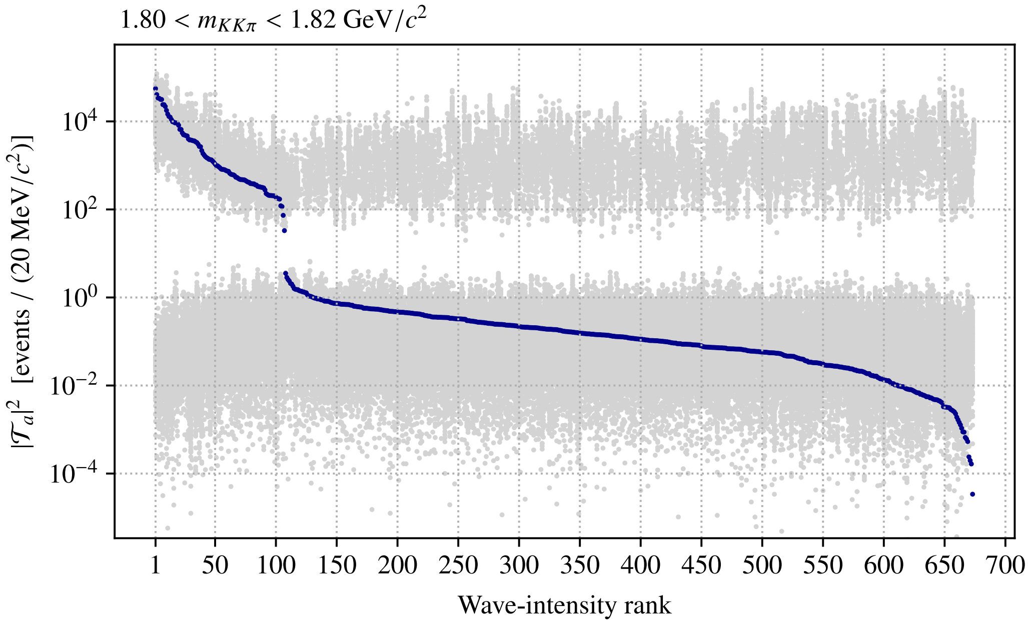

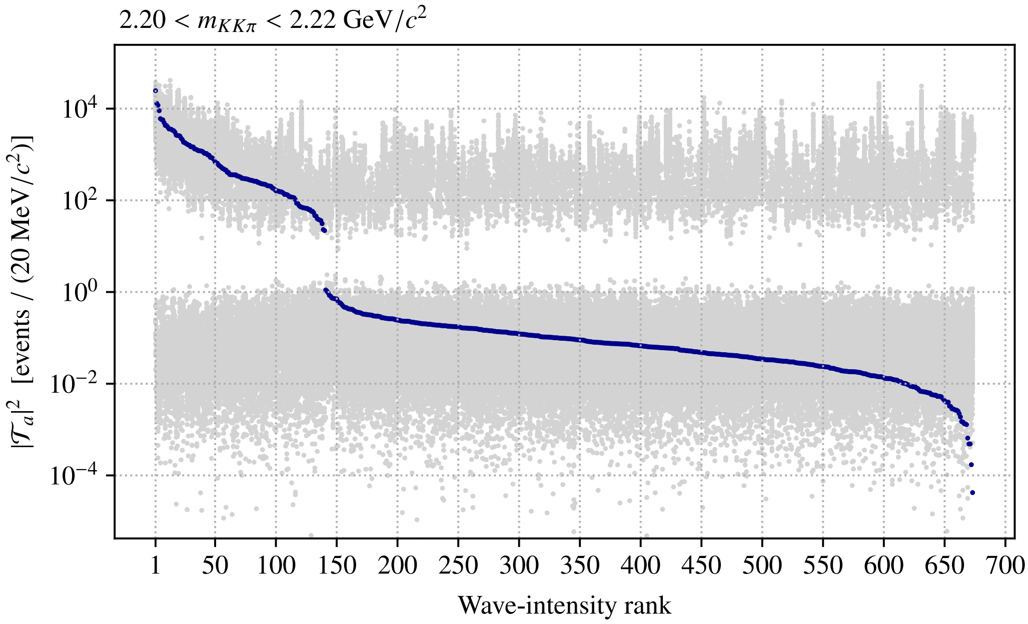

Figure 5.25: Similar to Fig. 5.18, but showing the results of the waveset selection on the $K^-K^+\pi^-$ real dataset, in the mass regions $1.80 < m_{KK\pi} < 1.82$ GeV/c^2 (upper plot) and $2.20 < m_{KK\pi} < 2.22$ GeV/c^2 (lower plot).

None of the waves exhibits a clear continuous peak structure below 2 GeV/c^2 although such structures have been observed in the VES analysis. This further hints to the fact that the waveset selection fails also in the real-data case.

The previous studies on pseudodata have demonstrated the unreliability of the PWA fit and the waveset selection at least for masses below 2 GeV/c^2. The results on the real dataset seem to confirm that the waveset-selection fit does not yield correct results for the $K^-K^+\pi^-$ channel. Unfortunately, applying the waveset selection in order to improve the PWA waveset was our last option to counter the issues caused by the inhomogeneous detector acceptance and to possibly obtain valid PWA results for $K^-K^+\pi^-$.

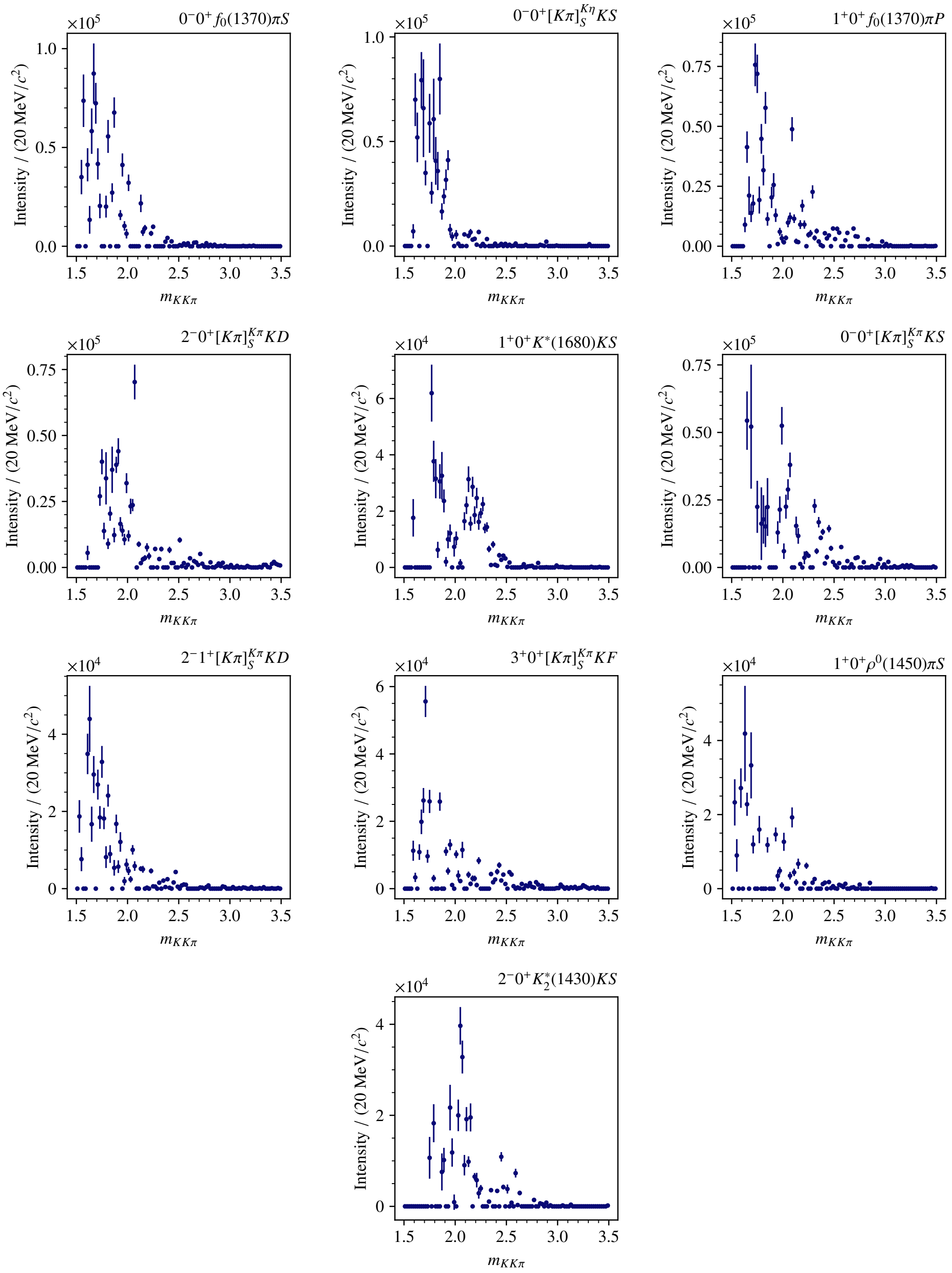

Figure 5.26: Intensity distributions as a function of $m_{KK\pi}$ for the 10 waves with the largest intensities in the waveset-selection fit of $K^-K^+\pi^-$ real data.

Chapter 6

Conclusions and Outlook

The goal of the first part of this thesis was to attempt a partial-wave analysis of the inelastic scattering reaction $\pi^- + p \to K^- K^+ \pi^- + p$, in order to study the resonance content of the intermediate states X^- produced during the reaction. We use a large dataset of 2.02×10^6 diffractive-dissociation events, recorded at the COMPASS spectrometer at CERN in 2008.

We have performed a first partial-wave decomposition of the data, in which the amplitude of the process is decomposed into waves with different quantum numbers and the intensity in each wave is determined from the data. The PWA has brought to light a number of serious and unexpected issues. The $m_{KK\pi}$ distributions of the partial-wave intensities as obtained from the PWA fit exhibit a significant and unphysical lack of continuity and several resonances expected to appear in these distributions, such as the prominent $\pi(1800)$, are not found. The extremely high relative intensity of above 20% of the flat wave, a phase-space isotropic distribution used to absorb background processes and misreconstructed events, indicates that the phase-space distributions of many waves appear nearly isotropic to the fit and are thus difficult to distinguish. This leads to uncontrolled redistribution of the intensities across the partial waves. These findings were further backed up by a wave-by-wave comparison between our results and results from a previous, successful analysis of the same final state by the VES collaboration [14]. The comparison presented significant discrepancies between our and the VES results especially in the $m_{KK\pi}$ range between 1.5 and 2.0 GeV/c^2, while at higher masses, the intensity distributions of some waves become more similar.

In an attempt to improve the PWA fit, we tried to optimize the waveset used in the PWA fit by applying a model-selection technique on the dataset. This technique aims to select those waves that contribute most to the data (see Section 5.3), and was successfully applied to other channels. Unfortunately, applied to the $K^- K^+ \pi^-$ data, the waveset-selection fit encountered similar problems as discussed above, despite the method repressing waves that are only weakly supported by the data.

We identified two effects that could lead to the encountered issues of the PWA fit. The isobar model, used in this analysis, assumes that resonances appear not only in the produced excited states X^-, but also in the K^+K^- and $K^+\pi^-$ subsystems. These resonances ξ have their own quantum numbers, e.g. total angular momentum and parity J_ξ^P. The S-wave isobar resonances have $J_\xi^P = 0^+$, which means that there is no angular dependence in their decay. They are also very broad and difficult to resolve, and thus cannot be represented by simple Breit-Wigner amplitudes, but have to be described by more complicated parametrizations. If in addition, the excited state X^- also has $J = 0$, there is no angular dependence at all in the X^- decay, which renders these states even more difficult to distinguish. The fact that these waves are expected to have significant intensity in the data [14] makes this a very tangible problem.

In addition to the inherent indistinguishability of some waves mentioned above, further, more severe distinguishability issues between waves can arise if their angular distributions differ predominantly in phase-space regions in which the acceptance is null or very low. This leads us to a second, more crucial problem of the $\pi^- + p \to K^-K^+\pi^- + p$ channel. For the PWA to work, and to separate the process from the dominant process $\pi^- + p \to \pi^-\pi^+\pi^-$, all three final-state particles have to be identified. As the RICH-1 detector that is used for the particle identification can separate kaons from pions only at momenta between approximately $10 - 60$ GeV/c, while the total beam momentum of 190 GeV/c is distributed among the final-state particles, many events have to be rejected. This affects in particular particle momenta above 45 to 60 GeV/c, which translates into larger regions of phase-space containing only very few events at three-body masses approximately below 2 GeV/c^2. The effect seems to gradually improve at higher masses. The strongly non-uniform acceptance can cause problems in the PWA fit procedure.

In order to investigate the encountered issues and identify their source as well as gauge the reliability of the PWA fit, two series of studies on Monte Carlo pseudodata have been performed. A first set of Monte Carlo data has been generated using values for the six largest partial-wave amplitudes from the VES analysis [14] in four exemplary mass bins that cover the $K^-K^+\pi^-$ mass range between 1.6 and 2.2 GeV/c^2. A second set of MC data has been derived from the first one by additionally taking into account the effects of the acceptance of the detector setup, as well as of the event reconstruction and event selection. We performed the PWA fit procedure on both MC datasets first including only the six waves with which the MC data were generated, and then using a larger waveset. We then compared the partial-wave amplitudes estimated by the PWA fit to their known input values in the different $m_{KK\pi}$ bins. This enabled us to study the behavior of the PWA fit with and without the effects of detector acceptance as well as its dependence on $m_{KK\pi}$. In the first set of studies, performed on the MC data with perfect acceptance, some small, but statistically significant differences between the amplitude values from the PWA fit and their input values arose. These could be explained by the inherent distinguishability issues of waves with KK and $K\pi$ S-wave isobars discussed above. Overall, the results of the PWA fit were still in good agreement with the expected outcomes in all $m_{KK\pi}$ bins. The second set of studies, performed on the set of accepted MC pseudodata, however, had a significantly different outcome. There, drastic differences in the behavior of the PWA fit were observed across the various mass bins. At masses below 2 GeV/c^2, the PWA fit completely fails to estimate the correct values of the partial-wave amplitudes. Large deviations between the input values and the fit output appeared especially in the phases of the amplitudes. At higher masses, above approx. 2 GeV/c^2, the situation gradually improves, and the PWA fit is able to reproduce the input values of the amplitudes more reliably. However, when including waves that were not contained in the MC data, the reliability worsens also at higher masses, with especially the structureless flat wave gaining significant intensity. This situation is more similar to the real-data case, where the chosen waveset cannot be perfectly accurate.

In order to investigate the unsuccessful application of the waveset-selection procedure on the real dataset, we performed the procedure on the two sets of MC data in a similar fashion to the previous pseudodata studies. The waveset-selection fits seemed to encounter difficulties already in the idealized case without effects of the detector acceptance. The fit had trouble estimating the intensities of the input waves correctly, and selected many waves that were not actually present in the MC data. As expected from the previous MC studies, these issues became much worse in the second study, when acceptance came into play. The waveset selection on the accepted MC dataset failed completely at masses below 2.2 GeV/c^2. We also observed a severe multimodality in all waveset-selection fits, which underlines the lack of distinguishability of many waves, even with perfect acceptance.

These various MC studies on the behavior of the PWA fit in the $K^-K^+\pi^-$ channel indicate that the fit becomes extremely unreliable when we take into account the acceptance of the setup. As the issues arising in the PWA fits of

MC data are similar to those observed in real data, we conclude that the non-uniform detector acceptance is the main cause for the problems encountered in the $K^-K^+\pi^-$ real-data PWA fit. As the acceptance is especially inhomogeneous at masses below 2 GeV/c^2, any results in this mass range are expected to be unreliable. This region is, however, crucial to cross-check our results with those of other experiments, as the well-known resonances lie there. Observed higher excited states in the high-mass region would be doubtful without such a confirmation of the validity of the fit. We therefore conclude that a reliable PWA of the $K^-K^+\pi^-$ final state with the COMPASS data is not possible with the current acceptance.

The acceptance effects unfortunately cannot be improved in the data. The main reason for the non-uniform acceptance is the identification of the final-state particles, which is mandatory for the PWA. One possibility of improving the acceptance would be to use additional particle-identification detectors to improve the PID. This is considered in a successor experiment named COMPASS++/AMBER [17]. Several measurements are planned, including high-precision strange-meson spectroscopy. For this, an upgrade of the beam line is considered to generate an RF-separated kaon beam. RF separation is a technique based on radio-frequency cavities that separate components of the beam using time-of-flight. This could drastically increase the fraction of kaons in the beam and allow to obtain much larger datasets on e.g. kaon-diffraction processes. In addition, upgrades and extensions of the spectrometer itself are planned, especially regarding the kinematic region covered by the particle-identification, by installation of new RICH detectors. This could significantly increase the detector acceptance and make it more uniform across the phase space, preventing the issues discovered in this thesis. Thus, an analysis of the reaction $\pi^- + p \to K^-K^+\pi^- + p$ could very well be possible with future datasets from the COMPASS++/AMBER experiment.

Part II

Event Selection and Analysis of the $K_s^0\pi^-$ and $K_s^0K^-$ Final States

Chapter 7

Selection of $K_s^0\pi^-$ and $K_s^0K^-$ Events

The goal of the event selection is to single out events produced by the studied inelastic scattering reactions $K^- + p \to K_s^0\,\pi^- + p$ and $\pi^- + p \to K_s^0\,K^- + p$. The data used here have been recorded at the COMPASS spectrometer, presented in Chapter 2, in the years 2008 and 2009. The event selection is performed separately on the datasets of the two years. It is divided into two steps: The preselection stage aims to broadly select events stemming from the more general reaction $h_b^- + p \to V^0 + ... + h^- + p$, where a negative beam hadron h_b^- interacts with a target proton to produce at least one neutral particle V^0 as well as one negative final-state hadron h^-. In the fine-selection stage, narrower cuts are applied to obtain pure event samples of exactly the reactions of interest. The initial event samples contain 7.39×10^9 events in the year 2008 and 5.98×10^9 events in the year 2009.

7.1 Preselection of the Data

In order to reduce the data sizes to a more convenient level, a preselection is first performed on the unprocessed dataset, in which broad cuts are applied. We require the events to match the generic reaction $h_b^- + p \to V^0 + ... + h^- + p$. V^0 particles, such as the K_s^0, are neutral and are therefore not detected directly in the spectrometer. However, they decay into pairs of oppositely charged particles, which leave tracks in the spectrometer. Events with V^0 particles are identified by the appearance of secondary vertices, from which the daughter particles emerge. In addition to the reactions of interest, $K^- + p \to K_s^0\,\pi^- + p$ and $\pi^- + p \to K_s^0\,K^- + p$, the preselected data can still contain events stemming from similar reactions. It can therefore also be used in the analyses of other final states, such as $\pi^- + p \to K_s^0\,K_s^0\,\pi^- + p$.

To select events in which the beam interacts with the target, we require that the event was triggered by the diffractive trigger. It consists of three independent trigger signals: First, beam particles set off a signal in scintillating fiber detectors installed upstream of the target, which ensures that a beam particle is entering the target cell. The second signal comes from the Recoil Proton Detector (RPD), which requires that a proton is recoiling from the target due to the interaction of the beam particle. Finally, a veto system suppresses events with non-interacting beam particles, events with beam particles far from their nominal trajectory, and events with final-state particles outside of the geometrical acceptance of the detector. Most events are selected by the diffractive trigger.

The RPD is used again outside the trigger system: we apply an additional cut that ensures that the RPD has detected a proton track and that the track begins inside the target.

To ensure well-defined and unambiguous kinematics, we require the presence of exactly one primary vertex, i.e. one point of interaction between the beam and the target particle.[1] The primary vertex must be located in the range $-200 < Z_{\mathrm{PV}} < 160$ cm along the beam axis. In the studied reactions, exactly one charged particle is leaving the primary vertex. We hence cut out all events for which this is not the case. We additionally require charge conservation, which automatically forces the primary scattered particle to have negative charge.

Since we want to study reactions in which neutral particles are produced, we require the presence of one or more secondary vertices.[2] The secondary vertices have to fulfill the following criteria: Exactly two secondary charged particles must be detected coming from the secondary vertex. The track parameters of these particles must be found correctly, and the particles must have opposite charge. Although there is only one V^0 particle in the reactions to be studied, we do not restrict the number of secondary vertices during the preselection, as further cuts in the finer selection can remove extra secondary vertices and leave only the secondary vertex corresponding to the decay of the K_s^0. In order to further reduce the number of events, a first, broad cut on the reconstructed V^0 mass is done. The four-momentum of the V^0 is reconstructed by summing the four-momenta of the particles that leave the secondary vertex with the assumption that the two outgoing particles are $\pi^\pm$. The invariant mass of the V^0 particle is then restricted to the region $|m_{\pi\pi} - m_{K^0}^{\mathrm{nom}}| < 5$ MeV/c^2 around the nominal mass $m_{K^0}^{\mathrm{nom}} = 497.611$ MeV/c^2 of the K^0 [13]. The preselection

---

[1] Additionally, we require that the Z-coordinate of the vertex is defined, in order to assure that the vertex has been correctly found.

[2] Secondary vertices, as opposed to primary vertices, are not associated with a beam track.

lowers the amount of events significantly, to 17 051 440 events in 2008 and 16 727 290 events in 2009.

7.2 Fine Selection of the $K_s^0\,\pi^-$ and $K_s^0\,K^-$ Final States

The fine selections of the $K_s^0\,\pi^-$ and $K_s^0\,K^-$ final states are very similar, and only differ in the cuts used to select the particle species in Section 7.2.2. We will thus discuss the two selections together. Both selections start with the set of preselected events (see Section 7.1). In the following sections, we will show event distributions of various variables. Unless explicitly stated otherwise, the shown distributions are with all selection cuts applied except the cuts in the plotted variable(s). We will show the distributions for both final states separately. The two datasets from 2008 and 2009 are overlaid in the same plots, with the distributions from 2009 scaled to the total number of events in the 2008 dataset. To some distributions, a function, usually the sum of signal and background components, is fitted to extract cut parameters, such as the width of the distribution's peak. To avoid clutter, the fitted function and its different components are drawn for the 2008 dataset only. As we will show, most distributions of the 2008 and 2009 datasets are compatible. Thus, most of the used cut values, that are indicated by gray lines in the plots, are the same for both datasets. In case the distributions and hence the cuts differ, the cuts for 2008 data are indicated by solid lines and those for 2009 data by dashed lines.

We group the applied cuts into four categories, which will be presented in the following sections.

7.2.1 Cuts on Event Topology

In order to prevent pile-up, i.e. the situation in which two beam particles enter the experiment at about the same time, we require a coincidence between the trigger time and the time of the beam track.The distributions of the beam time for $K_s^0\pi$ and K_s^0K are shown in Fig. 7.1. We restrict the difference between the trigger time and the mean of the beam time distribution to within plus-minus three times the time resolution. The latter is estimated by fitting the distribution of the beam time using a double Gaussian as signal function and a polynomial of second degree to describe the background, i.e.

$$f(t_B; A, r, \mu, \sigma_1, \sigma_2; a, b, c) = A\big[r \cdot \mathcal{N}(t_B; \mu, \sigma_1) + (1-r) \cdot \mathcal{N}(t_B; \mu, \sigma_2)\big] \\ + a\,t_B^2 + b\,t_B + c \; . \tag{7.1}$$

with $\mathcal{N}$ the Gaussian distribution

$$\mathcal{N}(x; \mu, \sigma) = \frac{1}{\sqrt{2\pi}\sigma} \cdot e^{-\frac{1}{2}\frac{(x-\mu)^2}{\sigma^2}} \tag{7.2}$$

The time resolution is then calculated as the weighted average of the standard deviations of the two Gaussians, i.e.

$$\sigma_{t_B} = r\,\sigma_1 + (1-r)\,\sigma_2 \; . \tag{7.3}$$

The curves in Fig. 7.1 show the result of a fit of Eq. (7.1) to the 2008 data. Since the distributions for 2008 and 2009 differ, especially regarding the mean of the distributions, the fits lead to different cut ranges:

$$-2.116 < t_B < 2.432 \text{ ns and } -2.571 < t_B < 2.469 \text{ ns} \tag{7.4}$$

for the 2008 and 2009 datasets, respectively.

To help ensure that the beam particle interacts with the target, we select only events where the primary vertex is located inside the target volume. The distributions of the primary vertex position are shown for $K_s^0\pi^-$ and $K_s^0K^-$ in Fig. 7.2. We cut on the radial and axial position of the vertex using the ranges: $-66 < Z_{\mathrm{PV}} < -29$ cm and $R_{\mathrm{PV}} = \sqrt{X_{\mathrm{PV}}^2 + Y_{\mathrm{PV}}^2} < 1.55$ cm. No significant differences are observed between the two final states. The two-dimensional distribution of X_{PV} against Y_{PV} is shown for the 2008 dataset only, as the distribution for 2009 is similar. The distributions of Z_{PV} for 2008 and 2009 are also compatible. We see that the primary vertex lies mostly inside the target. Hence, the cuts affect only few events.

7.2.2 Cuts on Particle Species

Different beam-particle species are required to produce the two investigated final states. The negative hadron beam from the SPS M2 beam line consists predominantly of pions, with a small admixture of kaons, which must be carefully separated. The particle identification (PID) of the beam is performed by the two CEDAR detectors located upstream of the target. For the $K_s^0\pi^-$

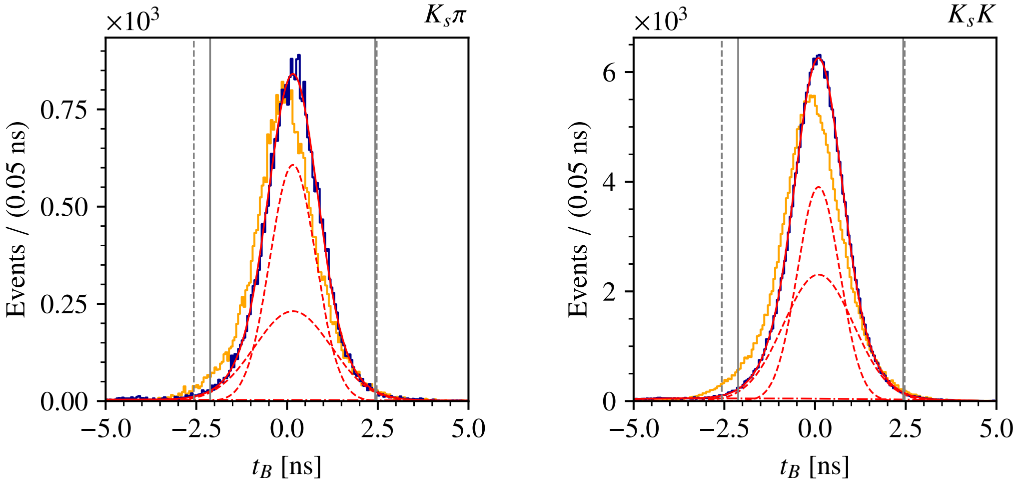

Figure 7.1: Beam time distribution of the events for (left) $K_s^0\pi$ and (right) K_s^0K. The beam time distributions of the 2008 (blue) and 2009 (orange) datasets are overlaid. The cut values are indicated by the gray vertical lines. The curves show the result of a fit to the 2008 data, with the overall fitted curve drawn as a solid red line and its signal and background components as dashed lines.

final state, we require that the incoming beam particle is identified as a kaon, whereas for $K_s^0K^-$, we require that the beam particle is identified as a pion. Events where the beam particle cannot be identified are rejected. We use the same beam-PID technique as in Ref. [18]. The exact procedure is explained in detail there.

The identification of the final-state particles is performed by the RICH-1 detector, presented in Section 2.2. For the reactions investigated here, the identification of the final-state particles is less important than for other channels. We mostly rely on the conservation of isospin, G-parity and/or strangeness in the strong interaction that mediates the scattering process and do not require a strict identification of the final-state particles. Instead, we simply veto out the undesired particle species. For the $K_s^0\pi^-$ final state, events in which the primary scattered particle is identified as kaon or proton are rejected. For the $K_s^0K^-$ final state, events in which the primary scattered particle is identified as pion or proton are rejected. The two secondary particles from the K_s^0 decay are supposed to be pions. Thus, events where any of the secondary particles is identified as a kaon are rejected for both final states. Unlike for the beam PID, events are also accepted in all cases if the final-state particles could not

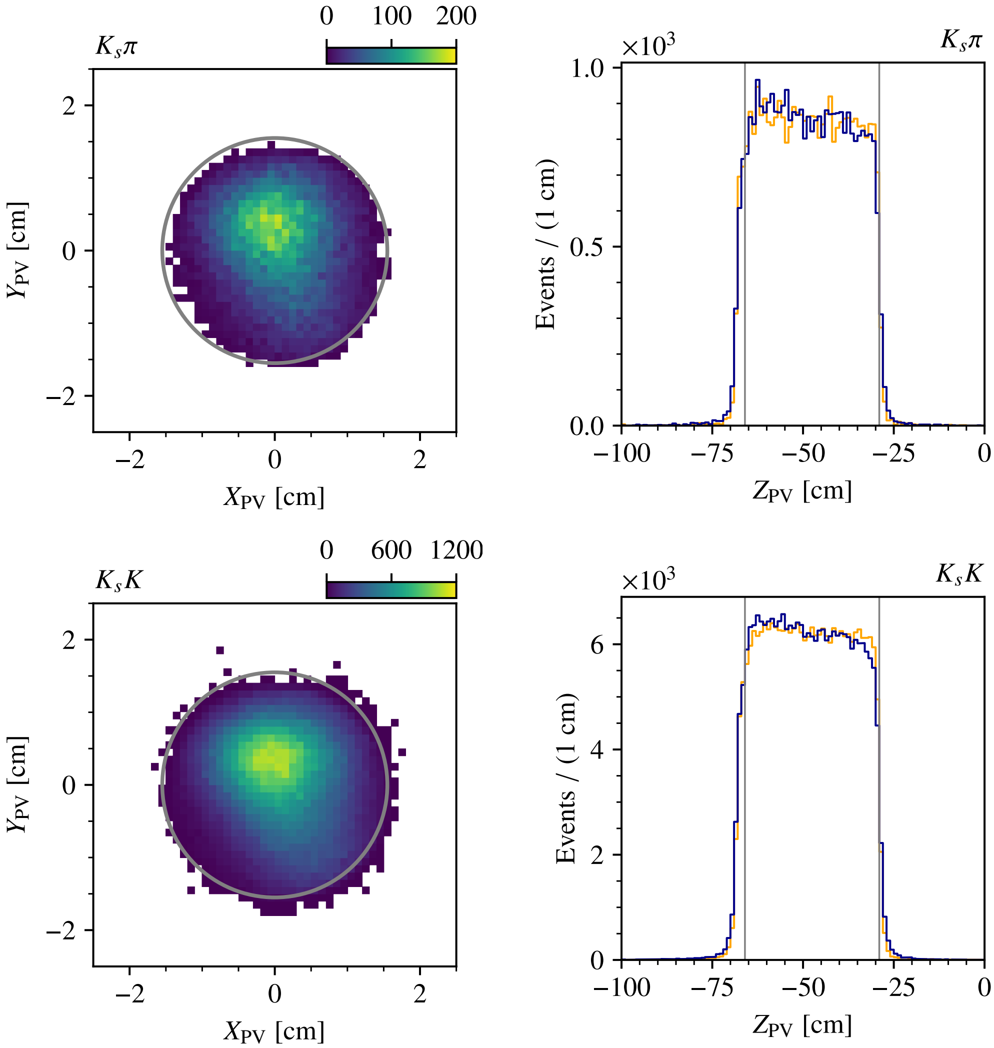

Figure 7.2: Distributions of the primary vertex position for (top row) $K_s^0\pi$ and (bottom row) K_s^0K. The left plots show the radial position for the 2008 dataset. The right plots show the axial position for both 2008 (blue) and 2009 (orange). The cut ranges are indicated by (left) the gray circle and (right) the gray vertical lines.

be identified by the RICH detector. Again, details on the approach for the RICH PID procedure can be found in Ref. [18], as well as in Section 4.1.2.

7.2.3 Cuts on the V^0 candidates

Most of the cuts applied up to this point concern the whole event, which may include multiple V^0 candidates. In the following, we present cuts on the V^0 candidates and their properties. The goal is to select events with exactly one secondary vertex coming from the decay $K_s^0 \to \pi^+\pi^-$. Thus, an event is discarded if all its secondary-vertex candidates are removed by the cuts, or if more than one secondary vertex remains after the selection. The four-momentum of the V^0 candidate is calculated by summing the four-momenta of its decay products. The masses of the two particles, of which there are several possibilities depending on the V^0 particle and its decay,[3] must be explicitly given. Here, we assume the V^0 to be a K_s^0 decaying into $\pi^+\pi^-$.

First, we cut on the position of the secondary vertices. As in both reactions under study, the K_s^0 is emitted in forward direction, the secondary vertex must be located downstream of the primary vertex. Thus, we restrict the separation ΔZ along the Z-axis between the primary and the secondary vertex to values larger than the sum of the uncertainties on the Z-position of both vertices, i.e.

$$\Delta Z = Z_{\mathrm{SV}} - Z_{\mathrm{PV}} > \sigma_{Z,\mathrm{SV}} + \sigma_{Z,\mathrm{PV}} \ . \tag{7.5}$$

The distributions of the secondary-vertex position are shown in Fig. 7.3, with all cuts applied. The radial position is only plotted for 2008 data, but is similar in 2009. It is centered around the Z-axis, as expected. The distributions of the vertex position along Z have similar structures in $K_s^0\pi^-$ and $K_s^0K^-$ but differ in details. This also leads to differences in the distribution of the vertex Z-separation ΔZ, shown in Fig. 7.4. We observe no significant discrepancy between 2008 and 2009 distributions. We expect exponentially falling distributions, with a slope depending on the K_s^0 lifetime. However, because of the irregular disposition of the detectors in the setup, the distributions are distorted.

Additionally, we verify that none of the outgoing tracks is associated with the wrong vertex. For this, we remove events where the track of the primary scattered particle is also associated with the secondary vertex. Since the

---

[3] According to the Particle Data Group [13], the K_s^0 decays into $\pi^+\pi^-$ with a 69.20% probability, and into $\pi^0\pi^0$ with 30.69% probability. However, the latter is difficult to reconstruct in the spectrometer. Decays into other final states are rarer. In addition to the possible decays of the K_s^0, other V^0 candidates are e.g. Λ or $\bar{\Lambda}$ particles, which decay predominantly into $p\pi^-$ or $\bar{p}\pi^+$ respectively

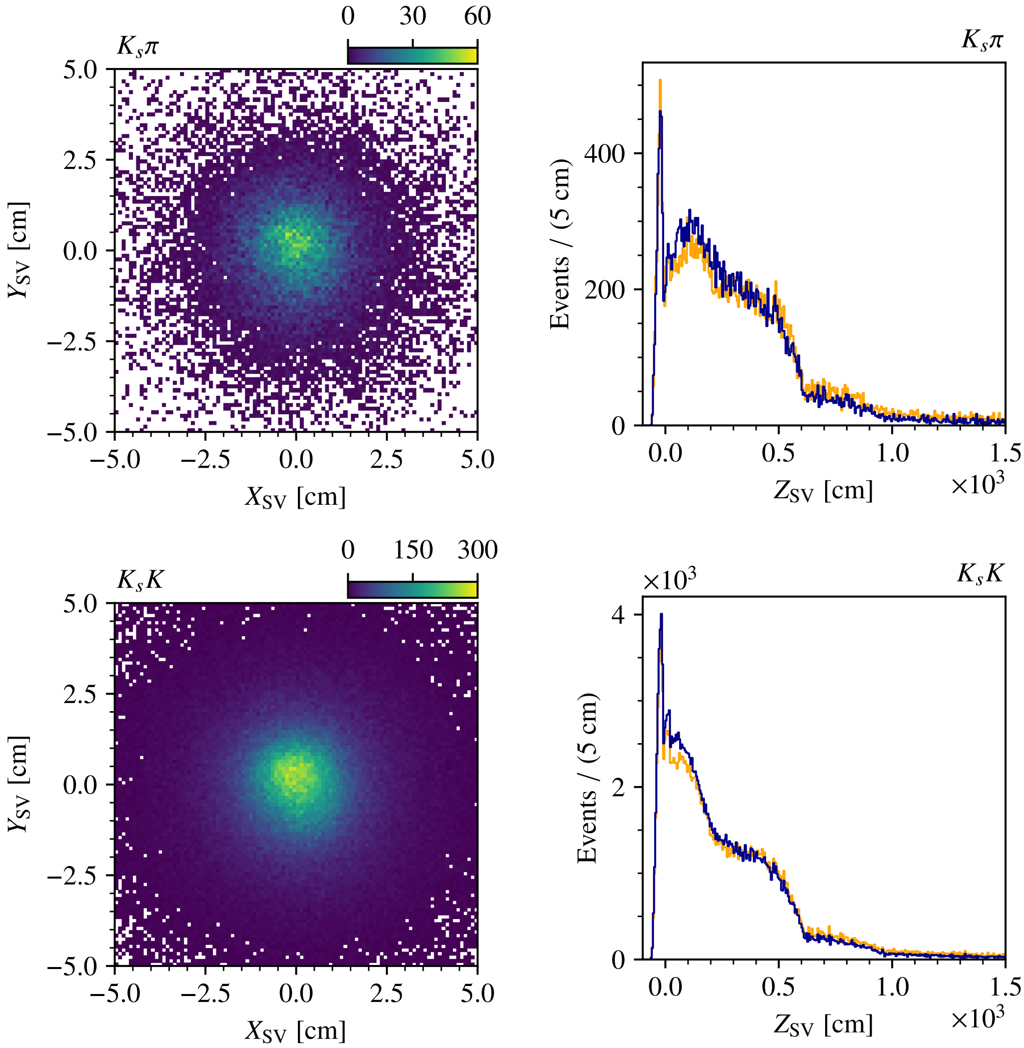

Figure 7.3: Distributions of the position of the secondary vertex for (top row) $K_s^0\pi^-$ and (bottom row) $K_s^0K^-$. The left plots show the radial position for the 2008 data and the right plots the axial position of the secondary vertices for the 2008 and 2009 data in both cases with all cuts applied.

primary vertex is required to have exactly only one negative track (see Section 7.1), this cut ensures the correct association of all final-state tracks to the secondary and primary vertices.

In order to ensure that the tracks of the secondary particles are correctly

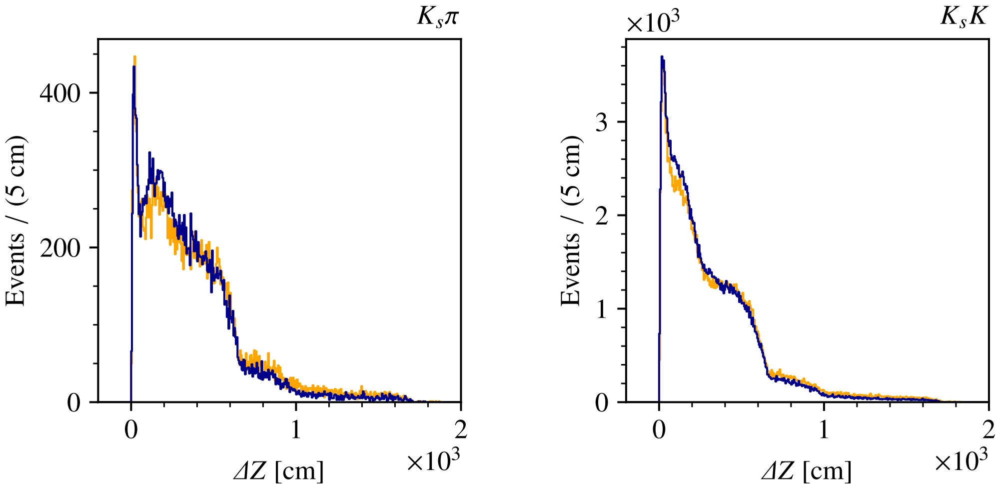

Figure 7.4: Distributions of the difference ΔZ of the Z-positions of the secondary and the primary vertex, for (left) $K_s^0\pi^-$ and (right) $K_s^0K^-$.

detected, we restrict the last measured position of the tracks along the Z-axis to be within $Z_{\text{last}} > 350$ cm.[4]

The momentum of the V^0 candidate should point from the primary to the secondary vertex. This means that the collinearity angle α_{coll}, which is the angle between the geometrical line from the primary to the secondary vertex and the direction of the V^0 momentum, should be approximately zero. We thus restrict α_{coll} to values smaller than 10 mrad $= 0.57$ deg. The distributions of the collinearity angle are shown in Fig. 7.5. There is a peak at very low angles, and only few events above approximately 0.1 deg. This confirms that the cut on the collinearity angle removes predominantly background or misreconstructed events.[5]

In the preselection, a first broad cut on the $\pi^-\pi^+$ mass of the reconstructed V^0 candidates was performed to reduce the number of events. In order to further reduce background, we make a narrower cut on the same variable. The distributions of the $\pi^-\pi^+$ mass are shown in Fig. 7.6. All distributions show a prominent K_s^0 peak with low background. The distribution from the

---

[4] This cut and its value have been taken from analysis of COMPASS muon-beam data [19, 20]. The cut is of a lesser importance in our data, which has a rather low background contamination (see Section 9.3). A possibility of improving this cut is discussed in Chapter 10.

[5] See Footnote 4.

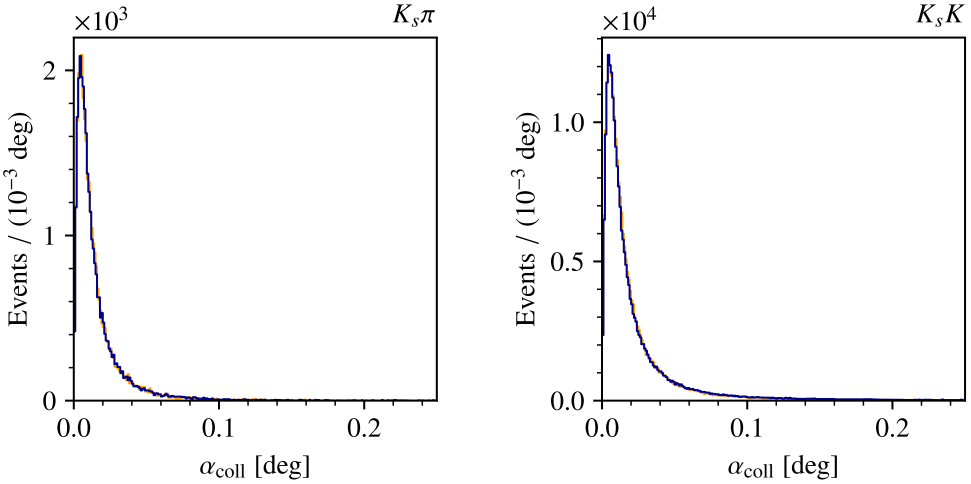

Figure 7.5: Distributions of the collinearity angle α_{coll} for (left) $K_s^0\pi^-$ and (right) $K_s^0K^-$. The cut value at 10 mrad = 0.57 deg is outside the plot range.

2009 dataset (orange) is slightly shifted towards lower K_s^0 masses. To select K_s^0 candidates, we fit the $m_{\pi\pi}$ distribution using a double Gaussian for the K_s^0 peak and a polynomial of second degree as background, equivalent to the function presented in Eq. (7.1). We then exclude events where the K_s^0 mass lies outside of the $3\,\sigma$ interval, i.e.

$$478.76 < m_{\pi\pi} < 517.96 \text{ MeV}/c^2 \text{ and } 478.70 < m_{\pi\pi} < 517.10 \text{ MeV}/c^2 \tag{7.6}$$

for the 2008 and 2009 datasets respectively. The fit result is shown by the red curves in Fig. 7.6.

Lastly, events remain which have more than one secondary vertex candidate after the selection. In this case, we cannot clearly assign the K_s^0 decay to any of the secondary vertices. These events could also stem from background reactions such as $K^- + p \to \pi^-\, K_s^0\, K_s^0 + p$. Such events are thus removed from the dataset, once all other cuts are applied. In 2008, only 1 event is removed by this cut from the $K_s^0\pi^-$ data, and only 11 events from the K_s^0K data. In 2009, no events are removed from the $K_s^0\pi^-$ dataset and only 2 events are removed from the $K_s^0K^-$ dataset. This shows that the other cuts in the event selection already eliminate the vast majority of such potential background events.

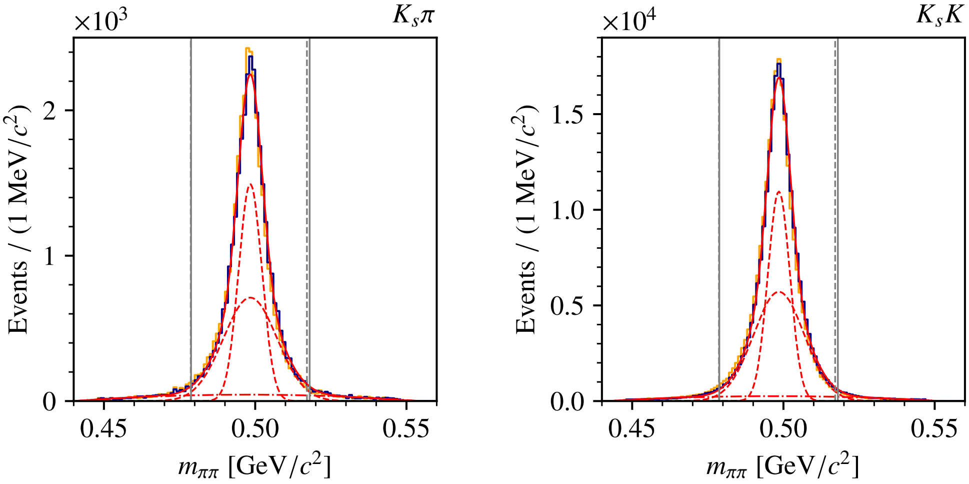

Figure 7.6: Mass distribution of the $\pi^-\pi^+$ pairs from the V^0 candidates, for $K_s^0\pi^-$ (left) and $K_s^0K^-$ (right). The cut values are indicated by gray vertical lines. The results of fitting Eq. (7.1) to the 2008 data are shown in red, with the overall fitted curve drawn as a solid line and its signal and background components as dashed lines.

7.2.4 Cuts on Energy and Momentum Conservation

In order to exclude events where some of the produced particles were not reconstructed, e.g. neutral particles such as π^0 or η, we apply cuts to ensure energy and momentum conservation between the initial and final state. In order to do this, first, the four-momentum of the intermediate state X^- is reconstructed from the detected final-state particles. The calculation of the V^0 four-momentum was explained in Section 7.2.3. We obtain the X^- four-momentum by summing the four-momenta of the V^0 and of the primary scattered particle.

We apply momentum conservation between the recoil proton and the X^- by verifying that both particles are emitted back-to-back in the plane transverse to the beam direction, i.e. the azimuthal angle ϕ_{recoil} between the two momenta must be equal to 180° within the angular resolution σ_ϕ of the RPD. This is done by enforcing

$$|\Delta\phi_{\text{recoil}}| = |180° - \phi_{\text{recoil}}| < \sigma_\phi \tag{7.7}$$

The azimuthal resolution of the RPD is either $\sigma_\phi = 8.432°$ or $5.377°$ depending on the hit pattern in the detector (see Ref. [18]). The $\Delta\phi_{\mathrm{recoil}}$ distribution for $K_s^0\pi^-$ and $K_s^0K^-$, respectively, are shown in Figs. 7.7 and 7.8.

Although the actual energy of the beam particle is not measured, we can still apply energy conservation by reconstructing the energy of the beam particle using the energy sum of the final-state particles. The distribution of the reconstructed beam energy is shown in Figs. 7.7 and 7.8 for $K_s^0\pi^-$ and $K_s^0K^-$ respectively. We also show the two-dimensional distributions of E_B versus $\Delta\phi_{\mathrm{recoil}}$ (only for 2008 data), in which a clear exclusivity peak at the nominal beam energy slightly above 190 GeV is visible. To select exclusive events, we extract the width of the exclusivity peak and reject events that lie outside the $3\,\sigma_E$ interval. The peak is modelled by a Gaussian. As the nonexclusive background is asymmetric around the peak, we describe it using the empirical function

$$f_{\mathrm{BG}}(E_B; a, b, c, d, E_0) = \frac{a}{|b| + c\,|(E_B - \mathrm{E}_0)^3| + |(E_B - \mathrm{E}_0)^2|} \cdot \left(\frac{\pi}{2} - \arctan\left(d\,(E_B - \mathrm{E}_0)\right)\right) \; . \tag{7.8}$$

We then fit the distribution with the sum of the Gaussian and the function in Eq. (7.8). This yields cut values of

$$186.48 < E_B < 196.20 \text{ GeV} \; .$$

7.2.5 Summary

The event selection yields a dataset of 57 216 $K_s^0\pi^-$ events (31 420 from the 2008 datataking and 25 796 from the 2009 datataking) and a dataset of 417 081 $K_s^0K^-$ events (227 835 from the 2008 datataking and 189 246 from the 2009 datataking). Fig. 7.9 summarizes the employed cuts for the event selections of the $K_s^0\pi^-$ and $K_s^0K^-$ final states. It also shows the number of secondary vertices remaining after each cut.

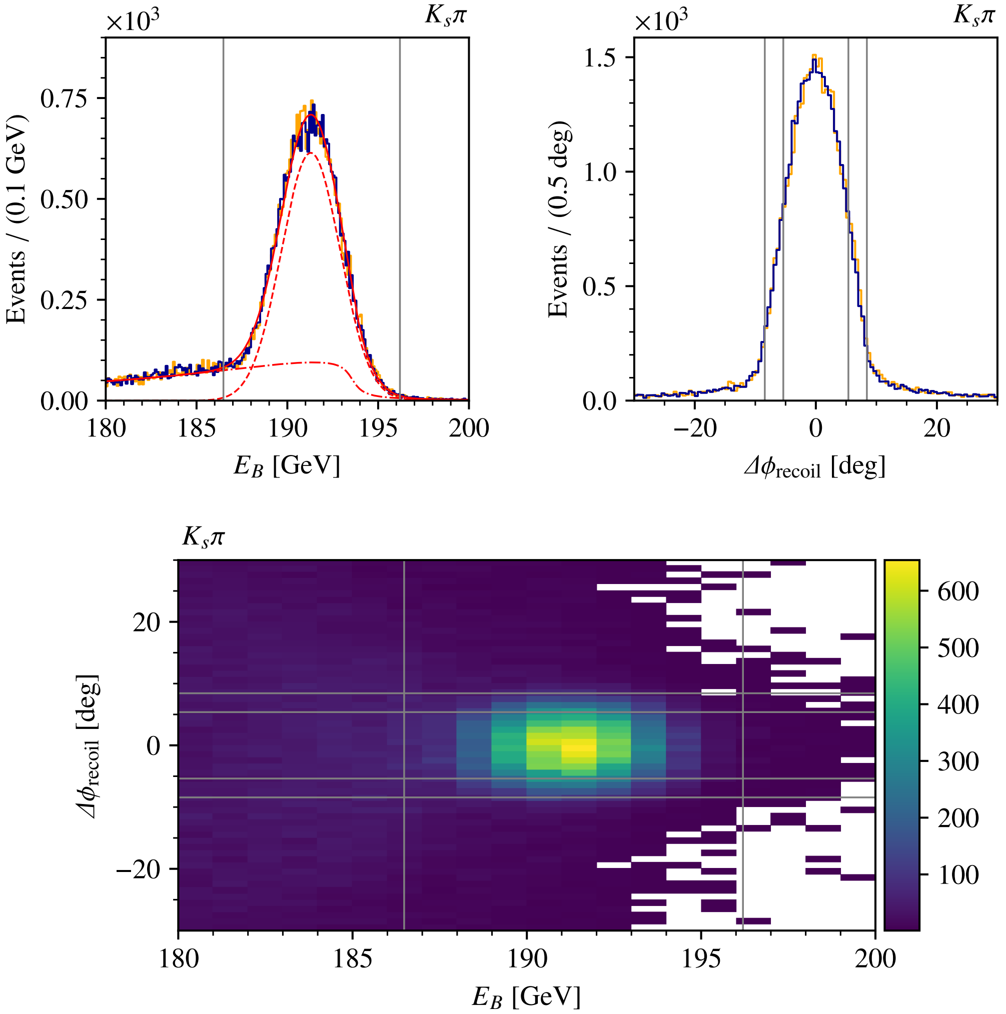

Figure 7.7: $K_s^0\pi^-$ distributions of (top left) the reconstructed beam energy E_B, and (top right) $\Delta\phi_{\mathrm{recoil}}$ (see text). The curve fitted on the 2008 beam energy distribution is drawn as a solid red line, its components are indicated by dashed lines. (Bottom) Two-dimensional distribution of $\Delta\phi_{\mathrm{recoil}}$ against E_B, for the 2008 $K_s^0\pi^-$ dataset. The cut ranges are indicated by gray lines.

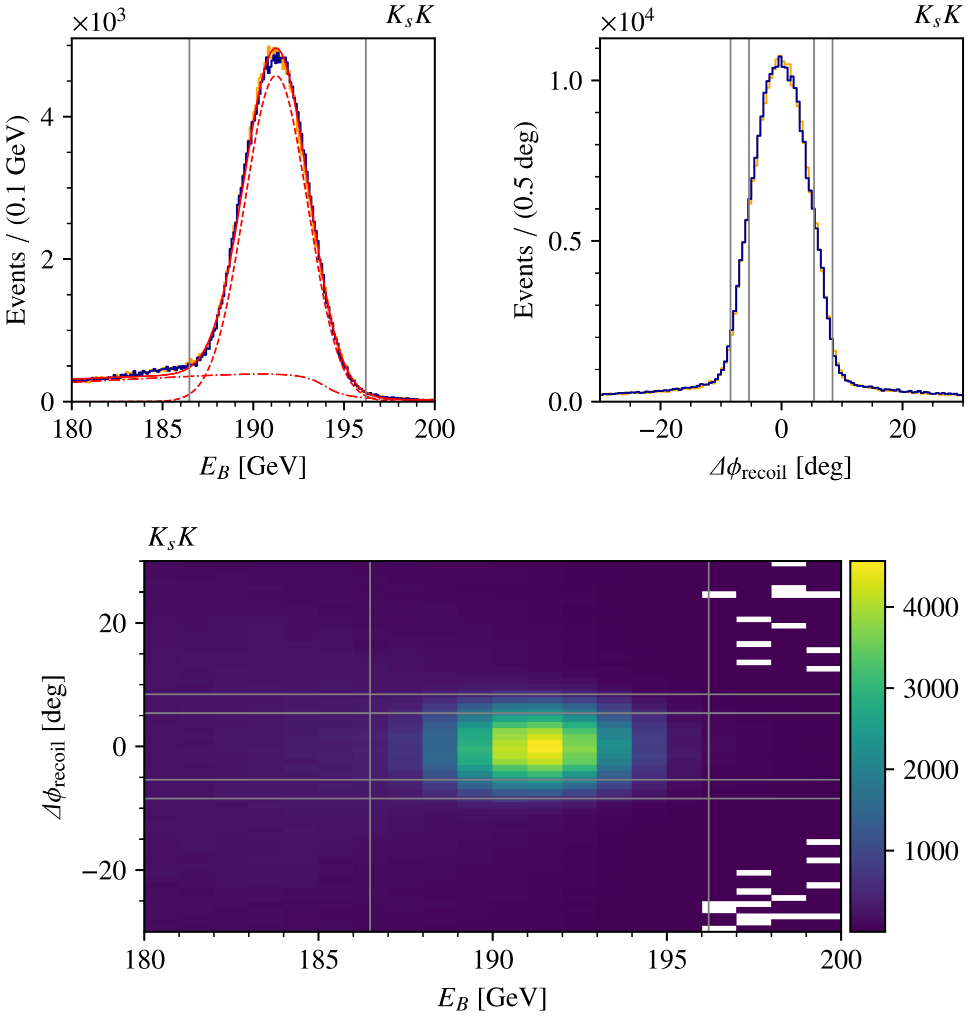

Figure 7.8: Same as Fig. 7.7, but for the $K_s^0K^-$ datasets.

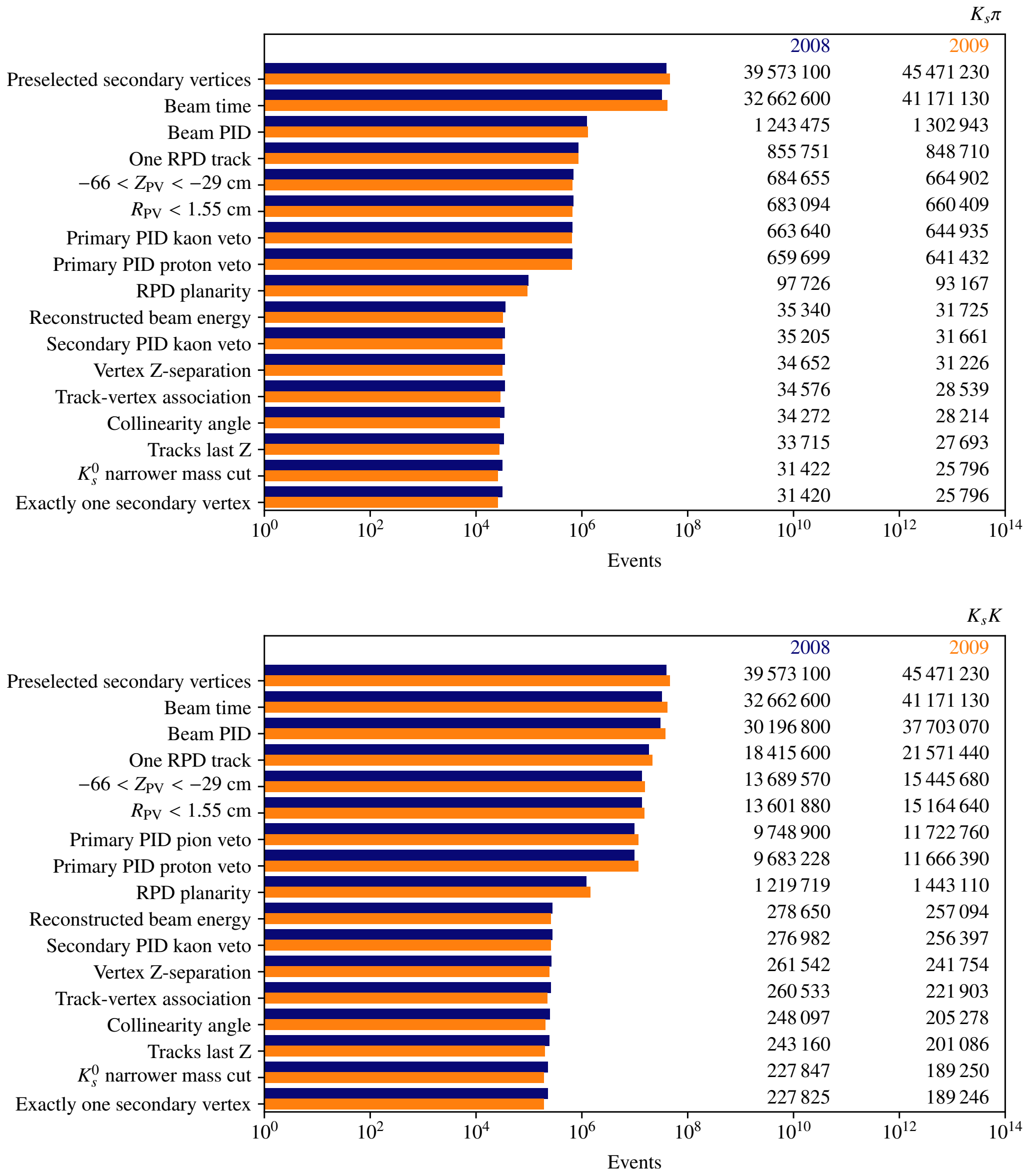

Figure 7.9: Summary of all used cuts and the corresponding number of secondary vertices for the event selections of (top) the $K_s^0\pi^-$ and (bottom) the $K_s^0K^-$ final state.

Chapter 8

Kinematic Distributions

Now that we have selected $K^- + p \to K_s^0\, \pi^- + p$ and $\pi^- + p \to K_s^0\, K^- + p$ events out of the 2008 and 2009 data, we can inspect various kinematic distributions of the data. We will study possible background contributions from other V^0 candidates, mass distributions of the $K_s^0\pi^-$ and $K_s^0K^-$ systems, the angular distributions, and the distribution of the reduced squared-momentum transfer t'. This will be done separately for the $K_s^0\pi^-$ and the $K_s^0K^-$ final states. The distributions are not acceptance-corrected, and might hence be distorted compared to the physical distributions. The acceptance will be studied in Chapter 9 using Monte Carlo methods, which will give us indications about the severity of these detector acceptance effects.

8.1 Kinematic Distributions of the $K_s^0\pi^-$ Final State

8.1.1 Contamination by Other V^0 Particles

First, we analyze the mass distributions that correspond to different candidates for the V^0 particle. In the studied reactions, signal events are events in which the V^0 is a K_s^0, but there can be background events in which the V^0 is e.g. a Λ or $\bar{\Lambda}$. As explained in Section 7.2.3, these three particles decay differently. However, the secondary particles are not strictly identified, as we only perform a RICH veto. We need to assume the masses of the secondary particles in which the V^0 decays in order to reconstruct the four-momentum of the V^0, and with this, the intermediate state. If the correct hypothesis is made, i.e. the correct secondary-particle masses are chosen for the V^0 in the event, its reconstructed mass should lie at its nominal mass. Taking into account the detector resolutions, a peak should form around the nominal V^0 mass. The mass distributions for the various V^0 hypotheses thus allow us to estimate the amount of V^0 particles of a given species in the data.

First, we study the mass distribution for the $\Lambda \to p\pi^-$ hypothesis. It is shown in the left plot of Fig. 8.1. Like in Chapter 7, we show the 2008

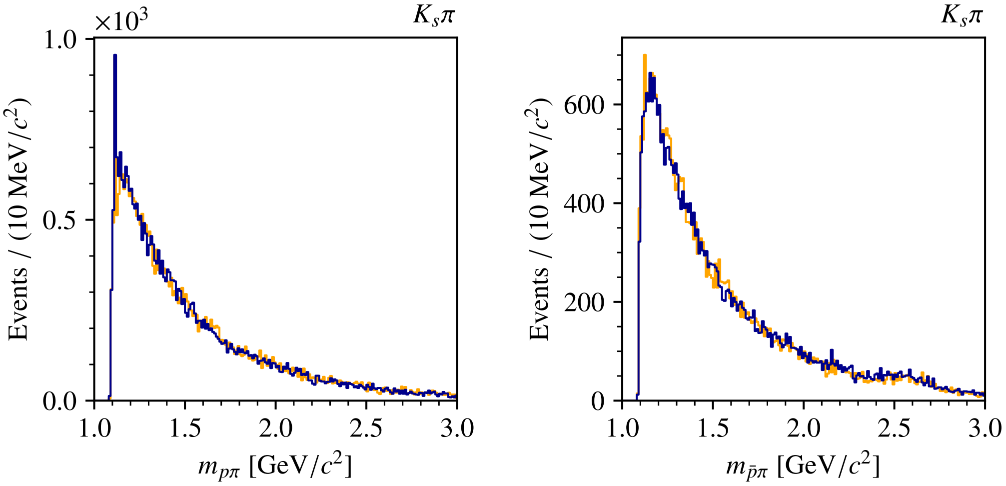

Figure 8.1: Distributions of (right) the reconstructed $\Lambda \to p\pi^-$ mass and (left) the reconstructed $\bar{\Lambda} \to \bar{p}\pi^+$ mass, both for the $K_s^0\pi^-$ final state. The distributions for the 2008 dataset are drawn in blue and the ones for the 2009 dataset in orange.

distribution and the scaled 2009 distribution in the same plot. They agree well. The $p\pi^-$ mass distribution exhibits a narrow peak at the nominal mass $m_\Lambda = 1.115$ MeV/c^2 of the Λ particle,on top of a large and smooth background.[1] This indicates that there are approx. 600 background events with Λ baryons as V^0 particles that remain after the event selection, but that the vast majority of V^0 particles are not Λs.

The same distributions for the $\bar{\Lambda} \to \bar{p}\pi^+$ hypothesis are shown in the right plot of Fig. 8.1. The distribution for the 2008 dataset does not exhibit a visible peak at m_Λ. In the 2009 dataset, a small peak can be seen around 1.1 GeV/c^2 which might contain approx. 100 $\bar{\Lambda}$ events, but might also simply stem from fluctuations in the data. Either way, the data does not contain a significant amount of background events in which the V^0 particle is a $\bar{\Lambda}$.

For the analyzed final states, the correct hypothesis is that the V^0 particle is a K_s^0 which decays into $\pi^-\pi^+$. We therefore expect the K_s^0 to be the dominant V^0 particle species in the selected data. This can be verified in the $\pi^-\pi^+$ mass distribution, which has already been shown in the left plot of Fig. 7.6. The distribution consists almost exclusively of a clear peak close to the nominal K_s^0

---

[1] The "background" in the $p\pi^-$ mass distribution corresponds to events where the mass-hypothesis is false, i.e. mostly K_s^0 events (which are the desired signal events), and is thus not to be confused with the actual background in our data.

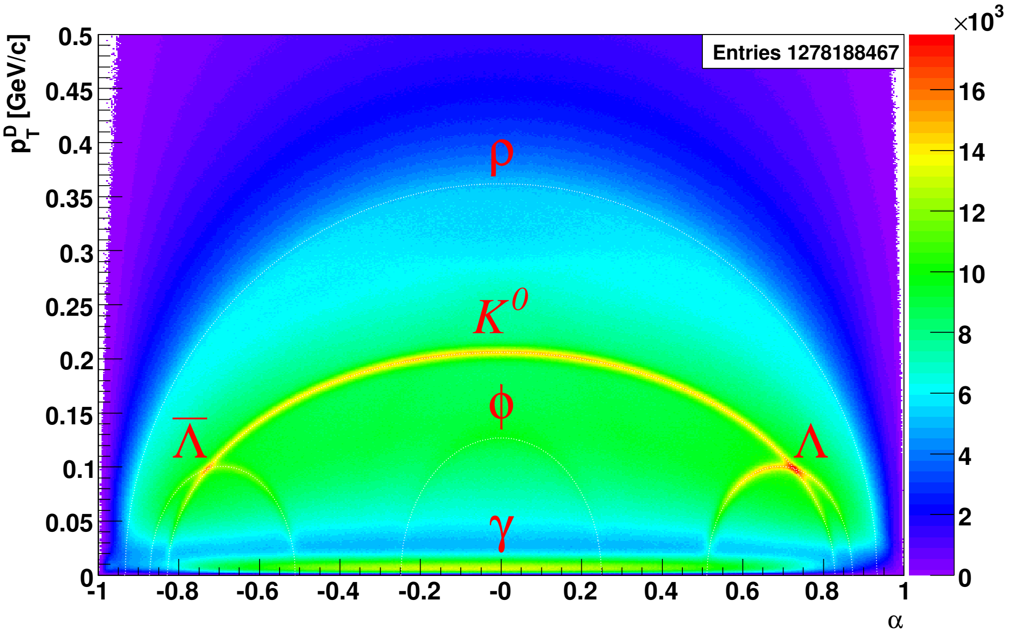

Figure 8.2: Example Armenteros plot, showing the bands of various V^0 particle species. From Ref. [21].

mass $m_{K^0} = 497.611$ MeV/c^2, with only very little background. This confirms that our event samples indeed contain an overwhelming majority of K_s^0 events. In order to extract the position and width of the peak, we fit a double Gaussian on top of a second-order polynomial background, equivalent to the function of Eq. (7.1), to our data, in the mass range $m_{K^0} \pm 50$ MeV/c^2. The curve in Fig. 7.6 shows the fit to the 2008 data. The peak is adequately modelled by the double Gaussian. The peak position lies at 498.4 MeV/c^2 for the 2008 $K_s^0\pi^-$ data, i.e. only 0.8 MeV/c^2 above the nominal K_s^0 mass. The distribution from the 2009 dataset is slightly shifted towards lower K_s^0 masses, with a fitted mean of 497.9 MeV/c^2, i.e. 0.3 MeV/c^2 above the nominal K_s^0 mass. Using Eq. (7.3), we calculate the total weighted width of the peak, which yields a value of $\sigma = 6.5$ MeV/c^2. This value essentially represents the resolution of the momentum reconstruction of the two secondary particles. The fit also gives us an indication on the amount of non-K_s^0 background in the distribution. Comparing the integrals of the signal and background components over the fit range yields a signal-to-background ratio of 9.1 for the 2008 data and 9.0 for the 2009 data.

Another way of estimating which V^0 particle species appear in the data is to inspect the so-called Armenteros or Armenteros-Podolanski plot [22], which shows the transverse momentum p_T of the V^0 decay versus the longitudinal-momentum asymmetry α of the decay. The former is the transverse momentum component of either daughter particle with respect to the V^0 direction of flight, while the latter is calculated from the longitudinal momentum components $p_L^\pm$ of the two daughter particles in the following way:

$$\alpha = \frac{p_L^+ - p_L^-}{p_L^+ + p_L^-} \ . \tag{8.1}$$

An example Armenteros plot from a different analysis [21] is shown in Fig. 8.2. Different V^0 particle species form bands in different areas of the plot, depending on how they decay. The particle species most interesting to us are $K_s^0 \to \pi^-\pi^+$, $\Lambda \to p\pi^-$ and $\bar{\Lambda} \to \bar{p}\pi^+$, and photons ($\gamma \to e^-e^+$). The latter cluster at low p_T, and can hence be clearly separated from the K_s^0 band, which is a wide and symmetric arc across α with a maximum p_T of about 0.2 GeV/c. The Λ and $\bar{\Lambda}$ form two smaller arcs at high positive and negative α, respectively. They overlap with the K_s^0 arc close to their maximum p_T of about 0.1 GeV/c. The arcs of the $\phi(1020)$ and $\rho(770)$ mesons shown in the plot are irrelevant here because - due to their extremely short lifetime - these mesons do not form secondary vertices in the detector. The Armenteros plot of the 2008 $K_s^0\pi^-$ data is shown in Fig. 8.3, with all cuts applied except the fine-selection cut on the reconstructed K_s^0 mass. We see that the mass cut applied in the preselection already removes the majority of non-K_s^0 events, essentially leaving only the area around the K_s^0 band intact. However, there can still be events containing Λ or $\bar{\Lambda}$ particles in the regions where the corresponding bands overlap with the K_s^0 band, as seen in the example plot in Fig. 8.2. A weak Λ arc overlapping with the K_s^0 arc can be discerned in Fig. 8.3 around $p_T = 0.1$ GeV/c and $\alpha = 0.75$. We do not see any increase of events in the area where the $\bar{\Lambda}$ band would be expected to appear. This confirms the findings from studying the $p\pi^-$ and $\bar{p}\pi^+$ mass distributions: Our $K_s^0\pi^-$ data sample contains some rare events with Λ as V^0 particles, but the majority of events contain K_s^0 particles as expected.

8.1.2 $K_s^0\pi^-$ Mass Distribution

We can gain first insights into the resonances contained in the $K_s^0\pi^-$ data sample by studying the distribution of the invariant $K_s^0\pi^-$ mass. Figure 8.4 shows the 2008 and 2009 distributions overlaid, which agree well. The distributions exhibit two prominent peaks around 900 and 1400 MeV/c^2. The first peak can be assigned to the well-known $K^*(892)$ resonance, while the second one corresponds to the $K_2^*(1430)$ resonance. This assignment is confirmed by studying the angular distributions of the data in Section 8.1.3. At about 1.8 GeV/c^2, we also see a slight increase in intensity which may be caused by the $K_3^*(1780)$ resonance. A partial-wave analysis of the data is required to further uncover the resonance content of the data, especially around and above 1.8 GeV/c^2.

The reaction $K^\pm + p \to K_s^0\pi^\pm + p$ has already been studied by W.E. Cleland et al. in 1982 [4] at CERN using beam momenta of 50 GeV/c. Except for the lower beam momentum, the reaction is exactly the same as the one studied in this thesis. In Ref. [4], they have studied $K_s^0\pi^\pm$ production as a function of $m_{K_s\pi}$ and t' using a dataset of 34 000 events. We thus possess a dataset that is roughly two times larger. While we have an overall lower acceptance (which will be seen in Section 9.1), the dependence of the acceptance in $m_{K_s\pi}$ is similar in both analyses, so that the distributions should be comparable. The $K_s^0\pi^-$ mass distribution from Ref. [4] is shown in Fig. 8.5 and looks very similar to Fig. 8.4. The two peaks corresponding to the $K^*(892)$ and the $K_2^*(1430)$ are also prominently present. In our distribution, the $K_2^*(1430)$ peak seems slightly more pronounced, which might be due to our higher beam momentum. Cleland et al. have also performed a PWA of the data. We have the same assignment

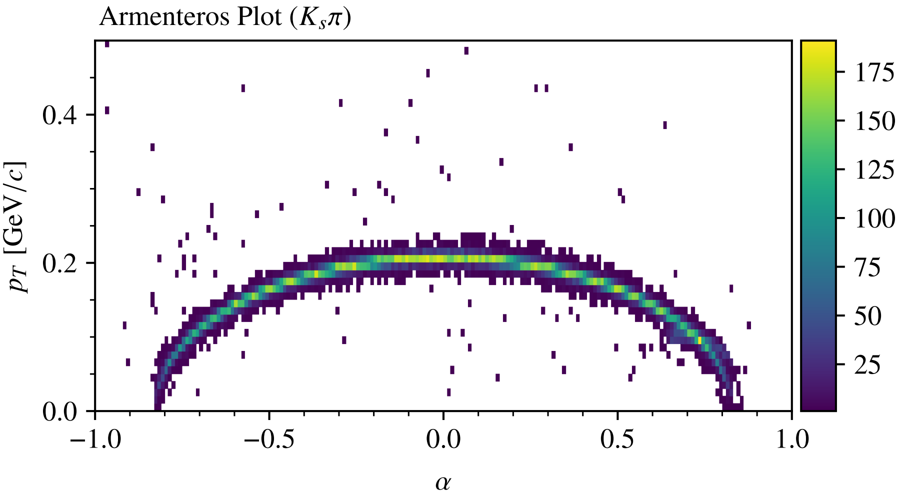

Figure 8.3: Armenteros plot of the 2008 $K_s^0\pi^-$ dataset, plotted without the fine-selection K_s^0 mass cut (see Section 7.2.3).

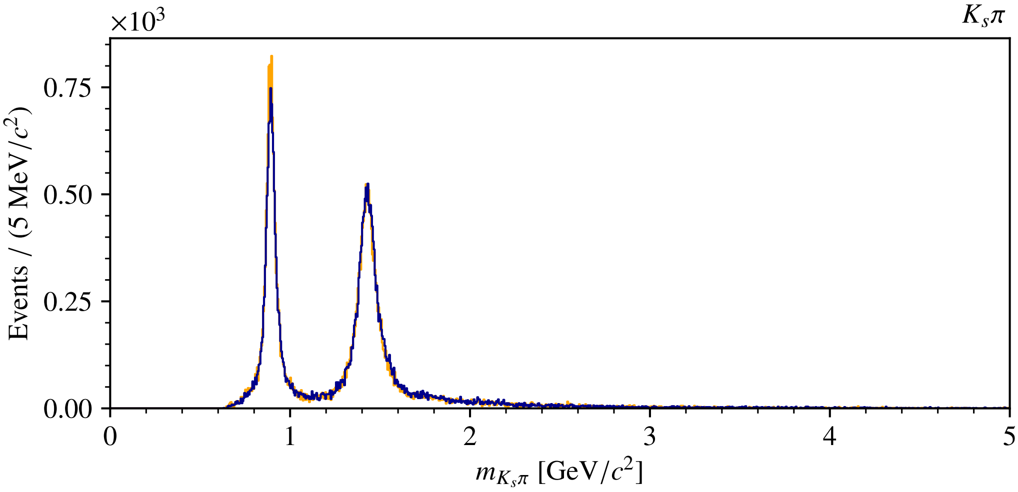

Figure 8.4: Distribution of the $K_s^0\pi^-$ mass. The distribution for the 2008 dataset is drawn in blue and the one for the 2009 dataset in orange.

of resonances as them. In their mass distribution and the PWA, they also identify the $K_3^*(1780)$ and the $K_4^*(2045)$. While in our mass distribution, the latter is not clearly visible, we observe an increase of events at approximately 1.8 GeV/c^2, which could be interpreted as the $K_3^*(1780)$. Overall, our findings are compatible with the analysis of Ref. [4].

8.1.3 Angular Distributions

As explained in Section 3.2.2, the angular dependence of the decay amplitude for a resonance decaying into two spinless particles is given by the spherical harmonics Y_J^M, with J being the total spin of the resonance[2] and M its projection. In our case, the two angles θ_{GJ} and ϕ_{GJ} describing the decay are defined in the Gottfried-Jackson frame, described in Section 3.2.5. More precisely, the distribution of the amplitudes in $\cos\theta_{\mathrm{GJ}}$ is given by the associated Legendre polynomials $P_J^M(\cos\theta_{\mathrm{GJ}})$, and the dependence on ϕ_{GJ} is given by $e^{iM\phi_{\mathrm{GJ}}}$. As mentioned in Section 3.3.3, we introduce an additional quantum number, the reflectivity ε, and describe the quantum numbers in the reflectivity basis, where $M \geq 0$ and $\varepsilon = \pm 1$. We can split the spherical harmonics into their positive-

---

[2] $J = L$ for two spinless final-state particles

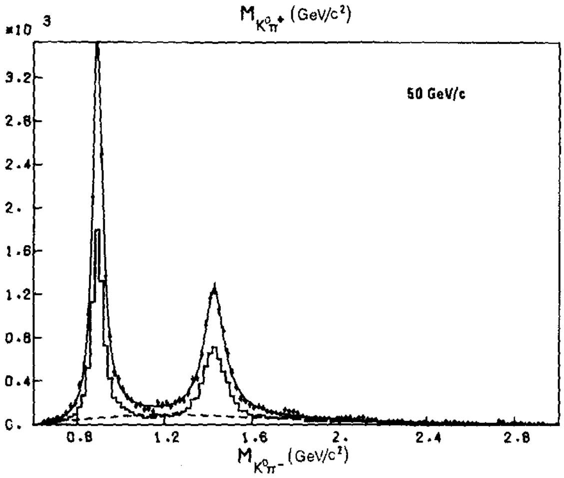

Figure 8.5: $K_s^0\pi^-$ mass distribution from the analysis of Cleland et al. for $0.05 \leq -t \leq 1$ $(\mathrm{GeV}/c)^2$. Histogram: Measured, non-acceptance corrected distribution (c.f. Fig. 8.4). Points with error bars: Acceptance-corrected distribution. The curves correspond to a fit to the data. From Ref. [4].

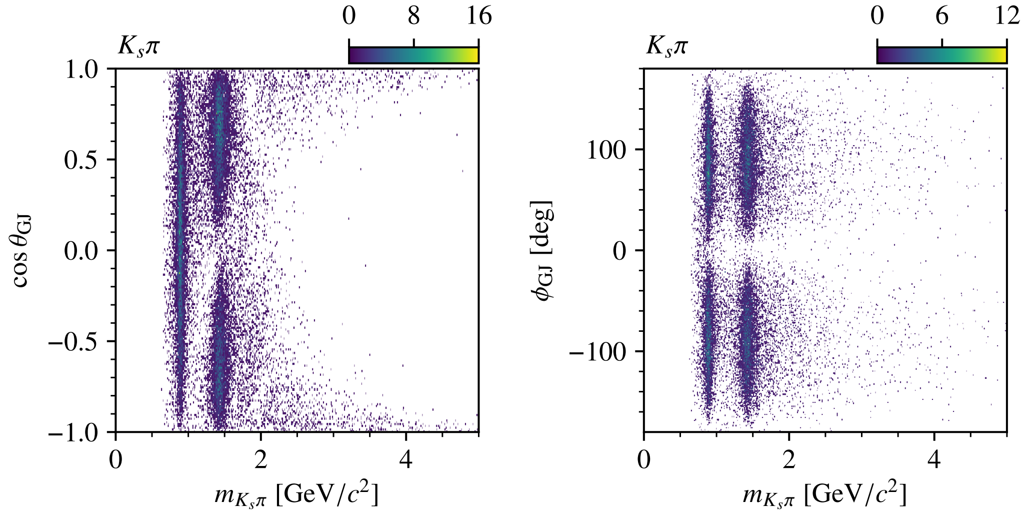

Figure 8.6: Distributions of (left) $\cos\theta_{\mathrm{GJ}}$ and (right) ϕ_{GJ} versus $m_{K_s\pi}$ for the 2008 $K_s^0\pi^-$ dataset.

and negative-reflectivity components [23]:

$$Y_J^{M,\varepsilon=+1}\left(\theta_{\mathrm{GJ}},\phi_{\mathrm{GJ}}\right) \propto i\sin\left(M\phi_{\mathrm{GJ}}\right) Y_J^M\left(\theta_{\mathrm{GJ}},0\right) \tag{8.2}$$

$$Y_J^{M,\varepsilon=-1}\left(\theta_{\mathrm{GJ}},\phi_{\mathrm{GJ}}\right) \propto \cos\left(M\phi_{\mathrm{GJ}}\right) Y_J^M\left(\theta_{\mathrm{GJ}},0\right). \tag{8.3}$$

This means that states with different reflectivities exhibit a different dependence on ϕ_{GJ}. However, at high beam energies, negative reflectivities are suppressed in diffractive scattering reactions such as $K^- + p \to K_s^0\pi^- + p$ (see Section 3.3.3), so that we expect the ϕ_{GJ} distributions to follow a $\sin\left(M\phi_{\mathrm{GJ}}\right)$ behavior.

Information about the spin projection M of the state along the beam direction can be extracted from the ϕ_{GJ}-dependence. We show the distribution of ϕ_{GJ} versus $m_{K_s^0\pi}$ in the right plot of Fig. 8.6. We observe a strong modulation in ϕ_{GJ} at the masses of the two resonance peaks. The angular distribution follows a $\sin^2\phi_{\mathrm{GJ}}$ distribution, which indicates that both states have $M = 1$. The distribution of $\cos\theta_{\mathrm{GJ}}$ against the $K_s^0\pi^-$ mass is shown for the 2008 dataset in the left plot of Fig. 8.6. We observe a clear modulation of the $\cos\theta_{\mathrm{GJ}}$ distribution in the mass regions of the two resonance peaks seen in Fig. 8.4. For $J = 1$, $|Y_1^1|^2 \propto |P_1^1|^2 \propto 1 - \cos^2\theta_{\mathrm{GJ}}$ has one maximum at $\cos\theta_{\mathrm{GJ}} = 0$, which is what we observe around 900 MeV/c^2. This confirms the presence of the $K^*(892)$ resonance. For $J = 2$, e.g. $|Y_1^2|^2 \propto |P_2^2|^2 \propto \cos^2\theta_{\mathrm{GJ}} - \cos^4\theta_{\mathrm{GJ}}$ has two maxima at $\cos\theta_{\mathrm{GJ}} \approx \pm 0.7$. The two maxima at about 1.4 GeV/c^2 hence confirm our hypothesis posed in Section 8.1.3 that the second resonant peak in the $K_s^0\pi^-$ mass distribution belongs to the $K_2^*(1430)$ with $J = 2$. No clear angular structure stemming from a further resonance can be seen outside of the two resonance peaks. However, we observe some patterns from background processes at high $m_{K_s\pi} > 2.5$ GeV/c^2 and $\cos\theta_{\mathrm{GJ}} \approx \pm 1$, the so-called "forward/backward peaking" also seen in Ref. [24].

8.1.4 Distribution of Squared Four-Momentum Transfer

The reduced four-momentum transfer squared t' between beam particle and the X^- is defined in Eq. (3.6). Figure 8.7 shows the t' distribution of the 2008 and 2009 $K_s^0\pi$ data in logarithmic scale, which agree well. Above about 0.1 (GeV/c)^2, we expect an approximately exponentially falling distribution, which indeed is case for both years. We extract the slope of the distribution by fitting an exponential function to the distribution between $0.2 < t' < 1.0$ (GeV/c)^2. This yields a slope of -5.4 (GeV/c)$^{-2}$.

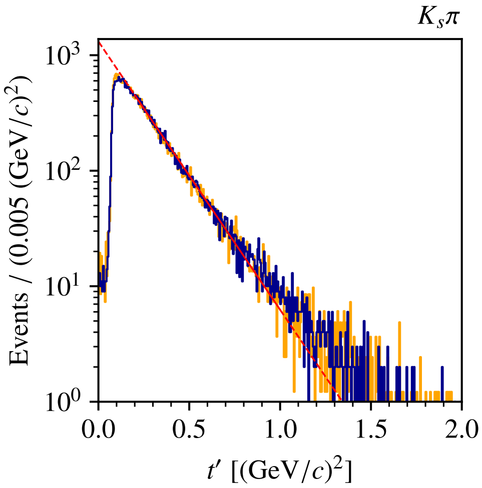

Figure 8.7: t' distributions of the 2008 (blue) and 2009 (orange) $K_s^0\pi^-$ data in logarithmic scale. The result of fitting an exponential to the 2008 distribution is drawn in red, with the extrapolated curve outside the fit range as a dashed line.

8.2 Kinematic Distributions of the $K_s^0 K^-$ Final State

8.2.1 Contamination by Other V^0 Particles

In a a similar fashion to Section 8.1.1, we study the mass distributions of various V^0 particles, i.e. Λ, $\bar{\Lambda}$, and K_s^0, for the $K_s^0 K^-$ final state.

The distributions of the reconstructed $\Lambda \to p\pi^-$ and $\bar{\Lambda} \to \bar{p}\pi^+$ masses are shown in Fig. 8.8. Slight deviations in the 1.2 GeV/c^2 region between 2008 and 2009 are yet to be understood. Here, in contrary to the distributions of the $K_s^0\pi^-$ final state (see Fig. 8.1), no peaks at the nominal Λ mass of $m_\Lambda = 1.115$ MeV/c^2 are observed. This suggests that the background from Λ and $\bar{\Lambda}$ events is negligible in the $K_s^0 K^-$ data.

The distribution of the reconstructed $K_s^0 \to \pi^-\pi^+$ mass has already been shown in the right plot of Fig. 7.6. Just as for $K_s^0\pi^-$, the distribution features a prominent peak at the nominal K_s^0 mass of $m_{K^0} = 497.611$ MeV/c^2. Again, we fit the distribution using the same function as in Section 8.1.1 to extract position and width of the peak. The peak lies at 498.5 MeV/c^2 for 2008 data and at 498.0 MeV/c^2 for 2009 data, i.e. 0.9 and 0.4 MeV/c^2 above the nominal K_s^0 mass. Both peaks are thus very close to the m_{K_s}, but, again, the 2009 distribution is nearer. The width of the distribution is estimated to $\sigma =$ 6.3 MeV/c^2, i.e. a little narrower than for the $K_s^0\pi^-$ final state. The amount of

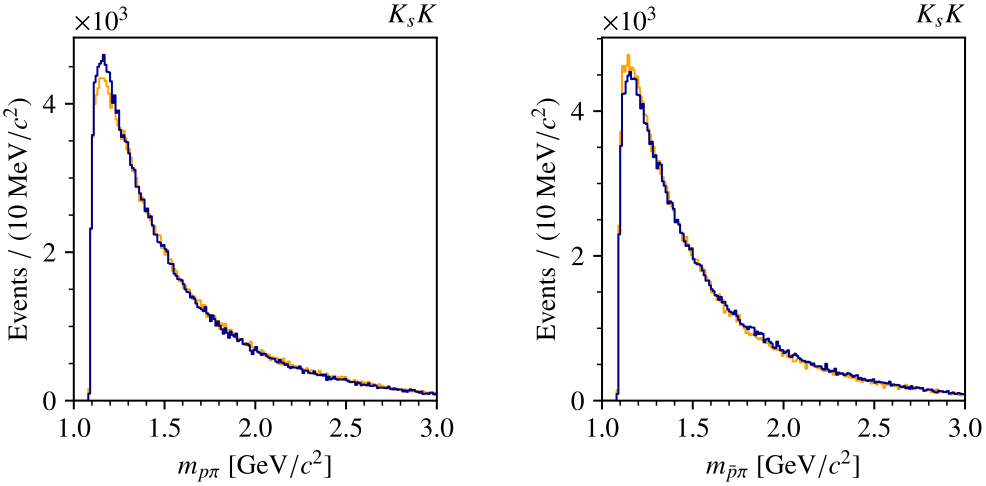

Figure 8.8: Distributions of (left) the reconstructed $\Lambda \to p\pi^-$ mass and (right) the reconstructed $\bar{\Lambda} \to \bar{p}\pi^+$ mass for the $K_s^0K^-$ final state. The distributions for the 2008 dataset are drawn in blue and the distributions from the 2009 dataset in orange.

background below the K_s^0 peak is minimal, with a signal-to-background ratio of 11.63 for the 2008 data and even increasing to 12.17 for the 2009 data, which is about 25% higher than for $K_s^0\pi^-$.

Lastly, we can study the Armenteros plot of the $K_s^0K^-$ final state, shown for the 2008 dataset in Fig. 8.9. Similarly to the plot for $K_s^0\pi^-$ in Fig. 8.3, we observe a clear band corresponding to the K_s^0. However, no overlapping of other V^0 bands is observed. As the total number of events in the $K_s^0K^-$ dataset is higher than in the $K_s^0\pi^-$ dataset, we observe also more background events around the K_s^0 band. These may e.g. be events with misreconstructed K_s^0, and are removed by the final cut on $m_{\pi\pi}$.

These observations are consistent with our findings from studying the reconstructed $K_s^0 \to \pi^-\pi^+$, $\Lambda \to p\pi^-$ and $\bar{\Lambda} \to \bar{p}\pi^+$ mass distributions. The selected $K_s^0K^-$ event sample seems to consist almost exclusively of events in which the V^0 particle is indeed a K_s^0, with no or only very little contamination by Λ or $\bar{\Lambda}$.

8.2.2 $K_s^0K^-$ Mass Distribution

In order to gain information about the intermediate states X^- produced in the reaction $\pi^- + p \to K_s^0K^- + p$, we study the distribution of the $K_s^0K^-$ mass,

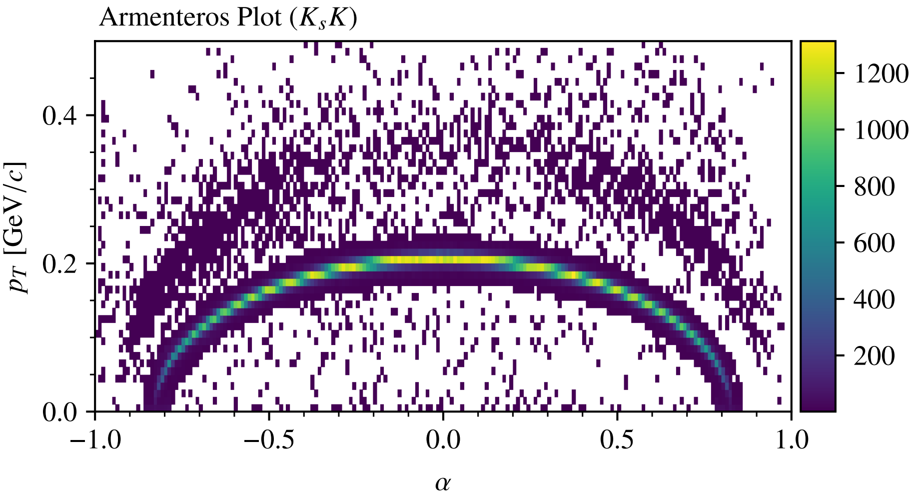

Figure 8.9: Armenteros plot of the 2008 $K_s^0K^-$ dataset, plotted without the fine-selection K_s^0 mass cut (see Section 7.2.3).

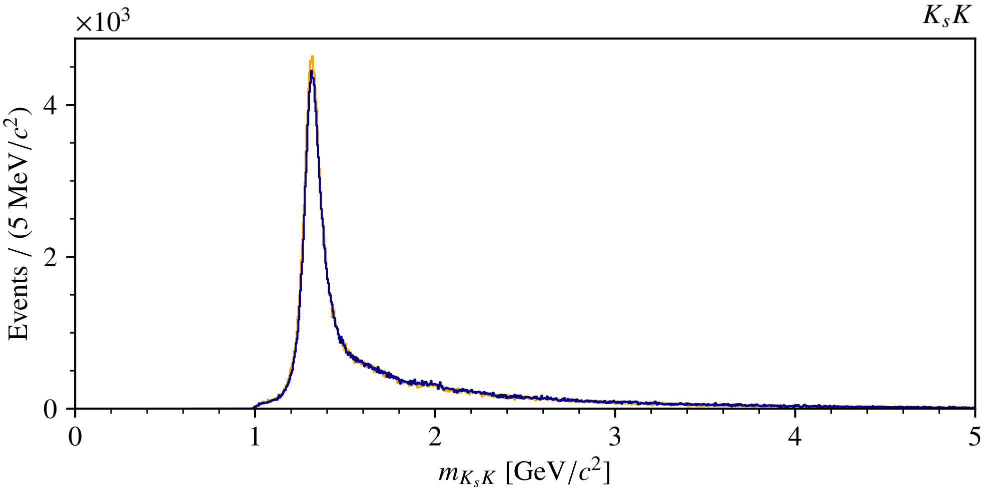

Figure 8.10: Distributions of the $K_s^0K^-$ mass. The distribution for the 2008 dataset is drawn in blue and the distribution from the 2009 dataset in orange.

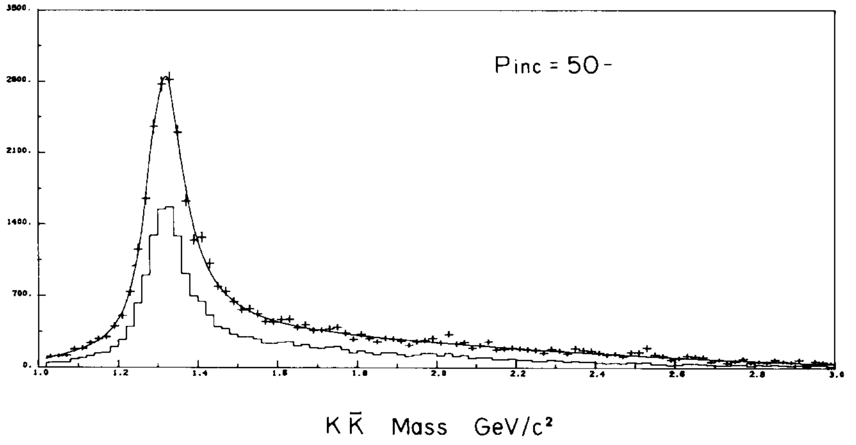

Figure 8.11: $K_s^0 K^-$ mass distribution from the analysis of Cleland et al. Histogram: Measured, non-acceptance corrected distribution (c.f. to Fig. 8.10). Points with error bars: Acceptance-corrected distribution. The curve corresponds to a fit to the data. From Ref. [5].

which is shown in Fig. 8.10. A prominent peak at 1.3 GeV/c^2, associated to the well-known $a_2(1320)$ resonance, dominates the distribution. A slight increase in intensity can also be seen at approximately 2 GeV/c^2, which could be due to the well-known $a_4(1970)$. Overall, no clear signals from higher-mass resonances can be seen in the distribution, and their presence would thus have to be established via partial-wave analysis.

In Ref. [5], Cleland et al. have also analyzed the $\pi^- + p \to K_s^0 K^\pm + p$ final state using the same experimental setup as in Ref. [4]. Again, except for the lower beam momentum, the process studied there is exactly the same as the one examined in this thesis. In comparison to their analyzed dataset of 40 000 $K_s^0 K^-$ events, we have acquired a dataset that is roughly 10 times larger. As was the case in $K_s^0 \pi^-$, we have a lower overall acceptance, but the dependence of the acceptance on $m_{K_s^0 K}$ is slightly weaker. The $K_s^0 K^-$ mass distribution from Ref. [5] is shown in Fig. 8.11. They observe a similar dominance of the $a_2(1320)$. Cleland et al. also report the clear presence of an $a_4(1970)$ resonance [formerly known as $a_4(2040)$] in their data, as well as minor contributions from the $\rho'(1600)$ and $\rho_3(1690)$. They also find evidence for an a_6 resonance at 2450 MeV/c^2. We can possibly make out the $a_4(1970)$ in our data as a slight enhancement in the mass distribution around 2 GeV/c^2. The $\rho(1700)$, $\rho'(1600)$, and the a_6 cannot be seen directly in our $m_{K_s K}$ distribution

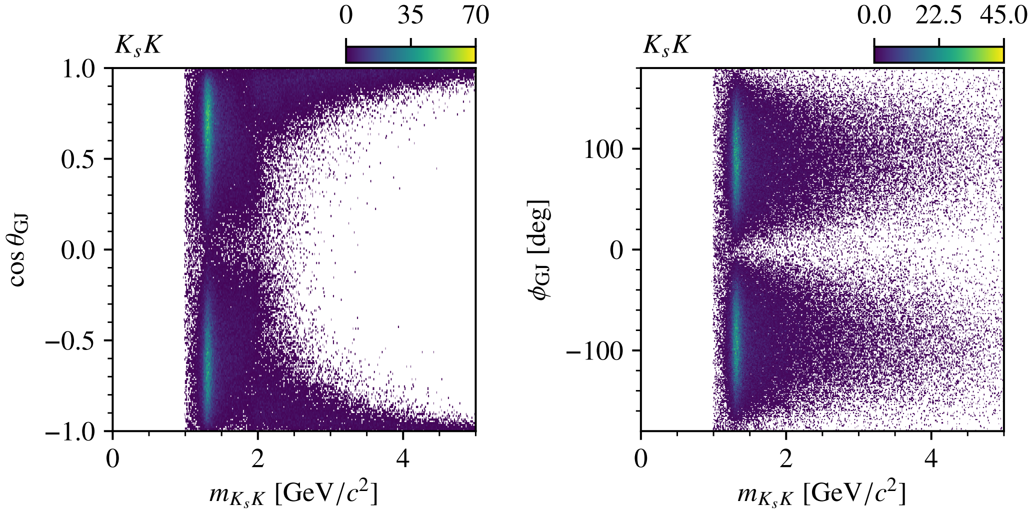

Figure 8.12: Distributions of (left) $\cos\theta_{\mathrm{GJ}}$ and (right) ϕ_{GJ} versus $m_{K_s^0K}$ for the 2008 $K_s^0K^-$ dataset.

in Fig. 8.10, but they are also invisible in Fig. 8.11. As far as our analysis of the $K_s^0K^-$ channel goes, our findings are in good agreement with those of Ref. [5].

8.2.3 Angular Distributions

As described in Section 8.1.3, we again deduce information about the quantum numbers of the resonances by inspecting the angular distribution of the $K_s^0K^-$ system. Similar to $K_s^0\pi^-$, the $\sin^2\phi_{\mathrm{GJ}}$ dependence of the ϕ_{GJ} distribution in the right plot of Fig. 8.12, indicates that the produced intermediate states have predominantly a spin projection of $M = 1$ w.r.t. the beam direction. The distribution of $\cos\theta_{\mathrm{GJ}}$ versus the $K_s^0K^-$ invariant mass is shown in the right plot of Fig. 8.12 for the 2008 dataset. The dependence of the distribution on $\cos\theta_{\mathrm{GJ}}$ around the mass peak at 1.3 GeV/c^2 indicates that the resonance there has total spin $J = 2$, which is consistent with our $a_2(1320)$ hypothesis. Around 2 GeV/c^2, we also observe interference effects and a faint four-peak structure in the $\cos\theta_{\mathrm{GJ}}$ distribution, likely stemming from the $a_4(1970)$ resonance. At even higher mass, we observe the same background effects as in $K_s^0\pi^-$.

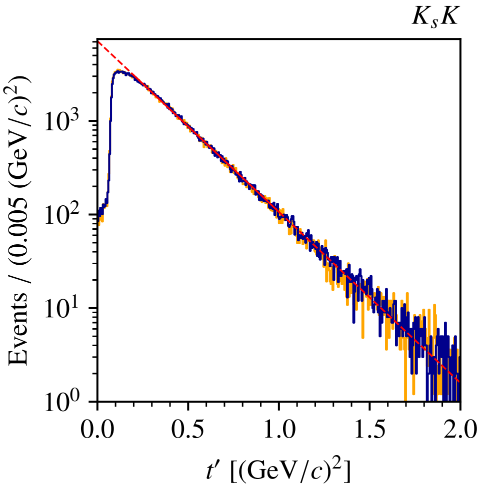

Figure 8.13: t' distributions of the 2008 (blue) and 2009 (orange) $K_s^0K^-$ data in logarithmic scale. The result of fitting an exponential to the 2008 distribution is drawn in red, with the extrapolated curve outside the fit range as a dashed line.

8.2.4 Distribution of Squared Four-Momentum Transfer

The t' distribution of the $K_s^0K^-$ data is shown in Fig. 8.13. It looks similar to the distribution for $K_s^0\pi^-$, and is decreasing exponentially, as expected. We extract the slope of the distribution by fitting an exponential function to the distribution between $0.2 < t' < 1.0$ (GeV/c)^2. This yields a slope of -4.2 (GeV/c)$^{-2}$.

Chapter 9

Monte Carlo Acceptance And Resolution Studies

In this section, we will present our studies on the phase-space acceptances and resolutions for the $K_s^0\pi^-$ and $K_s^0K^-$ final states. For each channel, we start by generating 10^7 Monte Carlo events which are distributed isotropically in phase space. These events are then processed through the detector simulation, the event reconstruction, and event selection. We thus obtain a MC dataset that is weighted by the acceptance and smeared by resolution effects. As the kinematic distributions of the generated MC data are known, we can estimate the extent of those effects. First, the acceptance will be studied in Section 9.1, before inspecting the experimental resolution for some kinematic variables in Section 9.2. We also study possible backgrounds from other processes in Section 9.3.

9.1 Acceptance of the $K_s^0\pi^-$ and $K_s^0K^-$ Channels

We use the term acceptance to refer to all effects leading to loss of events, from the finite efficiency of the detectors to the rejection of events during the event selection. As explained in Section 3.4, we can estimate these effects as a function of any kinematic variable by comparing the distributions of the accepted and generated MC data. This yields an approximation of the phase-space acceptance, which may be different from the real acceptance. There are two different possibilities for the calculation of the acceptance: for each accepted event, we can either use the reconstructed values of the variables, or the Monte Carlo truth (MCT) values, i.e. the values with which the event was generated. The former includes resolution effects from the measurement process, which will be studied separately in the next Section 9.2. We choose to use the latter definition of the acceptance, i.e. we divide the MCT distribution of the accepted events by the MCT distribution of the generated events, thereby separating detection efficiency from resolution effects. The acceptances for the $K_s^0\pi^-$ and

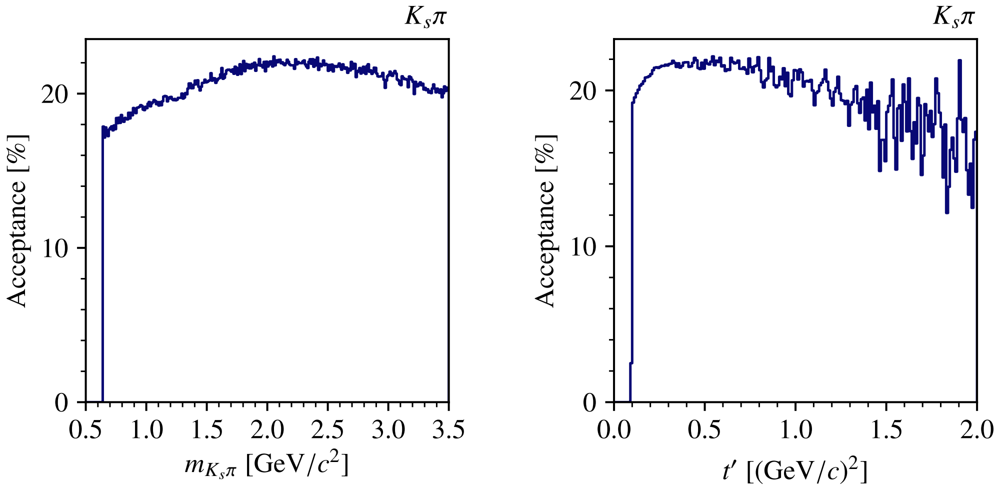

Figure 9.1: Acceptance as a function of (left) the $K_s^0\pi^-$ mass and (right) t', both for the $K_s^0\pi^-$ final state.

$K_s^0K^-$ final states are similar. They will thus be discussed together, although we show here only the distributions for the $K_s^0\pi^-$ final state. The corresponding distributions for the $K_s^0K^-$ final state can be found in Appendix B.1.

First, the overall acceptance can be calculated by dividing the number of accepted MC events to the number of generated MC events. This yields an average acceptance of 20.8% for the $K_s^0\pi^-$ final state and of 25.0% for the $K_s^0K^-$ final state. However, as exemplified by the PWA of the $K^-K^+\pi^-$ channel in Part I, the value of the overall acceptance is of lesser importance. What matters more for the PWA is that the acceptance is only weakly modulated in the phase-space variables. As we will show in this section, that is the case.

We start by discussing the acceptance as a function of the $K_S^0\pi^-$ mass as shown in the left plot of Fig. 9.1. We have started generating MC data at 0.64 GeV/c^2. The acceptance is quite uniform over the entire mass range, decreasing by a few percents at low and high masses. The corresponding acceptance for the $K_S^0K^-$ final state looks similar (see Fig. B.1 left).

Before coming to the angular distributions, we inspect the acceptance as a function of the reduced squared four-momentum transfer t', shown in the right plot of Fig. 9.1. We have generated MC data non-uniformly in the interval $0.1 < t' < 3.0$ (GeV/c)^2. Between 0.1 and 1.0 (GeV/c)^2, the acceptance is

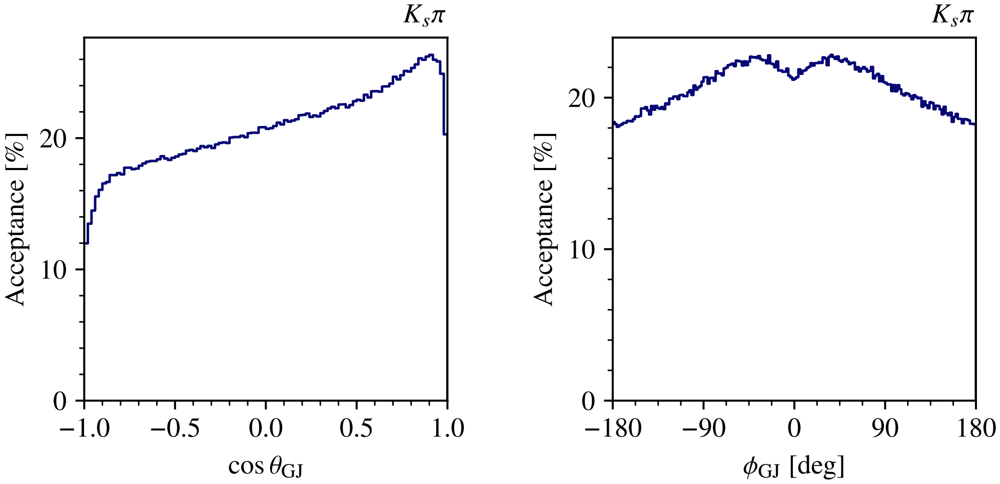

Figure 9.2: Acceptance as a function of (left) $\cos\theta_{\mathrm{GJ}}$ and (right) ϕ_{GJ}, both for the $K_s^0\pi^-$ final state.

quite stable slightly above 20%, and then starts to decline slowly for $t' > 1.0\ (\mathrm{GeV}/c)^2$.

When searching for resonances by performing an angular analysis of the data (such as a PWA), it is of great importance that the acceptance is as uniform as possible in the decay angles. We therefore study the distributions of the acceptance in the two decay angles θ_{GJ} and ϕ_{GJ} already introduced in Sections 3.2.5, 8.1.3 and 8.2.3. The MC data has been generated isotropically in those two variables. Hence, any deviation of the accepted MC data from an isotropic distribution is due to the acceptance. In Fig. 9.2, we show the one-dimensional distribution of the acceptance for the $K_s^0\pi^-$ final state as a function of $\cos\theta_{\mathrm{GJ}}$ and ϕ_{GJ}, respectively. Again, the corresponding distributions for the $K_s^0K^-$ final state look very similar (see Fig. B.2). The acceptance in $\cos\theta_{\mathrm{GJ}}$ rises nearly linearly with $\cos\theta_{\mathrm{GJ}}$ from approximately 18 to 26% for $K_s^0\pi^-$(from 22 to 30% for $K_s^0K^-$), with two drops at $\cos\theta_{\mathrm{GJ}} \approx \pm 1$, i.e. in backward and forward direction of the π^- (or K^- for $K_s^0K^-$). In these kinematic regions, we lose about 5 and 10%, respectively, but the acceptance never drops below 10%. The distribution of the acceptance in ϕ_{GJ} is less modulated, and stays within ±5% points around the average. The acceptance slightly decreases towards $\phi_{\mathrm{GJ}} = 0°$ and $\pm 180°$. Figure 9.3 shows the two-dimensional distribution of the acceptance in $\cos\theta_{\mathrm{GJ}}$ and ϕ_{GJ}. We observe a slight correlation of the acceptance in both variables: the decrease in acceptance at $\phi_{\mathrm{GJ}} = 0$ appears only

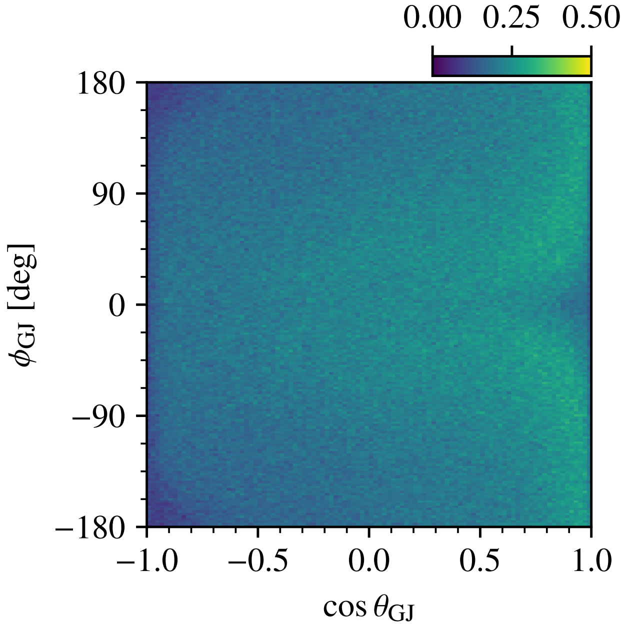

Figure 9.3: Acceptance as a function of $\cos\theta_{\mathrm{GJ}}$ and ϕ_{GJ}, averaged over the entire mass and t' range, for the $K_s^0\pi^-$ final state.

in forward direction, i.e. for $\cos\theta_{\mathrm{GJ}}$ near $+1$. Inversely, the lower acceptance at $\phi_{\mathrm{GJ}} = \pm 180°$ appears for negative $\cos\theta_{\mathrm{GJ}}$. Although we observe a slight angular dependence of the acceptance, it is important to note that there are no regions in which the acceptance is worryingly low as was the case for $K^-K^+\pi^-$ (c.f. Fig. 5.11).

In order to study the dependence of the angular acceptance on the two-body mass, we show in Fig. 9.4 the angular distributions of the acceptance averaged over narrower $m_{K_s^0\pi}$ ranges. We can recognize the same tendencies as observed in the one-dimensional distributions of the angles. We observe a $m_{K_s\pi}$ dependence of the structures in Fig. 9.3: at low $m_{K_s^0\pi} < 1.15$ GeV/c^2, the region with lower acceptance at $\phi_{\mathrm{GJ}} = 0$ spans over the entire $\cos\theta_{\mathrm{GJ}}$ range, while with increasing $m_{K_s\pi}$ it moves toward $\cos\theta_{\mathrm{GJ}} = +1$.

To conclude, these studies have shown that for both the $K_s^0\pi^-$ and the $K_s^0K^-$ channel, the acceptances depend only weakly on the two-body mass and t'. There are slight modulations of the acceptance in the decay angles $\cos\theta_{\mathrm{GJ}}$ and ϕ_{GJ}, but these do not reach a critical level. Generally, as long as

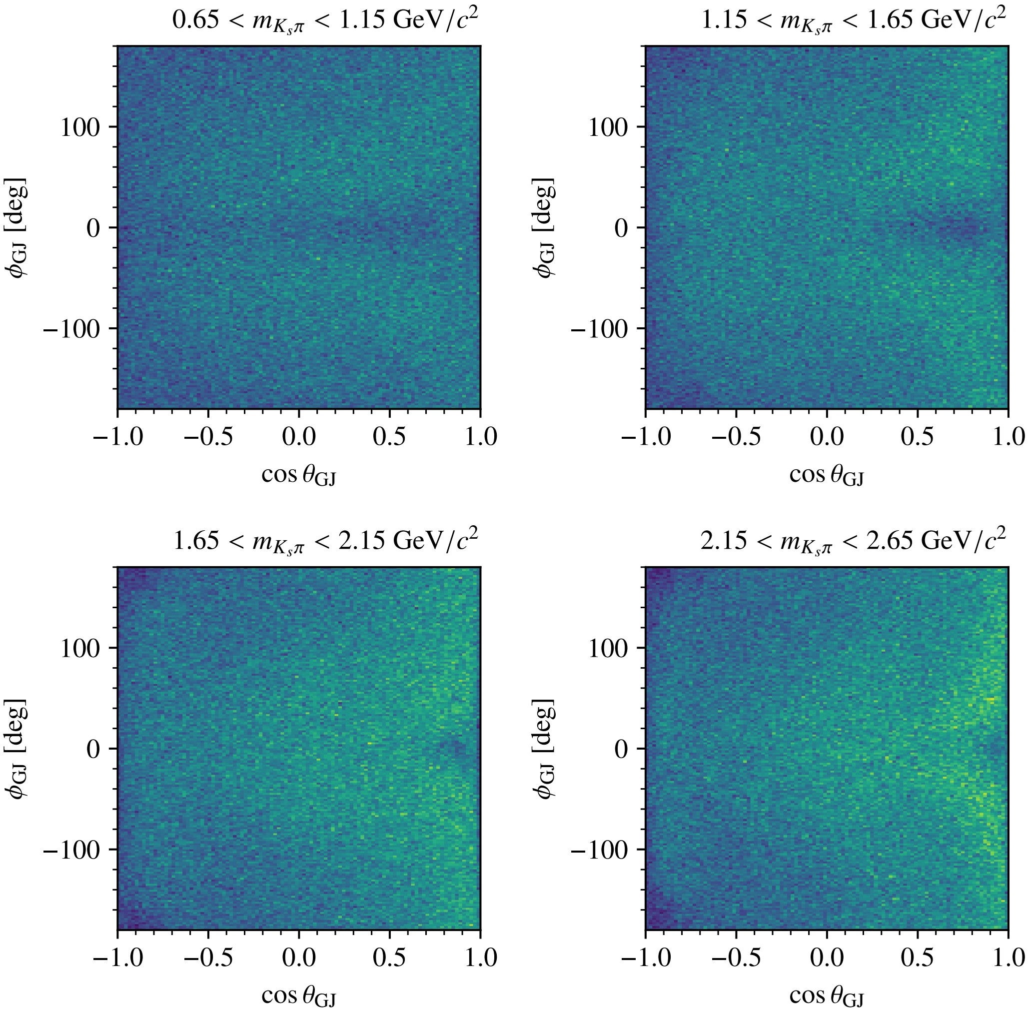

Figure 9.4: Acceptance as a function of $\cos\theta_{\mathrm{GJ}}$ and ϕ_{GJ} in different $m_{K_s\pi}$ ranges, for the $K_s^0\pi^-$ final state. The acceptance goes from 0 to 50%.

the acceptance of the setup is known accurately and there are no regions with vanishing acceptance, the acceptance effects can be corrected for in the PWA.

9.2 Mass, Angular, and t' Resolution

We can also use the accepted MC dataset to estimate the resolution of the setup by studying the distribution of the residuals, i.e. of the difference of the MCT and the reconstructed value for a given kinematic variable,. These distributions are expected to peak at zero. Their width corresponds to the resolution of the experimental setup for the given variable.

Figure 9.5 shows the distribution of the residuals for the two-body mass for the $K_s^0\pi^-$ and $K_s^0K^-$ final states. In order to extract the widths, i.e. the mass resolution (averaged over the entire mass range), we fit the distributions with a double Gaussian, i.e. we use the equivalent of Eq. (7.1), but without the background component $(a, b, c = 0)$. Using Eq. (7.3) to calculate the weighted width yields an resolution of 12.2 MeV/c^2 for $m_{K_s\pi}$ and 12.5 MeV/c^2 for m_{K_sK}.

Another interesting variable to study is reconstructed $\pi^-\pi^+$ mass from the V^0 decay. As mentioned in Section 8.1.1, due to the negligible natural width of the K_S^0, the deviation of the measured $\pi^-\pi^+$ mass from the nominal K_s^0 mass is only because of the limited resolution of the experimental setup. Hence we can compare our resolution estimate with the width of the peak in real data shown in Fig. 7.6. We fit the distributions of the residuals shown in Fig. 9.6 using the same function as for real data, i.e. a double Gaussian with polynomial background equivalent to Eq. (7.1). This yields a $\pi^-\pi^+$ mass resolution of 5.0 MeV/c^2 for $K_s^0\pi^-$ and 4.9 MeV/c^2 for $K_s^0K^-$. From real data, we have determined resolutions of 6.5 MeV/c^2 for $K_s^0\pi^-$ and 6.23 MeV/c^2 for $K_s^0K^-$. This might indicate that the detector simulation slightly underestimates the resolution. However, we have to take into account that the kinematic distri-

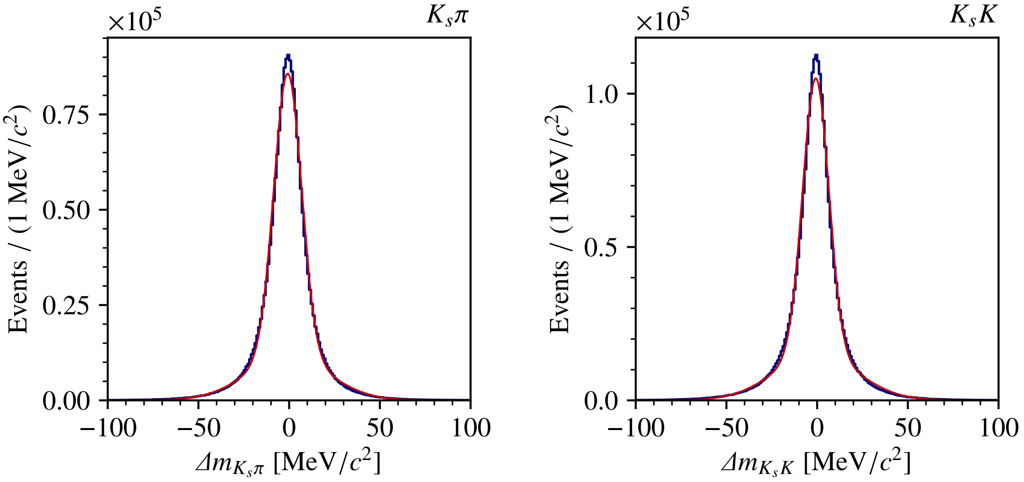

Figure 9.5: Distribution of the residuals for (left) the $K_s^0\pi^-$ mass and (right) the $K_s^0K^-$ mass. The fit curves are drawn in red.

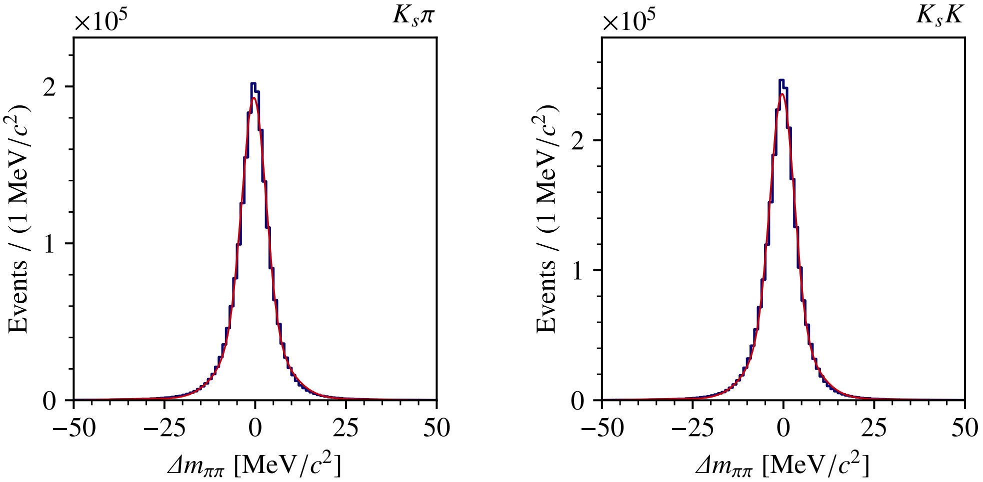

Figure 9.6: Distribution of the residuals for the $\pi^-\pi^+$ mass for (left) $K_s^0\pi^-$ and (right) $K_s^0K^-$. The fit curves are drawn in red.

butions of the MC pseudodata are isotropic in phase-space, which might also influence our resolution estimate.

Using the same approach,we study the resolutions of the Gottfried-Jackson angles θ_{GJ} and ϕ_{GJ}. Figure 9.7 shows the distributions of the residuals for $\cos\theta_{\mathrm{GJ}}$ and ϕ_{GJ} for the $K_s^0\pi^-$ data. The distributions for $K_s^0K^-$ are similar. We fit the distributions by a double Gaussian to extract their widths. As can be seen in Fig. 9.7, the fit function does not describe the distributions perfectly, especially concerning the top of the peaks. However, we consider the fits sufficient to extract the approximate resolution values. We obtain average resolutions of $\sigma(\cos\theta_{\mathrm{GJ}}) = 0.008$ and $\sigma(\phi_{\mathrm{GJ}}) = 1.20°$ for $K_s^0\pi^-$ and $\sigma(\cos\theta_{\mathrm{GJ}}) = 0.006$ and $\sigma(\phi_{\mathrm{GJ}}) = 1.24°$ for $K_s^0K^-$.

Finally, we study the resolution of the reduced four-momentum transfer squared t'. Again, the distributions of the residuals are shown in Fig. 9.8. Fitting a double Gaussian to the distributions yields an average t' resolution of 9.2×10^{-3} $(\mathrm{GeV}/c)^2$ for $K_s^0\pi^-$ and 10.2×10^{-3} $(\mathrm{GeV}/c)^2$ for $K_s^0K^-$.

9.3 Background Studies

By generating Monte Carlo data for possible background reactions and processing them with the event selection for $K_s^0\pi^-$ and $K_s^0K^-$ channel, respectively, we can estimate the amount of background in the selected data. We will

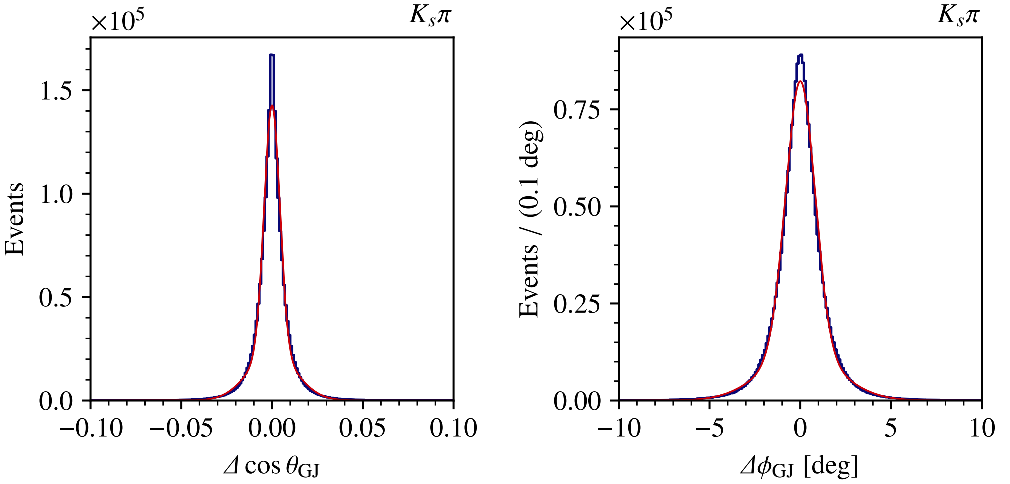

Figure 9.7: Distribution of the residuals for (left) $\cos\theta_{\mathrm{GJ}}$ and (right) ϕ_{GJ} for $K_s^0\pi^-$. The fit curves are drawn in red.

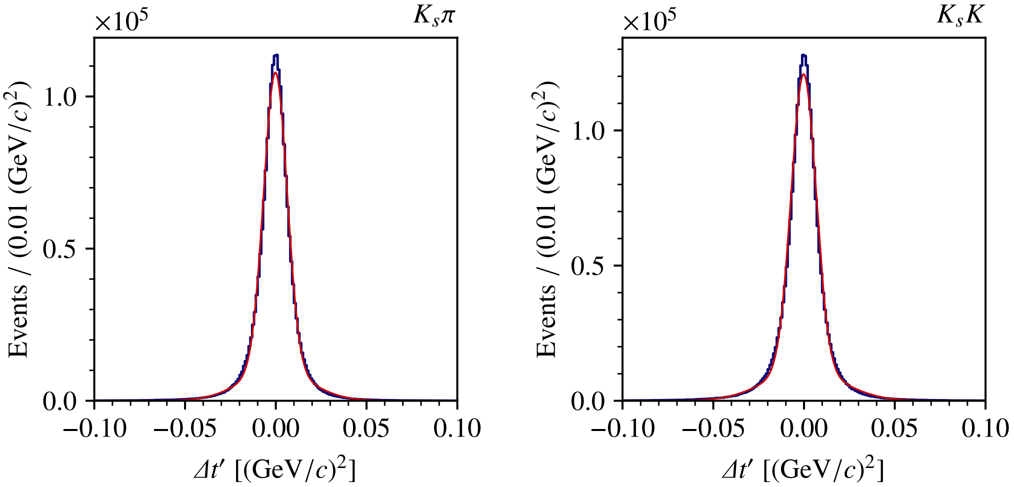

Figure 9.8: Distribution of the residuals for t' for (left) $K_s^0\pi^-$ and (right) $K_s^0K^-$. The fit curves are drawn in red.

explain the procedure for the case where we estimate the $K_s^0\pi^-$ background in the $K_s^0K^-$ channel. For this, we generated 10^7 MC $K_s^0\pi^-$ events and applied the $K_s^0K^-$ event selection to this dataset. After the $K_s^0K^-$ event selection, 32 288 $K_s^0\pi^-$ events remain, i.e. a fraction of $R_{K_sK}^{K_s\pi} = 3.2 \times 10^{-3}$ of the $K_s^0\pi^-$ events leaks into the $K_S^0K^-$ data. In order to estimate the $K_s^0\pi^-$ background in the real $K_s^0K^-$ dataset from this number, we first have to estimate the total amount of $K_s^0\pi^-$ events produced in the real data. For this, we use the overall phase-space acceptance that we calculated in Section 9.1 to 20.8% for the $K_s^0\pi^-$ channel. In real data, we measured 57 216 $K_s^0\pi^-$ events for both years. This corresponds to 280 000 produced $K_s^0\pi^-$ events. Multiplying this with $R_{K_sK}^{K_s\pi}$ gives us a $K_s^0\pi^-$ background estimate of 880 events in the $K_s^0K^-$ dataset. This corresponds to a $K_s^0\pi^-$ background of 0.2%.

It is important to note that this procedure is only a rough approximation. The estimated amount of real data events is far from exact, as we only scale it by the overall acceptance in the channel. Besides, the MC data on which we perform the event selection is generated isotropically in phase space and does not incorporate the real phase-space distributions of the data, which may influence the number of selected events and the acceptance. A realistic estimate can only be obtained once a PWA fit was performed successfully. Still, these calculations give us an order-of-magnitude estimate of the amount of $K_s^0\pi^-$ background in our $K_s^0K^-$ data, which seems to be low.

We use the same approach to study the $K_s^0K^-$ background in the $K_s^0\pi^-$ data. From the initial 10^7 MC events, 2 807 events pass the $K_s^0\pi^-$ event selection, i.e. $R_{K_s\pi}^{K_sK} = 2.8 \times 10^{-4}$. We estimate the total number of produced events in the measured data to 1 700 000. This corresponds to a contamination of 470 $K_s^0K^-$ background events in the real $K_s^0\pi^-$ data, equivalent to a background fraction of 0.8%, which is again small.

Lastly, we have applied the same procedure to another possible source of background, the reaction $\pi^- + p \to \pi^-\pi^-\pi^+ + p$. There, we use a MC dataset of 48×10^6 events that are generated following a realistic phase-space distribution, estimated by a PWA fit of the 3π data [3]. A rough approximation of the number of produced $\pi^-\pi^-\pi^+$ reactions in the years 2008 and 2009 yields 257×10^6 events. No $\pi^-\pi^-\pi^+$ events pass the $K_s^0\pi^-$ event selection, which indicates that the $\pi^-\pi^-\pi^+$ background in $K_s^0\pi^-$ is negligible. In $K_s^0K^-$, 248 $\pi^-\pi^-\pi^+$ events pass the event selection. This corresponds to 1 300 events in the real $K_s^0K^-$ dataset, or 0.3% of the $K_s^0K^-$ events, which again is negligibly small. We thus conclude that in both channels, $\pi^-\pi^-\pi^+$ events are only a very minor source of background, despite the comparatively large cross-section of this process.

Chapter 10

Conclusions and Outlook

We have performed a first analysis of COMPASS data on the reactions $K^- + p \to K_s^0\pi^- + p$ and $\pi^- + p \to K_s^0 K^- + p$. In both reactions, a K_s^0 is produced, which, as a neutral particle, cannot be detected directly in the spectrometer but is reconstructed by its decay into $\pi^-\pi^+$. Although the two analyzed final states are produced by different beam-particle species and hence contain different resonances, they have a quite similar experimental signature. In this thesis, we have developed an event selection for both final states. Performing this selection on the datasets taken by the COMPASS experiment in the years 2008 and 2009 yields clean samples of 57 216 $K_s^0\pi^-$ events and 417 081 $K_s^0 K^-$ events. By inspecting the invariant mass and angular distributions of the $K_s^0\pi^-$ system, we have clearly identified two well-known resonances, the $K^*(892)$ and the $K_2^*(1430)$, that contribute significantly to the data. For the $K_s^0 K^-$ final state, the same studies have shown that the well-known $a_2(1320)$ resonance dominates the distributions. In both reactions, we have found indications for further high-mass resonances, that also have been reported by previous experiments. Overall, our datasets are in good agreement with those of a previous experiment that studied the same reactions. Several studies on possible background contributions have shown that our data contain only small contaminations from other processes.

Using Monte Carlo data, we have studied the acceptances and resolutions for both channels. We find that the acceptances depend quite weakly on the two-body masses and t'. Slightly larger modulations of the acceptance of up to approximately 50% are observed in the angles describing the $K_s^0\pi^-$ and $K_s^0 K^-$ systems. As these modulations are restricted to rather small phase-space regions, we do not consider them to be critical.

The selection of the data and the studies made in this part of the thesis are the first steps toward partial-wave analyses of the $K_s^0\pi^-$ and $K_s^0 K^-$ final states. First, two small improvements can be made concerning the selected datasets. Some of the employed cuts, such as the cut on the collinearity angle, were taken from previous analyses of COMPASS muon-beam data. The optimal cut ranges for our channels have been investigated by studying the significance of the $\pi^-\pi^+$ mass peak for different parameter values. One way of further improving these cuts would be to determine the resolutions in the concerned variables, like in Section 9.2 for the two-body mass and decay angles. Then, we could base the cut ranges on these resolutions, similar to what has been done for the reconstructed $\pi^-\pi^+$ mass. The analysis could also be improved further by performing a kinematic fit. By refitting the tracks of the secondary particles with the additional constraint that the resulting $\pi^-\pi^+$ mass equals exactly the nominal K_s^0 mass, we could improve the $K_s^0\pi^-$ and $K_s^0K^-$ mass resolutions. Furthermore, we could extend our studies of background contributions in the $K_s^0\pi^-$ and $K_s^0K^-$ datasets by inspecting the additional background sources $K^- + p \to K^-\pi^-\pi^+ + p$ and $K^- + p \to K_S^0\pi^-\pi^0 + p$.

Apart from the above-mentioned improvements, the next step would be to start the partial-wave analysis of the data. We have already been able to identify the dominant resonances contributing to the studied reactions, but many interesting resonances can only be detected by performing a PWA. As we have selected clean datasamples and the acceptance of the experimental setup is rather uniform, nothing is standing in the way of a reliable partial-wave analysis of the data. With such an analysis, we could identify further resonance states in the two investigated reactions. With our large $K_s^0K^-$ event sample, we should, for example, be able to confirm or refute the existence of the $a_6(2450)$, which has so far been observed only by Cleland et al. [5]. Furthermore, with our $K_s^0\pi^-$ dataset, that is similar in size to the dataset of the Belle collaboration in Ref. [6], we could perform a precise measurement of the mass of the $K^*(892)^\pm$ resonance. This could provide further information on the observed mass discrepancy discussed in Chapter 1.

Appendix A

Additional Material for the $K^-K^+\pi^-$ Channel

A.1 Construction of the Extended $K^-K^+\pi^-$ Waveset for Real Data

In the first PWA of the $K^-K^+\pi^-$ real data presented in Section 5.1, we employed the same waveset as the one used by the VES collaboration in their analysis of the same final state [14]. As the results of our PWA presented several issues, we attempted to improve the fit by refining and extending the waveset used in the PWA fit. This was done in two ways. The use of the waveset-selection technique to construct a waveset from a large number of starting waves was already presented in Section 5.3.4. We also constructed a waveset manually, starting with the waves that had also been used in the VES analysis. This will now be briefly presented. The method of manually constructing the waveset and its challenges and caveats have already been briefly treated in Section 5.3.1. Essentially, we iteratively added sets of waves into the waveset and then removed those waves that only picked up little relative intensity in the PWA fit. The sets of waves that were tentatively added to the waveset contained waves with total spin J from 0 to 4, angular momentum L from 0 to 4, and spin projections $M = 0, 1$, as well as several different K^+K^- and $K^+\pi^-$ isobars with masses below 2 GeV/c^2. This yielded a set of 47 waves (plus the flat wave), listed in Table A.1. The intensity distributions resulting from the PWA fit with this waveset are shown in Fig. A.1. Unfortunately, we did not observe an improvement of the PWA fit when using this waveset. Similar issues as the ones discussed in Section 5.1 arose. In particular, the intensity distributions of the waves still lack continuity between the $m_{KK\pi}$ bins, especially at low masses. Structure can be seen in the intensity distributions of some waves, but not in the expected ones, which further supports the hypothesis that there is still significant intensity leakage between the waves.

Given the unreliability of the PWA fit, it is thus probable that many of the waves listed in Table A.1 are not actually contained in the data, and, vice versa, that many waves present in the data have not been added in the waveset. This is further supported by the fact that, during the construction of the waveset, we even removed the $2^-0^+f_2(1270)\pi^-S$ wave, which had significant intensity in the VES analysis and in the COMPASS analysis of the $\pi^-\pi^-\pi^+$ final state. The correctness of this waveset is thus questionable. Nevertheless, it has been used in a slightly modified manner in the MC pseudodata studies in Sections 5.2.2.3 and 5.2.4.2. In addition to the waves in Table A.1, we included the $2^-0^+f_2(1270)\pi^-S$ wave, with which the MC pseudodata had been generated (see Section 5.2.1) and thus has to be used in the pseudodata fit, and the flat wave. The MC studies investigated the reliability of the PWA fit when including more waves into the PWA fit waveset than just those with which the MC pseudodata was generated. In these cases, it does not particularly matter whether the added waves are really present in the real data.

A.2 Distribution of the Acceptance in the $K^-K^+\pi^-$ Phase-Space Variables

Similar to Fig. 5.11, which shows the distribution of the acceptance in the phase-space variables ϕ_{GJ} and $\cos\theta_{\mathrm{GJ}}$ for a $K^+\pi^-$ isobar, this section presents further acceptance distributions in the remaining phase-space variables. Figure A.2 shows the acceptance in the same variables as Fig. 5.11, but in the $m_{KK\pi}$ regions around 1.6 GeV/c^2, 2.0 GeV/c^2, and 2.4 GeV/c^2, by averaging over all mass bins in the respective $m_{KK\pi}$ ranges (indicated in the top right of the plots). Figure A.3 shows the acceptance in the remaining phase-space variables, i.e. ϕ_{GJ} and $\cos\theta_{\mathrm{GJ}}$ for a K^+K^- isobar, as well as ϕ_{HF} and $\cos\theta_{\mathrm{HF}}$ for K^+K^- and $K^+\pi^-$ isobars. We show distributions in two mass regions around 1.8 GeV/c^2 and 2.2 GeV/c^2.

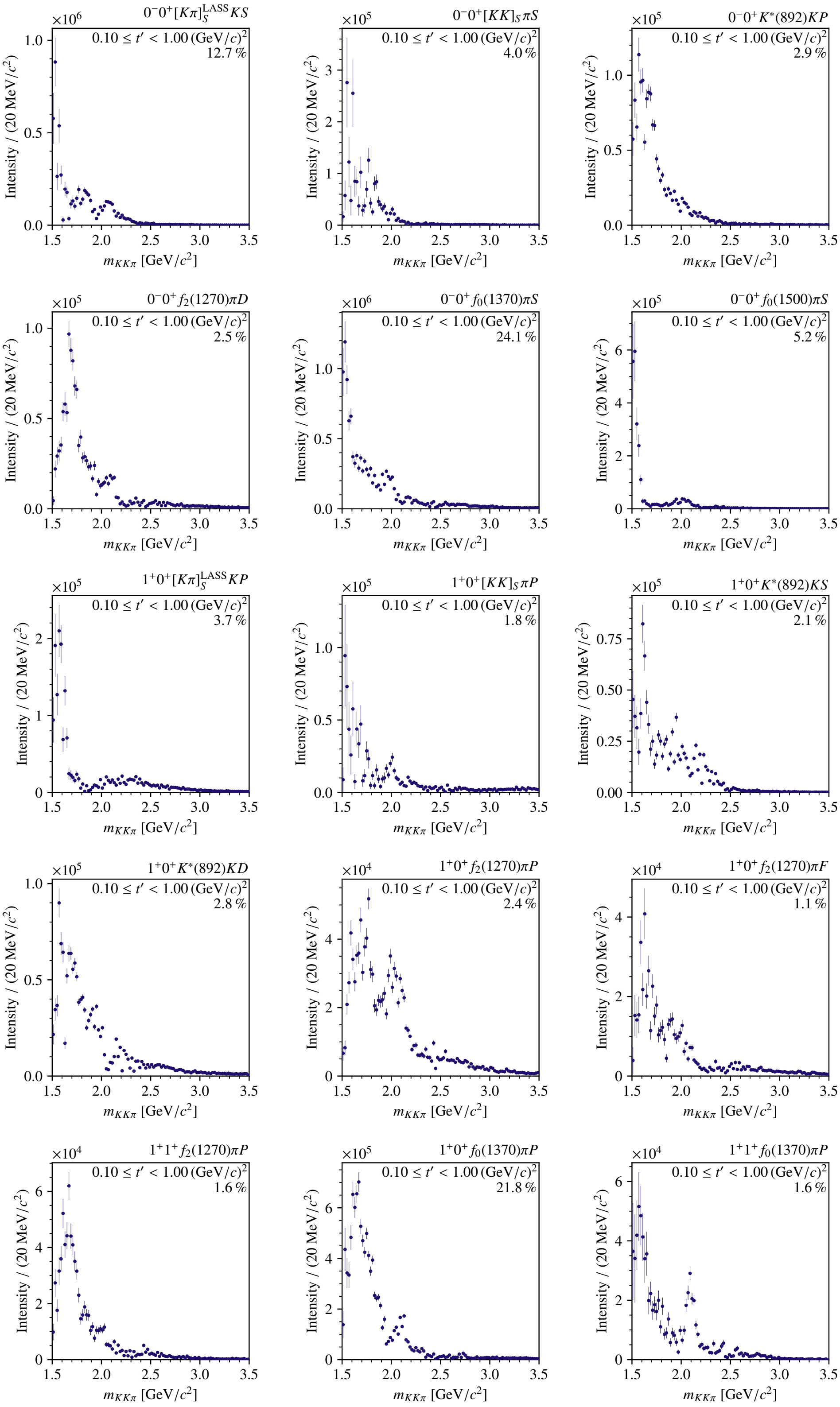

Figure A.1: Intensity distribution of partial waves resulting from the PWA fit of real data using the waveset in Table A.1.

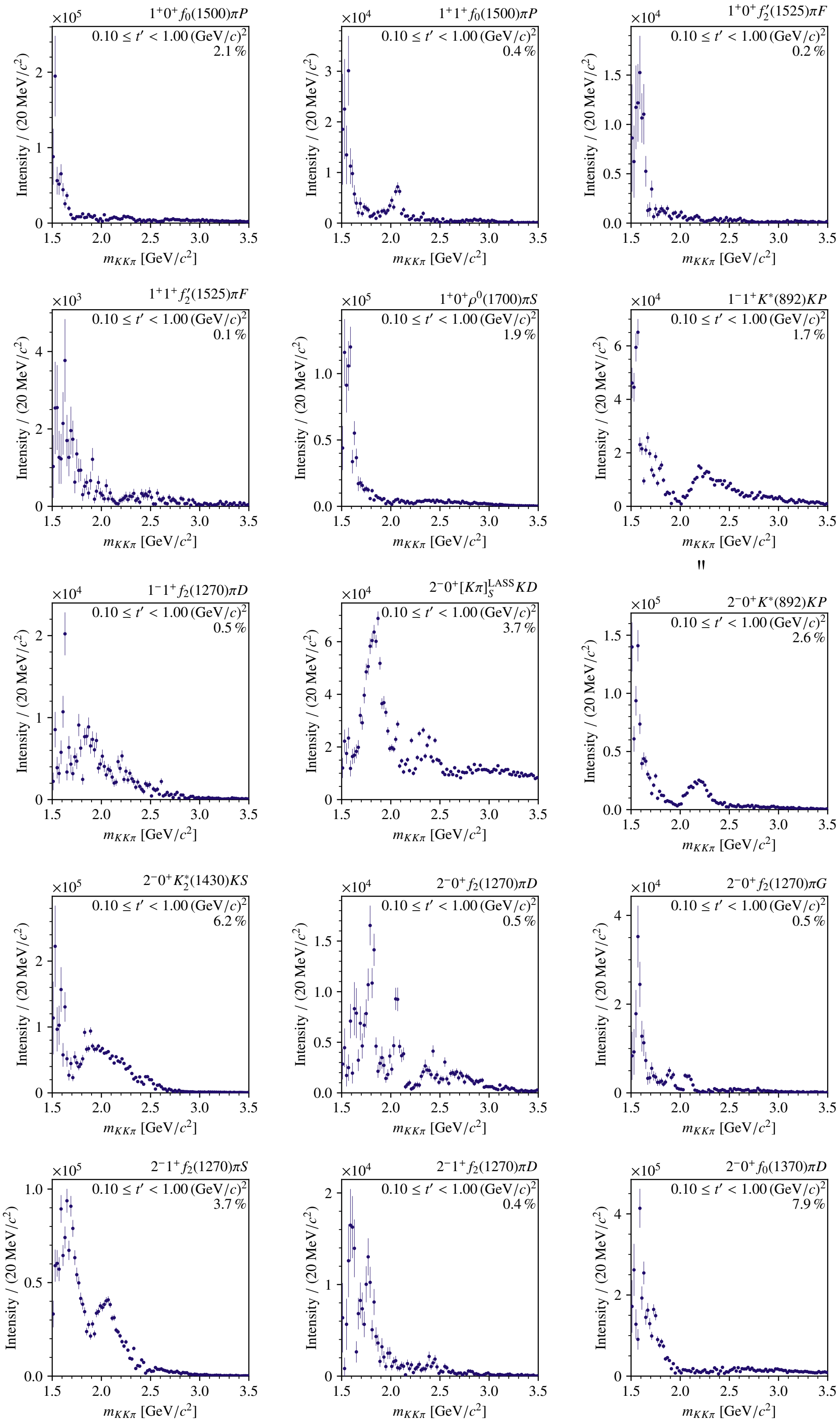

Figure A.1: Continued

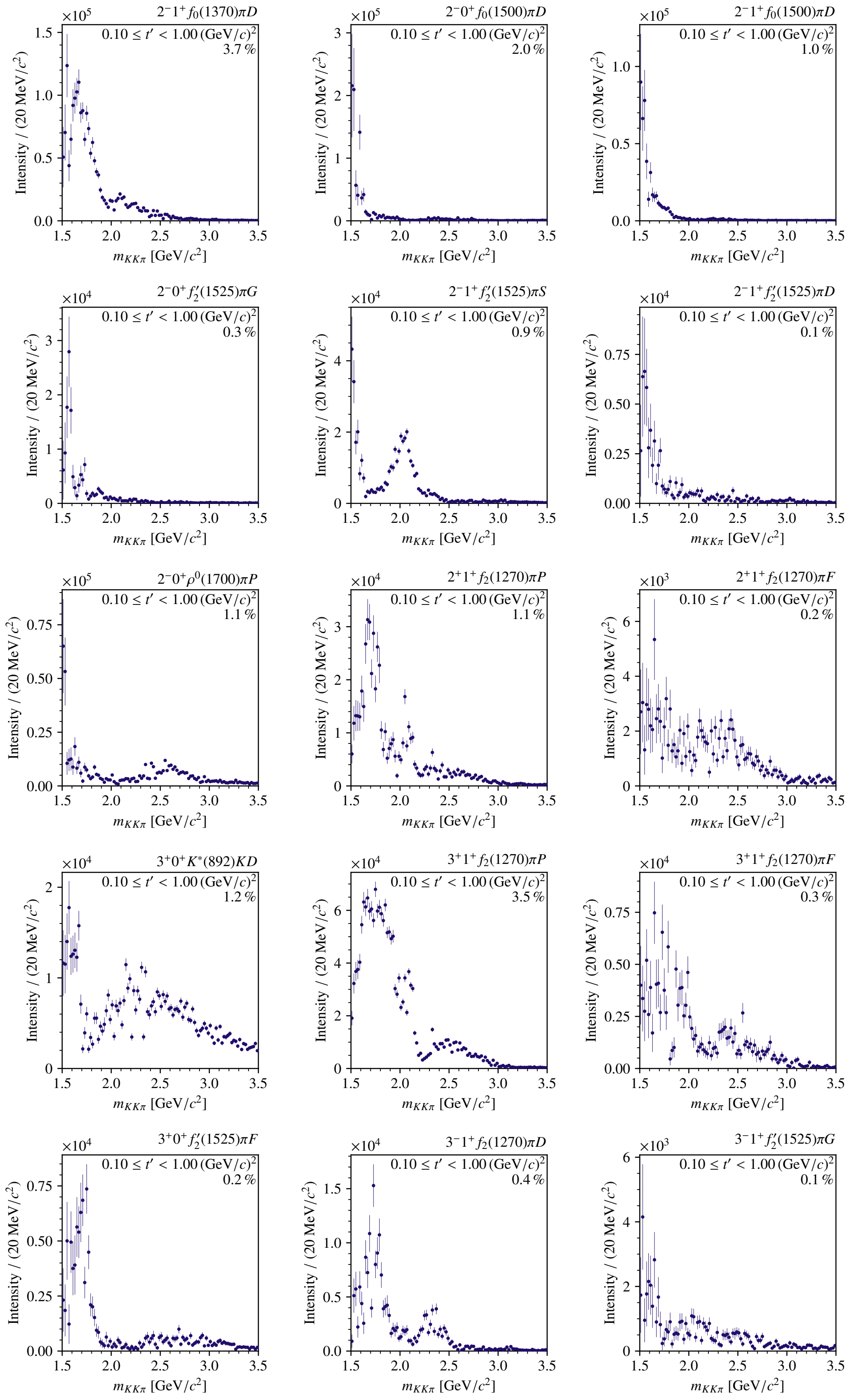

Figure A.1: Continued

Table A.1: List of the 47 waves of the extended $K^-K^+\pi^-$ waveset. This waveset, appended with the $2^-0^+f_2(1270)\pi^-S$ and flat waves (see text), was also used as extended waveset in the MC studies (see Sections 5.2.2.3 and 5.2.4.2).

$0^-0^+[K\pi]_S K^- S$	$1^+0^+[K\pi]_S K^- P$	$2^-0^+[K\pi]_S K^- D$	$3^+0^+K^*(892)K^- D$
$0^-0^+[KK]_S \pi^- S$	$1^+0^+[KK]_S \pi^- P$	$2^-0^+K^*(892)K^- P$	$3^+1^+f_2(1270)\pi^- P$
$0^-0^+K^*(892)K^- P$	$1^+0^+K^*(892)K^- S$	$2^-0^+K_2^*(1430)K^- S$	$3^+1^+f_2(1270)\pi^- F$
$0^-0^+f_2(1270)\pi^- D$	$1^+0^+K^*(892)K^- D$	$2^-0^+f_2(1270)\pi^- D$	$3^+0^+f_2'(1525)\pi^- F$
$0^-0^+f_0(1370)\pi^- S$	$1^+0^+f_2(1270)\pi^- P$	$2^-0^+f_2(1270)\pi^- G$	$3^-1^+f_2(1270)\pi^- D$
$0^-0^+f_0(1500)\pi^- S$	$1^+0^+f_2(1270)\pi^- F$	$2^-1^+f_2(1270)\pi^- S$	$3^-1^+f_2'(1525)\pi^- G$
	$1^+1^+f_2(1270)\pi^- P$	$2^-1^+f_2(1270)\pi^- D$	
	$1^+0^+f_0(1370)\pi^- P$	$2^-0^+f_0(1370)\pi^- D$	$4^-1^+f_2(1270)\pi^- G$
	$1^+1^+f_0(1370)\pi^- P$	$2^-1^+f_0(1370)\pi^- D$	$4^-1^+f_2'(1525)\pi^- G$
	$1^+0^+f_0(1500)\pi^- P$	$2^-0^+f_0(1500)\pi^- D$	
	$1^+1^+f_0(1500)\pi^- P$	$2^-1^+f_0(1500)\pi^- D$	
	$1^+0^+f_2'(1525)\pi^- F$	$2^-0^+f_2'(1525)\pi^- G$	
	$1^+1^+f_2'(1525)\pi^- F$	$2^-1^+f_2'(1525)\pi^- S$	
	$1^+0^+\rho(1700)\pi^- S$	$2^-1^+f_2'(1525)\pi^- D$	
	$1^-1^+K^*(892)K^- P$	$2^-0^+\rho(1700)\pi^- P$	
	$1^-1^+f_2(1270)\pi^- D$	$2^+1^+f_2(1270)\pi^- P$	
		$2^+1^+f_2(1270)\pi^- F$	

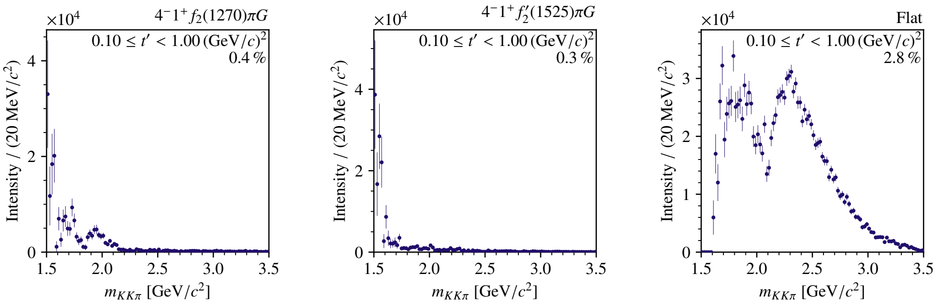

Figure A.1: Continued

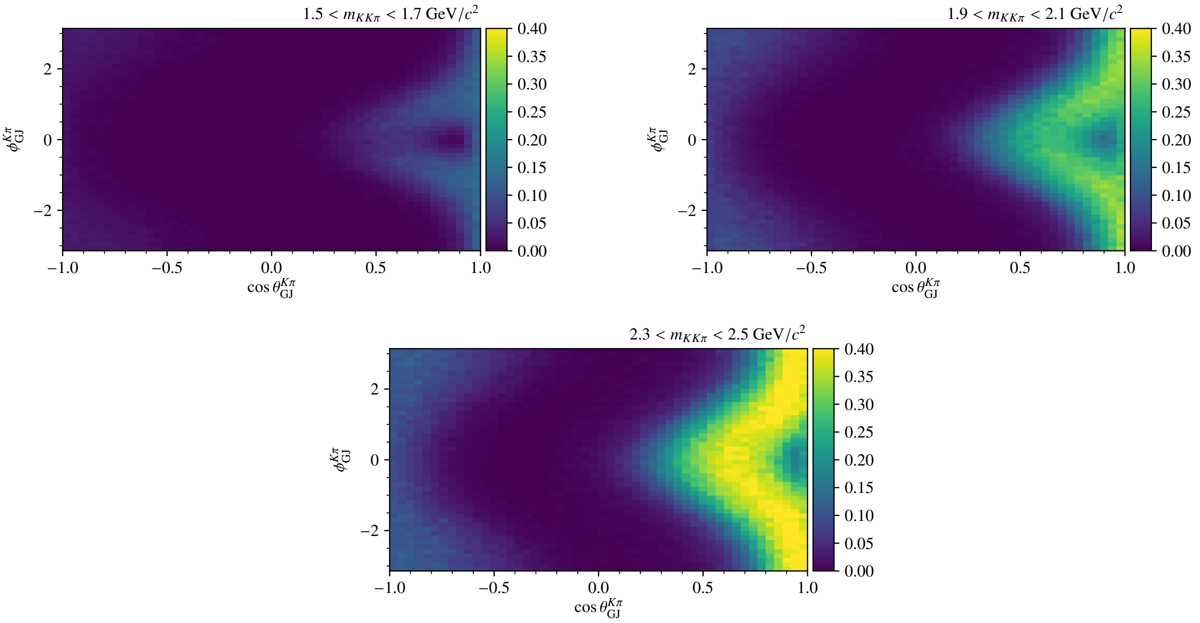

Figure A.2: Dependence of the acceptance on the phase-space variables ϕ_{GJ} and $\cos\theta_{\mathrm{GJ}}$ that describe the decay of X^- into a $K^+\pi^-$ isobar and a bachelor K^-. From top to bottom, left to right: Acceptance in the 1.6 GeV/c^2, 2.0 GeV/c^2, and 2.4 GeV/c^2 mass regions. See also Fig. 5.11.

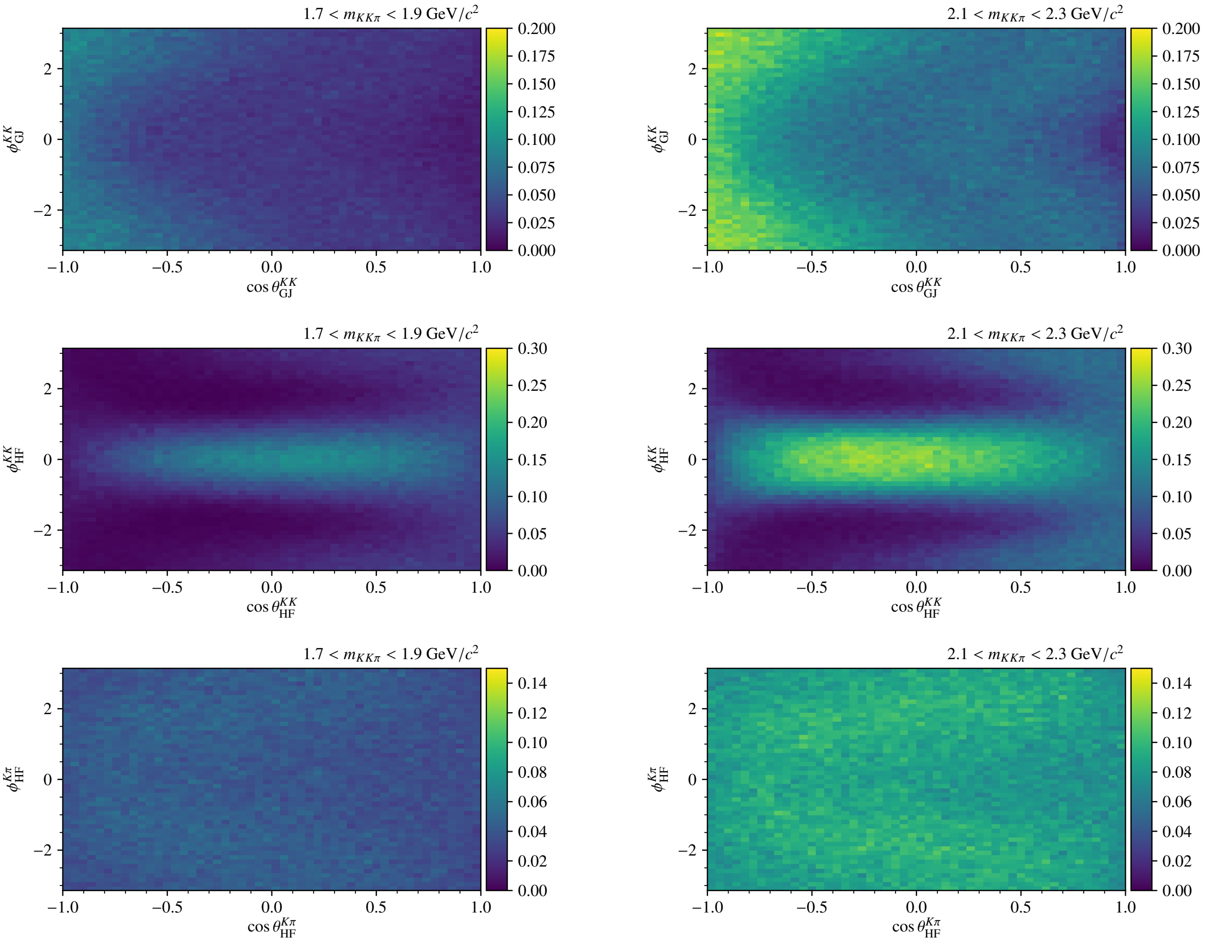

Figure A.3: Dependence of the acceptance on the phase-space variables, in two different mass regions (columns). (Top row) Acceptance as a function of ϕ_{GJ} and $\cos\theta_{\mathrm{GJ}}$ for a K^+K^- isobar; (center row) ϕ_{HF} and $\cos\theta_{\mathrm{HF}}$ for a K^+K^- isobar; (bottom row) ϕ_{HF} and $\cos\theta_{\mathrm{HF}}$ for a $K^+\pi^-$ isobar. See also Figs. 5.11 and A.2.

Appendix B

Additional Material for the $K_s^0\pi^-$ and $K_s^0K^-$ Channels

B.1 Acceptance for the $K_s^0K^-$ Final State

In Section 9.1, we showed the acceptance for the $K_s^0\pi^-$ channel. In this section, we present the same distributions for the $K_s^0K^-$ channel. The overall acceptance is slightly higher for $K_s^0K^-$, but the dependence of the acceptance on m_{K_sK}, t' (shown in Fig. B.1) and the decay angles (shown in Figs. B.2 to B.4) is very similar to $K_S^0\pi^-$.

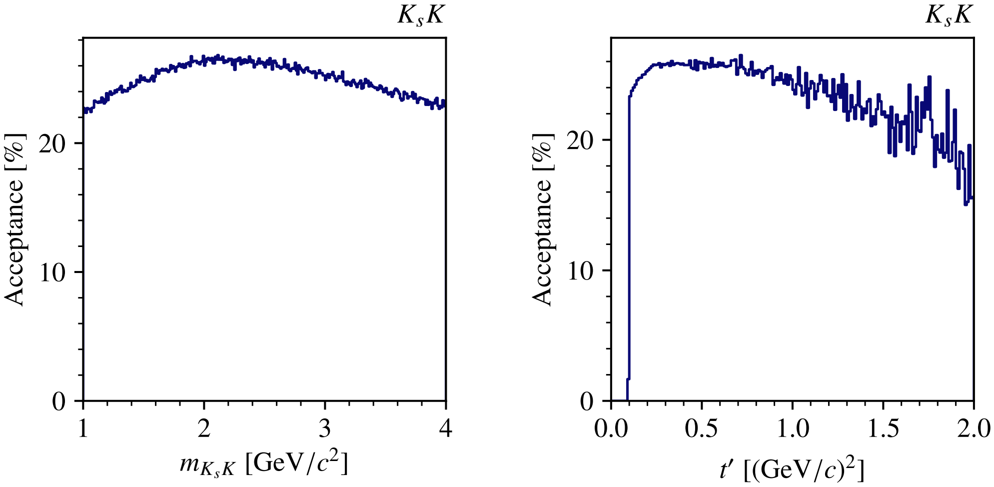

Figure B.1: Acceptance as a function of (left) the K_sK^- mass and (right) t' for the $K_s^0K^-$ final state.

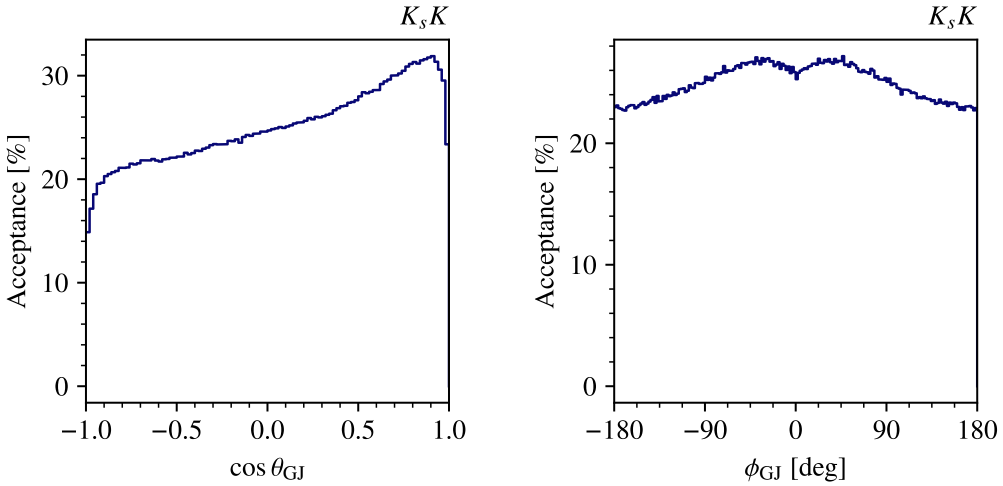

Figure B.2: Acceptance as a function of (left) $\cos\theta_{\mathrm{GJ}}$ and (right) ϕ_{GJ}, for the $K_s^0K^-$ final state.

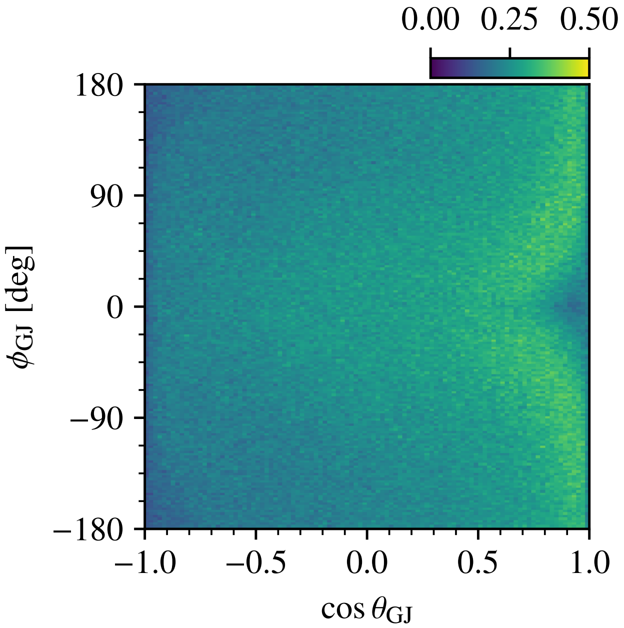

Figure B.3: Acceptance as a function of $\cos\theta_{\mathrm{GJ}}$ and ϕ_{GJ}, for the $K_s^0K^-$ final state.

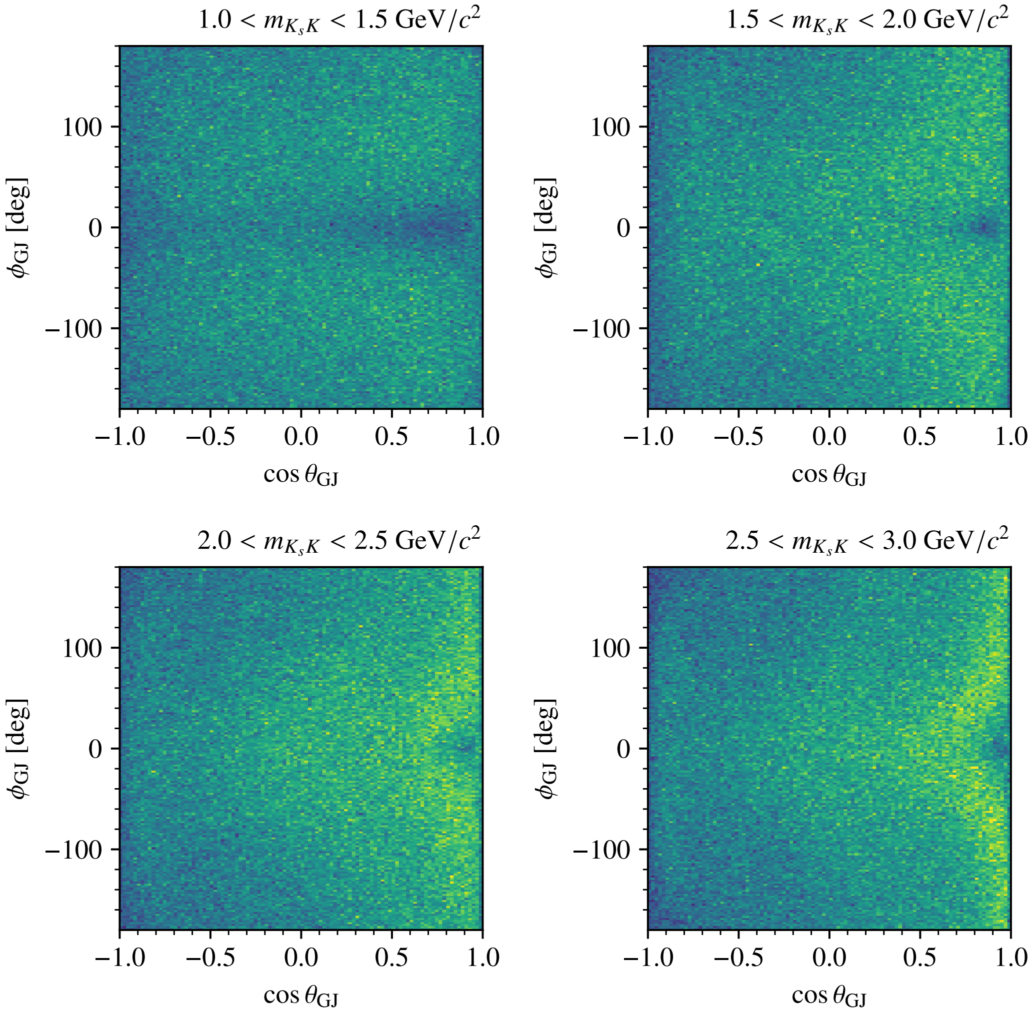

Figure B.4: Acceptance as a function of $\cos\theta_{\mathrm{GJ}}$ and ϕ_{GJ} in different m_{K_sK} ranges for the $K_s^0K^-$ final state. The acceptance goes from 0 to 50%.

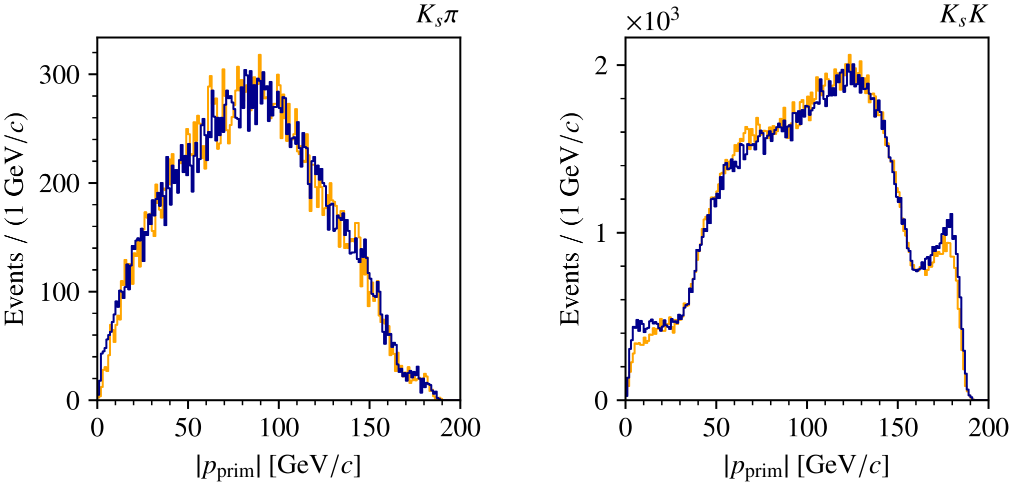

Figure B.5: Distributions of the momentum of the primary scattered particle, for (left) the $K_s^0\pi^-$ and (right) the $K_s^0K^-$ final states.

B.2 Distributions of the Final-State Momenta

The distributions of the particle momenta have not been discussed in Chapter 8, but will be shortly presented here. The distributions of the momentum of the primary scattered particle are shown in Fig. B.5, and the distributions of the momenta of the secondary particles are shown in Fig. B.6. While the latter exhibit an expected shape, the distributions of the primary-particle momenta in Fig. B.5 exhibit interesting structures. Especially for the $K_s^0K^-$ final state, we observe a peculiar increase of events at low and high momenta. As the phase-space Monte Carlo distributions do not exhibit such structures, they do not stem from acceptance effects but must rather have a physical cause, which is as of yet unclear. Further investigation is required.

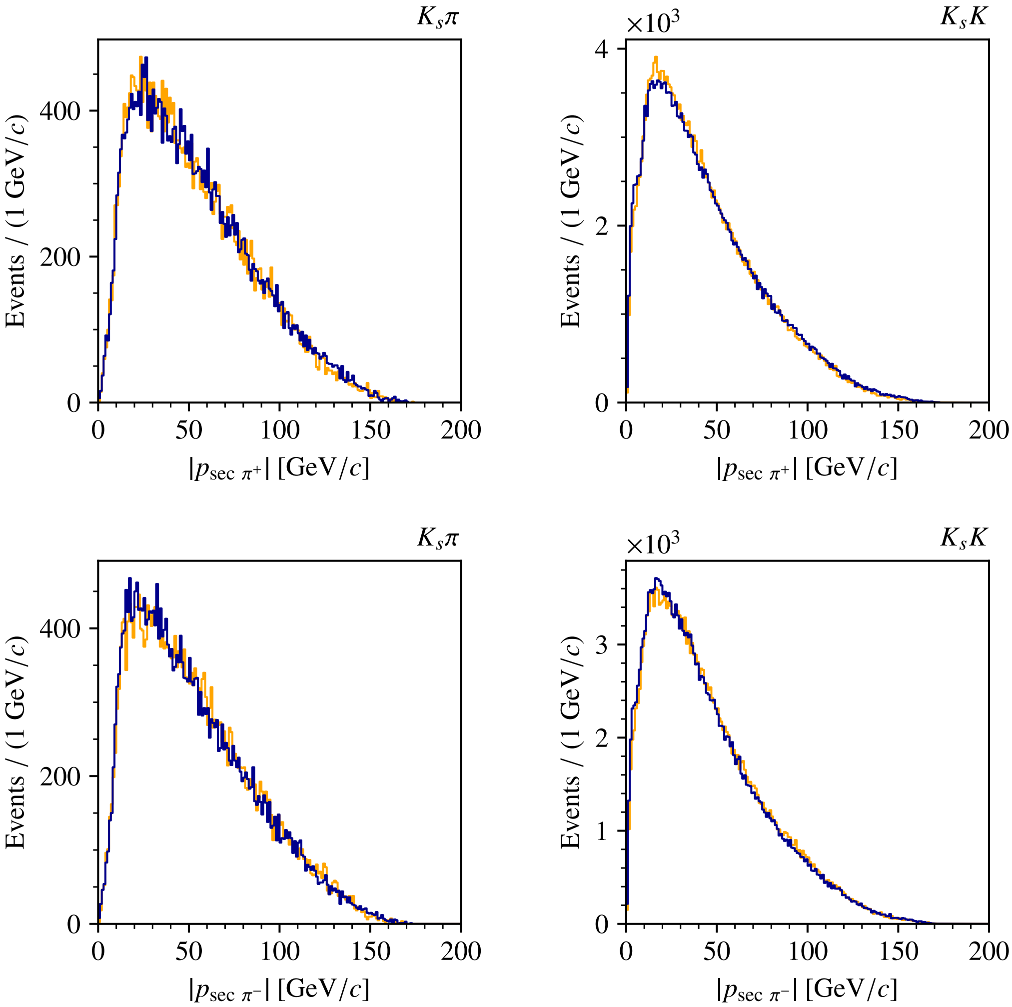

Figure B.6: Distributions of the momentum of (top row) the positive and (bottom row) the negative secondary particle, for (left column) the $K_s^0\pi^-$ and (right column) the $K_s^0K^-$ final states.

Bibliography

[1] C. Adolph et al., COMPASS collaboration. »Observation of a New Narrow Axial-Vector Meson $a_1(1420)$«. In: *Phys. Rev. Lett.* 115 (2015), p. 082001. DOI: `10.1103/PhysRevLett.115.082001`. arXiv: `1501.05732 [hep-ex]`.

[2] C. Adolph et al., COMPASS collaboration. »Resonance Production and $\pi\pi$ S-wave in $\pi^- + p \to \pi^-\pi^-\pi^+ + p_{\text{recoil}}$ at 190 GeV/c«. In: *Phys. Rev. D* 95 (2017), p. 032004. DOI: `10.1103/PhysRevD.95.032004`. arXiv: `1509.00992 [hep-ex]`.

[3] M. Aghasyan et al., COMPASS collaboration. »Light isovector resonances in $\pi^- p \to \pi^-\pi^-\pi^+ p$ at 190 GeV/c«. In: *Phys. Rev. D* 98 (2018), p. 092003. DOI: `10.1103/PhysRevD.98.092003`. arXiv: `1802.05913 [hep-ex]`.

[4] W.E. Cleland et al. »Study of the Reactions $K^{\pm}p \to K^0_s\pi^{\pm}p$ at 30 and 50 GeV/c: Description of the Apparatus and Amplitude Analysis of the $K^0_s\pi$ System«. In: *Nuclear Physics B* 208.2 (1982), pp. 189–227. ISSN: 0550-3213. DOI: `https://doi.org/10.1016/0550-3213(82)90114-6`.

[5] W. E. Cleland et al. »Resonance Production in the Reaction $\pi^{\pm}p \to K^0_s K^{\pm}p$ at 30 GeV/c and 50 GeV/c«. In: *Nucl. Phys. B* 208 (1982), pp. 228–261. DOI: `10.1016/0550-3213(82)90115-8`.

[6] D. Epifanov et al. »Study of $\tau \to K_s\pi^-\nu_\tau$ decay at Belle«. In: *Physics Letters B* 654.3 (2007), pp. 65–73. ISSN: 0370-2693. DOI: `https://doi.org/10.1016/j.physletb.2007.08.045`. URL: `https://www.sciencedirect.com/science/article/pii/S0370269307010313`.

[7] C. Dittrich. »Selektion des Prozesses $\pi^- + p \to \pi^- + K^- + K^+ + p$ aus COMPASS Daten«. Bachelor's thesis. TU München, 2019. URL: `https://wwwcompass.cern.ch/compass/publications/theses/2019_bac_dittrich.pdf`.

[8] Ph. Abbon et al., COMPASS Collaboration. »The COMPASS Setup for Physics with Hadron Beams«. In: *Nucl. Instrum. Methods Phys. Res. A* 779 (2014), pp. 69–115. DOI: `http://dx.doi.org/10.1016/j.nima.2015.01.035`. arXiv: `1410.1797`.

[9] Bernhard Ketzer, Boris Grube and Dmitry Ryabchikov. »Light-Meson Spectroscopy with COMPASS«. In: *Prog. Part. Nucl. Phys.* 113 (2020), p. 103755. DOI: `10.1016/j.ppnp.2020.103755`. arXiv: `1909.06366 [hep-ex]`.

[10] M. E. Rose. *Elementary Theory of Angular Momentum.* Ed. by Dover Publications. 1957. ISBN: 978-0-486-78879-1.

[11] Stefan Wallner. PhD thesis in preparation. TU München, 2021.

[12] Stefan Wallner. »Partial-Wave Decomposition of the Reaction $K^- + p \to K^-\pi^-\pi^+ + p$«. In: *COMPASS Release Note, August 2019* (2019). URL: `https://wwwcompass.cern.ch/compass/results/.html/2019/august_Kpipi_PWA/index.html`.

[13] P.A. Zyla et al. »Review of Particle Physics«. In: *PTEP* 2020 (2020), p. 083C01. DOI: `10.1093/ptep/ptaa104`. URL: `pdg.lbl.gov`.

[14] E.B. Berdnikov et al., VES collaboration. »Study of the reaction $\pi^- A \to K^- K^+ \pi^- A$ at 37 GeV/c«. In: *Physics Letters B* 337 (1994), pp. 219–225. DOI: `https://doi.org/10.1016/0370-2693(94)91471-0`.

[15] D. Aston et al. »A Study of $K^-\pi^+$ Scattering in the Reaction $K^- p \to K^+\pi^+ n$ at 11-GeV/c«. In: *Nucl. Phys. B* 296 (1988), pp. 493–526. DOI: `10.1016/0550-3213(88)90028-4`.

[16] Florian M. Kaspar et al. »Wave-Selection Techniques for Partial-Wave Analysis in Light-Meson Spectroscopy«. In: *18th International Conference on Hadron Spectroscopy and Structure.* Dec. 2019. DOI: `10.1142/9789811219313_0079`. arXiv: `1912.09849 [hep-ex]`.

[17] B Adams et al. »COMPASS++/AMBER: Proposal for Measurements at the M2 beam line of the CERN SPS Phase-1: 2022-2024«. In: *CERN-SPSC-2019-022, SPSC-P-360* (May 2019). URL: `http://cds.cern.ch/record/2676885`.

[18] S. Wallner et al. *Event Selection of the Reaction $K^- + p \to K^-\pi^-\pi^+ + p$.* COMPASS Release Note, July 2019. URL: `https://wwwcompass.cern.ch/compass/results/.html/2019/august_Kpipi_Data/index.html`.

[19] M. Alekseev et al. »Measurement of the Longitudinal Spin Transfer to Lambda and Anti-Lambda Hyperons in Polarised Muon DIS«. In: *Eur. Phys. J. C* 64 (2009), pp. 171–179. DOI: `10.1140/epjc/s10052-009-1143-7`. arXiv: `0907.0388 [hep-ex]`.

[20] C. Adolph et al. »Study of $\Sigma(1385)$ and $\Xi(1321)$ hyperon and antihyperon production in deep inelastic muon scattering«. In: *Eur. Phys. J. C* 73.10 (2013), p. 2581. DOI: `10.1140/epjc/s10052-013-2581-9`. arXiv: `1304.0952 [hep-ex]`.

[21] Boris Grube. »A Trigger Control System for COMPASS and A Measurement of the Transverse Polarization of Λ and Ξ Hyperons from Quasi-Real Photo-Production«. PhD thesis. TU München, 2006. URL: `https://wwwcompass.cern.ch/compass/publications/theses/2006_phd_grube.pdf`.

[22] J. Podolanski and R. Armenteros. »III. Analysis of V-events«. In: *The London, Edinburgh, and Dublin Philosophical Magazine and Journal of Science* 45.360 (1954), pp. 13–30. DOI: `10.1080/14786440108520416`. eprint: `https://doi.org/10.1080/14786440108520416`. URL: `https://doi.org/10.1080/14786440108520416`.

[23] Tobias Schlüter. »The $\pi^-\eta$ and $\pi^-\eta'$ Systems in Exclusive 190 GeV/c^2 π^-p Reactions at COMPASS (CERN)«. PhD thesis. LMU München, 2012. URL: `https://wwwcompass.cern.ch/compass/publications/theses/2012_phd_schlueter.pdf`.

[24] C. Adolph et al. »Odd and even partial waves of $\eta\pi^-$ and $\eta'\pi^-$ in $\pi^-p \to \eta^{(\prime)}\pi$ at 191 GeV/c«. In: *Physics Letters B* 740 (Jan. 2015), pp. 303–311. ISSN: 0370-2693. DOI: `10.1016/j.physletb.2014.11.058`. URL: `http://dx.doi.org/10.1016/j.physletb.2014.11.058`.